2009

VORTEX MODEL OF OPEN CHANNEL FLOWS WITH GRAVEL BEDS

Brian James Belcher
University of Kentucky, brian@beavercreekhydrology.com

ABSTRACT OF DISSERTATION

Brian James Belcher

The Graduate School
University of Kentucky
2009

VORTEX MODEL OF OPEN CHANNEL FLOWS WITH GRAVEL BEDS

ABSTRACT OF DISSERTATION

A dissertation submitted in partial fulfillment of the
requirements for the degree of Doctor of Philosophy in the
College of Engineering
at the University of Kentucky

By

Brian James Belcher

Lexington, Kentucky

Co-Directors: Dr. James Fox, Associate Professor of Civil Engineering and Dr. Scott Yost, Associate Professor of Civil Engineering

Lexington, Kentucky

2009

ABSTRACT OF DISSERTATION

VORTEX MODEL OF OPEN CHANNEL FLOWS WITH GRAVEL-BEDS

Turbulent structures are known to be important physical processes in gravel-bed rivers. A number of limitations exist that prohibit the advancement and prediction of turbulence structures for optimization of civil infrastructure, biological habitats and sediment transport in gravel-bed rivers. This includes measurement limitations that prohibit characterization of size and strength of turbulent structures in the riverine environment for different case studies as well as traditional numerical modeling limitations that prohibit modeling and prediction of turbulent structure for heterogeneous beds under high Reynolds number flows using the Navier-Stokes equations. While these limitations exist, researchers have developed various theories for the structure of turbulence in boundary layer flows including large eddies in gravel-bed rivers. While these theories have varied in details and applicable conditions, a common hypothesis has been a structural organization in the fluid which links eddies formed at the wall to coherent turbulent structures such as large eddies which may be observed vertically across the entire flow depth in an open channel. Recently physics has also seen the advancement of topological fluid mechanical ideas concerned with the study of vortex structures, braids, links and knots in velocity vector fields. In the present study the structural organization hypothesis is investigated with topological fluid mechanics and experimental results which are used to derive a vortex model for gravel-bed flows. Velocity field measurements in gravel-bed flow conditions in the laboratory were used to characterize temporal and spatial structures which may be attributed to vortex motions and reconnection phenomena. Turbulent velocity time series data were measured with ADV and decomposed using statistical decompositions to measure turbulent length scales. PIV was used to measure spatial velocity vector fields which were decomposed with filtering techniques for flow visualization. Under the specific conditions of a turbulent burst the fluid domain is organized as a braided flow of vortices connected by prime knot patterns of thin-cored flux tubes embedded on an abstract vortex surface itself having topology of a Klein bottle. This model explains observed streamline patterns in the vicinity of a strong turbulent burst in a gravel-bed river as a coherent structure in the turbulent velocity field.

KEY WORDS: Open channel flow, turbulence, gravel-bed rivers, coherent structures, velocity distributions

Author's Name: Brian J. Belcher
Publication Date: 1/12/2009

VORTEX MODEL OF OPEN CHANNEL FLOWS WITH GRAVEL-BEDS

By

Brian James Belcher

Dr. Scott A. Yost
Co-Director of Dissertation

Dr. James F. Fox
Co-Director of Dissertation

Dr. Kamyar C. Mahboub
Director of Graduate Studies

January 12, 2009
(Date)

RULES FOR THE USE OF DISSERTATIONS

Unpublished dissertations submitted for the Doctor's degree and deposited in the University of Kentucky Library are as a rule open for inspection, but are to be used only with due regard to the rights of the authors. Bibliographical references may be noted, but quotations or summaries of parts may be published only with the permission of the author, and with the usual scholarly acknowledgements.

Extensive copying or publication of the dissertation in whole or in part also requires the consent of the Dean of the Graduate School of the University of Kentucky.

A library that borrows this dissertation for use by its patrons is expected to secure the signature of each user.

Name Date

_____

_____

_____

_____

_____

_____

_____

_____

_____

DISSERTATION

Brian James Belcher

The Graduate School

University of Kentucky

2009

VORTEX MODEL OF OPEN CHANNEL FLOWS WITH GRAVEL BEDS

DISSERTATION

A dissertation submitted in partial fulfillment of the
requirements for the degree of Doctor of Philosophy in the
College of Engineering
at the University of Kentucky

By

Brian James Belcher

Lexington, Kentucky

Co-Directors: Dr. James Fox, Associate Professor of Civil Engineering and Dr. Scott Yost, Associate Professor of Civil Engineering

Lexington, Kentucky

2009

This dissertation is dedicated to Shelly.

ACKNOWLEDGEMENTS

The following dissertation, while an individual work, benefitted from the insights and directions of Jimmy Fox, who exemplifies the high quality scholarship to which I aspire. Jimmy provided timely and instructive comments and evaluation at every stage of the dissertation process. I wish to thank the entire Dissertation Committee: J. Fox, S. Yost, R. Warner, J. Phillips and O. Wendroth. Each individual provided insights that guided and challenged my thinking. I wish to thank J. Jacob for assistance with instrumentation.

In addition to the technical and instrumental assistance above, I received equally important assistance from family and friends. My wife Shelly provided on-going support and encouragement throughout the dissertation process. Without her this would not have been possible.

TABLE OF CONTENTS

LIST OF TABLES

LIST OF FIGURES

1. INTRODUCTION

1.1 Background

Gravel-bed rivers are important to the civil engineering research community for many reasons, including human demands for water supply, navigation, recreation, civil infrastructure and stream restoration. Gravel-bed rivers are systems which are typically characterized as having turbulent flows of particles which may consist of solids, liquids and gases. A photograph of a recent civil engineering project involving a gravel-bed river is shown in Figure 1, which shows a turbulent flow evident by the white-caps on the water surface, induced by a hydraulic grade control structure being placed in the flow to benefit fishery habitats in Clear Creek near Golden, Colorado. The boulder structure in the photograph is intended to alter the existing flow characteristics in such a way that the river is controlled to improve fish habitats. Unfortunately, these types of civil infrastructure applications have not been fully studied in terms of turbulence and sediment transportation dynamics.

Figure 1. Photograph of a stream restoration project under construction in Clear Creek, Golden, Colorado, showing an excavator placing boulders in a gravel-bed river to control fluid and sediment transport mechanics in order to promote stable fisheries and channel stability

Three-dimensional flow dynamics and hydraulic stability are not fully understood for gravel-bed rivers; however, fishermen have long known that trout can be found holding and feeding in areas of strong currents in highly turbulent conditions. This biological phenomenon may be observed in the Tennessee Aquarium, which has a large open channel flow over a gravel and cobble bed in which several species of trout can be observed holding and feeding, as shown in the photograph (Figure 2). One may ask how do hydraulic control structures like the one shown in Figure 1 alter the flow in a gravel-bed river in such a way that is beneficial to fish habitats? Or in general, how do civil engineering projects of any sort control the turbulent flow properties of a gravel-bed river in order to achieve some globally recognized notion of stability?

Before these questions can be answered, a need exists to define the notion of stability in terms of fundamental physical principles and conservation laws governing the turbulent flows that occur in rivers. In reference to the conservation laws of fluid dynamics, "this is a God given system, and we have to study it as it is" (Shnirelman 2001). This is no trivial task, as it requires us to reconcile a major problem presented by our lack of understanding of the natural behavior of the turbulent flow. The origin, fate and transport of turbulence and turbulent structures such as large eddies in gravel-bed rivers remains a problem unsolved. The latter is not only a difficult problem facing the civil engineering research community, it represents a missing piece in the puzzle that is recognized as the last unsolved problem in classical physics (Holmes *et al.* 1998).

Figure 2. Photograph of trout holding in a turbulent region at the TN aquarium in Chattanooga, photograph Copyright © Brian J. Belcher 2009

Figure 2 is an example of the complexity of fluid motions which are common in gravel-bed rivers which may contain diverse biological habitats. The small bright lines in the photograph are created as air bubbles illuminated by the ambient fluorescent lighting in the room trace a small bright pathline during the time elapse of the exposure. The trajectories of the individual bubbles do not all appear to be going in the same direction, indicating that the flow may be turbulent, and have fluid mass flux into and away from the region at the bed. The fluid region in the center of the photograph contains a swirling type of motion and may be a region of low pressure caused by a structure in the turbulent flow that some researchers term a large eddy. Presumably these types of turbulent structures are important components of fish habitats and all instream processes in gravel-bed rivers including the motions of air bubbles and other particles such as sediments suspended in the flow.

In this thesis the focus is on rivers with granular beds and use the term "gravel bed" interchangeably with "granular bed". The fluid systems shown in the photographs above are both considered gravel-bed systems. This broad category includes many natural rivers on Earth. Particles sampled from river beds are generally noncohesive sediments with a granular structure which have been deposited due to fluvial processes. The most important parameters characterizing individual particles in a granular bed are size and weight. Noncohesive sediments are typically sands and gravels which form a mixture of particles ranging in size from 62 microns to large boulders with dimensions of meters.

Herein the term "gravel-bed" shall be intended to include all sizes of granular particles. Particles smaller than 62 microns are generally clays and silts. Surface area is an important parameter characterizing individual particles in this size range which typically have cohesive properties. These smaller particles are easily lifted from the bed during flood events and because of their much smaller mass they take much more time to fall out of suspension and thus are often termed "wash load" in sediment transport literature because they represent the fraction of particle mass which appears to wash through the reach without directly influencing the channel boundary; whereas, the bedload and suspended load are the portion attributed to the sand (<2 mm) and gravel (>2 mm) sizes. When sand and gravel particle size fractions are in motion along a river bed then this suggests that the river boundary is undergoing a deformation process. Larger particles such as cobbles and boulders may also be included in the particle size distribution of a gravel-bed river and usually the term "gravel bed" implies any collection of noncohesive particles with measurable particle sizes having mean value larger than 2 mm and the beds with mean value in the range 62 microns to 2 mm are called sand beds. It is common to classify river boundaries by appropriate statistical measures of sampled grain particles, for example by measuring the sizes in a collection of stones sampled in the river bed. Rosgen (1994) has presented a classification system of natural rivers which includes classes based on ranges of particle sizes: silt/clay, sand, gravel, cobble, boulder and bedrock.

Gravel-bed rivers were considered under-researched and poorly understood as late as the 1980's (Klingeman 1998) and since then much focus has been on the problem of understanding and predicting sediment transport dynamics. The general research is now moving towards a better understanding of how motion of sediments relates to concepts of river stability in terms of deformation of the channel boundary. The sediment transport problem is difficult, not only because the number of particles which composes the channel boundary is very large, i.e., bed heterogeneity, but also due to our lack of understanding of the turbulent velocity fields around these particles and the distribution of fluid stresses that turbulence causes on the channel boundary. Currently there is no way to predict the behavior or form of large eddies or other turbulent structures in these environments or how these structures influence the deformation of the channel boundary, e.g. by influencing gravel and sand particle motions.

1.2. Hypothesis

A number of limitations prohibit the advancement and prediction of turbulence structures for optimization of civil infrastructure, biological habitat and sediment transport in gravel-bed rivers. This includes measurement limitations that prohibit characterization of size and strength of turbulent structures in the riverine environment for different case studies as well as traditional numerical modeling limitations that prohibit modeling and predicting of turbulent structure for heterogeneous beds under high Reynolds numbers via the governing Navier-Stokes equations. While measurement and modeling limitations exist, this has not stopped researchers from theorizing the structure of turbulence in boundary layer flows, including gravel-bed rivers. A conceptual understanding of turbulence has been presented by a number of scientists and engineers (Falco 1977; Yalin 1977; Imamoto and Ishigaki 1985; Kaftori *et al.* 1994; Adrian, Meinhart *et al.* 2000; Shvidchenko and Pender 2001). While these theories have varied in their details and proposed applicable conditions, a common driving theme has been the hypothesis that there exists structural organization of turbulence that links the generation/shedding

of vortices at the wall with coherent vortical structural phenomena observed vertically across the flow depth. Recent research in fluid mechanics has seen the advancement of topological fluid mechanics, which is concerned with the study of vortical coherent structures (Ricca 2001; Boyland *et al.* 2003). Topological fluid mechanics are based on the fundamental conservation laws and allow model derivation of the coherent vortical shapes in the flow and their connectivity, i.e., a vortex model, which can lead to better understanding of the origin, form, and function of turbulence. In the present study, topological fluid mechanics is used with experimental results to derive a vortex model for gravel-bed flows and central to this thesis is the hypothesis that structural organization of turbulence does exist in gravel-bed rivers.

1.3. Research Objectives and Goals

A goal of this thesis is to derive a fluid model for the gravel-bed flow based on the topology of observed coherent structures in turbulent velocity fields. Topology is a branch of mathematics which deals with properties of surfaces and is fundamental to physical laws, i.e. the fluid model, and is important to current research in turbulence, e.g. (Khan and Ahmed 2005). This goal is relevant to the modeling of turbulent processes in gravel-bed rivers. A model derived from topological considerations is necessary to consider fluid motions which may be natural and only depend on intrinsic properties of the fluid media, e.g. types or shapes of vortices, *and* other fluid motions such as local accelerations that may depend on the external boundary conditions such as roughness or thickness of the flow. Such a model contributes to science by advancing our understanding of the physical laws applied to river environments.

A need exists for new data collected in flows over a gravel bed in the laboratory to further test the hypothesis that turbulence is structurally organized by large eddies and large-scale coherent structures. The data is necessary to help bound a vortex model of turbulence structure based on topologic principles. This data is necessary to provide experimental observations of the types of vertical fluid motions captured by the structural model formulation. Thereafter scaling to measurable physical boundary conditions such as roughness heights and flow thicknesses for comparison with previous research should be enabled. While turbulence data has previously been collected for gravel-bed flow conditions, this data has traditionally focused on time-average measurements and structure of time-series. Both spatial and temporal data are required to be able to "see" the structure of vortices. A need exists to be able to characterize measurable physical scales of these vortices using a consistent and reliable technique and thus necessitates turbulent velocity field decomposition, or filtering technique, which enables mathematical computations consistent with the topology used to describe the structural model. In order to "see" turbulence structure a method must be used that can visualize eddies moving in vector fields, similar to the way a motion picture camera may be used to "see" the motion of a sports team executing a play during a game, and therefore be used as a flow visualization tool to watch the dynamic evolution of a vortex system which may move in space and time. Previous research has shown us that an excellent tool for flow visualization is a spatial and temporal velocimetry technique called PIV combined with a turbulence filtering method called the POD. These techniques return time-series measurements for computing statistics such as the time-average in order that the temporal aspects of the turbulent flows may be assessed, as well as for comparison with previous vortex models derived without the aid of PIV or the POD filtering technique.

While recent efforts have had success with these techniques including PIV/POD (Adrian, Christensen *et al.* 2000) they have yet to be used for flow involving gravel beds.

It is expected that a broader understanding of the structural organization of turbulence including a topologically derived vortex model for the gravel bed flows will be useful for a number of applications. Specifically, one needed application is a physically-based approach to collapse time-average velocity data in rivers, for example, to predict the shape of the mean streamwise velocity profile in a cross-section. The latter is a geometrical adaptation of the underlying topology of the fluid motions. The early assumption by Prandtl and other researchers in the late 1800's through early 1900's that turbulent structures on average increase in size when transported vertically away from the bed was pioneering and pivotal to the study of wall bounded turbulence theory (Tokaty 1971). This assumption led to the introduction of the idea that the eddy length scale, l, is proportional to the distance from the bed, y, as $l = \kappa y$, where κ is the von Karmon constant; and thereafter a physically-based logarithmic law was derived. However, since that time it has been found that the log law is really only physically valid for about 15% of the flow depth in open channel flows (Nezu and Nakagawa 1993). Even so, current research in gravel-bed rivers has tended to focus on two-dimensional boundary layer models and empirical modifications of the log law to fit the entire velocity profile in a river. It is hopeful that averaging of an appropriate vortex model would provide a more physically-based time-average model of what is actually the structure of turbulence in a gravel-bed river.

The first objective is to perform a comprehensive literature review of vortex structure and conceptual turbulence models for flows in rivers and related fluid systems such as boundary layers. A second objective is to collect new data in flows over a gravel bed and perform analysis to assess the hypothesis that turbulence has structural organization for the flow conditions and to work towards characterizing the turbulence structure for a gravel bed including assessment of vortical features and their connectivity. The literature review and new data and results will provide the foundation for the next primary objective, which is to formulate a new vortex model of turbulence in gravel-bed rivers. A desirable feature of this model is to have the same topology as the observed vortex interactions that exist in a river. Thereafter invariant properties of the flow which are related only to the topology of the vortex model may be used for describing physical events in rivers, including the relationship between large and small scale turbulent processes, the turbulent bursting phenomena and other observed fluid motions in rivers and laboratory experiments. The purpose of the model is to provide a mathematical background to test the hypothesis of structural organization of the turbulent flow. Thereafter, a vortex model of structural organization can be used to understand and predict the fluid forces that cause portions of the river boundary to move and result in sediment transport phenomena and larger scale cyclic phenomena such as secondary currents and river meanders. Ultimately uses of this model include a tool for understanding and predicting the distribution of velocity and turbulent fluid stresses for describing the fluid dynamical forces involved in future particle transport studies. Further, a model of the structure of turbulence presents a map of streamlines in an attracting region of a turbulent system and can be used in future modeling methods that focus on the dynamical system context (e.g., Holmes et al. 1998). A long term goal of applications of the vortex model is a physically-based collapse of time-average velocity data at equilibrium conditions in gravel-bed rivers.

In addition to the above specific objectives, the research presented in this thesis works towards overcoming a broad research need to understand the natural, or background, turbulence complexity in gravel-bed rivers, including the influence of spatio-temporal patterns in turbulent velocity measurements. The latter are known as turbulent coherent structures and are the mathematical version of the physical phenomena which produce large eddies in rivers. Coherent structures are recognizable patterns in the velocity field, such as streamlines or vortex lines, which have a certain amount of spatial and temporal coherence in a local region of the fluid flow. The coherence gives these structures prominence with respect to the strongly incoherent turbulent field surrounding them (Porporato and Ridolfi 2002) and therefore a flow with coherent structures will, perhaps, influence particle motions, both incipient motion and trajectories, differently than a flow without coherent structures or with structures of a different form. Turbulent coherent structures are known to be important flow phenomena that influence the transport rates of sediments, including in-stream organic particle mobility and gases, such as the oxygen and nutrient transfer between the bed and the water column (Hondzo 1998).

The overall goal of this dissertation is to further the knowledge of natural flow processes in gravel-bed rivers, thus working towards a solution to the problem of turbulence which makes fluid modeling and prediction of sediment transport difficult. The questions addressed in this dissertation relate to the concepts of time and space in a fluid domain and the size, shape, spatial frequency, temporal frequency and strength of coherent turbulent structures and how these structures relate to the average distribution of velocity and fluid stresses in a gravel-bed, open-channel flow. An additional goal is to further investigate the structure of turbulence in gravel-bed rivers at the scales that are important for sediment transport of sand and gravel particles which are also important for other in-stream processes such as biological and chemical reactions necessary for sustainable fisheries and other habitats.

1.4. Scales of Observation for this Thesis

Rivers are studied at a variety of different scales, depending on the important process being considered. Rivers are long bodies of flowing water, for example in Kentucky a river is generally defined as a perennial body of surface water which is at least 100-miles long as measured on a historical topographic map. Fluids studied at these scales are called geophysical flows as they involve motions related to the rotating frame of reference of planetary motion. A photograph of the Kentucky River near Lexington is shown in Figure 3. The map shows a typical scale important for flood-studies and other large-scale hydraulic phenomena, at the "river-reach" scale. Typical reach scales used in practice are multiples of the channel width or meander wavelength. The reach scale is important because it applies to any natural river. Own may trace the river shown in Figure 3 and then trace the map of either a much larger river or a much smaller stream (smaller in terms of average flow rate) and then if they are scaled to fit the same size paper and placed side by side it sometimes becomes impossible to identify which flow is smaller (Leopold *et al.* 1964). This unusual form of symmetry is a generic property of rivers that does not depend on scale and therefore geometry and thus may be considered an intrinsic property related to the fluid motions inside the river.

Turbulence and large eddies, however, are generally studied at much smaller scales than the reach scale, for example on the order of the flow depth or fraction of width. These later units are much smaller than the typical scales used in the study of bulk

transport processes in rivers and for general civil engineering studies such as floodplain mapping studies. A recent review of other important scales related to the study of rivers is provided in Schwartz and Herricks (2008). The most relevant and most studied scale in river engineering is termed therein a "*mesohabitat*" within the reach planform that has a distinctive morphology with terms such as "pool-riffle", "channel geomorphic unit" and "bar unit" used by geomorphologists which may include a variety of areas or patterns of areas termed by fishery biologists as "backwaters", "pools", "riffles", "glides", "runs", "chutes", "rapids", "cascades", and "falls". Hydraulic metrics are important parameterizations of these physical habitats, e.g. turbulence intensity. Current research is leading towards classification of mesohabitats using the hydraulic parameterizations with the intent to evaluate the usefulness of mesohabitat units in terms of ecological information that can be used to constrain river restoration design objective functions (Schwartz and Herricks 2008).

Figure 3. Satellite view of the Kentucky River south of the University of Kentucky showing meandering characteristics which may be observed in smaller streams and other fluids

New experimental data is presented herein intended to focus on what may be termed a "riffle" scale in the context of river studies (Henderson 1966). Consider a typical longitudinal profile of a gravel-bed river that is naturally formed without local influences of externally imposed hydraulic controls such as dams or constrictions, as sketched in Figure 4.

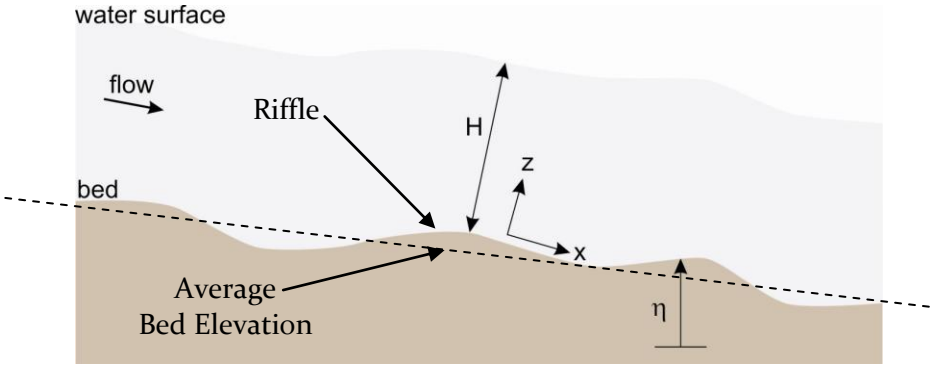

Figure 4. Definition sketch of typical gravel-bed river domain

Here a boundary layer coordinate system is often used where the direction x represents the streamwise flow direction and is parallel to the boundary and z is the direction normal to the boundary. The instantaneous flow depth H is measured at some x-coordinate along the z-axis. Riffles, as defined herein, occur in the locations denoted by local peaks in the longitudinal profile of a pool-riffle system. For example, if one were to draw a best-fit line through evenly spaced coordinates along the surface of the bed taken at intervals of say one meter in a large gravel-bed river, (dashed line in Figure 4) riffles are herein considered areas of the bed that plot above this line and pools are the areas that plot below this line. The riffles are of primary importance to civil engineering applications because they represent areas of minimal depth and therefore are likely locations for transportation crossings and other civil infrastructure. At the lowest flows the water surface may be nearly flat in the pools and very steep in the riffles; however, at the highest flows the slope of the water surface tends to match the slope of a line connecting the tops of the riffles. For this reason it is the riffle that is used to measure hydraulic properties that are critical to the general characterization of the flow through a river reach, for example flow gauging stations established by velocity measurements and stage-discharge correlations used by the USGS are applicable in riffles. In addition, stream inventories by the USFWS and stream classification systems used by the USEPA depend on the hydraulic parameters specific to the riffles.

2. REVIEW OF TURBULENCE AND TURBULENT STRUCTURES

This section focuses on the specific objective of a comprehensive literature review of turbulence structural models used in open-channel and related flows in order to describe physical events such as eddies that occur in dissipative systems. A viscous fluid system is a dissipative system because vorticity and momentum diffuse into the flow. Dissipative dynamical systems, i.e. the three-dimensional Navier-Stokes equations, are characterized by the existence of attractors which are structures in the phase space toward which neighboring trajectories approach as time goes to infinity. Attractors include fixed points and closed curves. A fixed point implies a stable steady flow solution whereas a closed curve implies a stable oscillation in the phase space. A well-known lower-dimensional attractor is the Lorentz, or butterfly attractor, which was also discovered by examining fluid flows, although highly simplified. These are the most generic coherent structures, or largest-scale "eddies", that exist within the fluid domain.

The word "eddy" herein is taken to be synonymous with "coherent structure" with respect to the literature in turbulence research and generally means some sort of coherent vortex motion when referring to fluid systems (Kline *et al.* 1967; Imamoto and Ishigaki 1985; Robinson 1991; Clifford 1993; Smith 1996; Dargahi 1997; Tamburrino and Gulliver 1999; Shvidchenko and Pender 2001; Roy *et al.* 2004). Eddies are coherent structures which tend to gradually grow and evolve and then die out with complex dynamics. Large eddies and thus coherent structures have been referred to with descriptors like "skeleton', 'backbone', 'DNA', etc. because most of the turbulence production, dissipation and transport near the wall are associated with them (Porporato and Ridolfi 2002).

2.1. Structural Model of Eddies in Rivers

The existence of eddies as coherent structures in rivers has long been known. A general model of the origin, fate and form of largest eddies in rivers was suggested in (Yalin 1977) and sketched here in Figure 5.

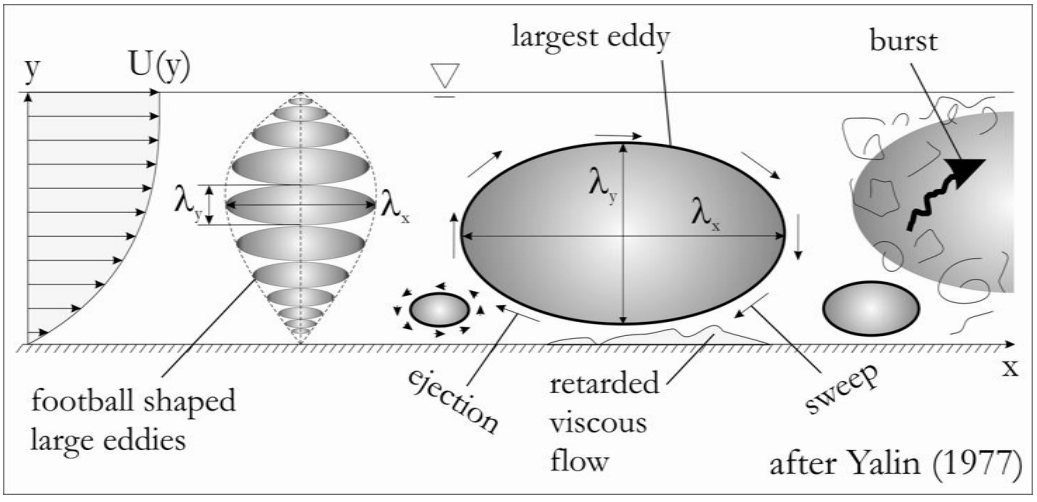

Figure 5. Conceptual model of large eddies in rivers, after Yalin (1977)

Yalin (1977), based on previous collections of observations of large eddies in rivers, proposed a model of "football shaped" large eddies that exist in a parallel shear flow, as

indicated by the shape of the velocity distribution on the left side of the figure. The spatial dimensions of these football shaped eddies, which could occur at any depth, were thought to vary as a function of the flow depth; however, the largest eddies were thought to continue to grow until occupying the entire flow depth. Yalin hypothesized that sweeping fluid motions caused by the largest eddies induced an area of retarded viscous flow at the wall which becomes unstable and is coupled with ejection motions induced by a smaller, more intense football-shaped eddy with opposite sense of rotation. Yalin nicknamed this smaller eddy the "eraser" and hypothesized that as kinetic energy was fed into this eddy from the largest eddy it would grow and consume the area of retarded viscous flow, thus 'erasing' it. Eventually the eraser eddy was thought to cause the largest eddy to become unstable and cause it to burst into a collection of random vortex filaments, or smaller eddies. Presumably the eraser eddy then grows to about the size of the flow depth and initiates the reverse process, describing a cycle of large eddies. The physical mechanism by which these football shaped eddies, or semi-spherical coherent structures, are formed is not understood. It is still unclear if football-shaped eddies exist in typical gravel-bed rivers or what may have caused them to form if they do exist.

2.2. Structural Models of Turbulent Boundary Layers

In boundary layer research the classical models for large eddies is qualitatively similar to that proposed by Yalin. Much of the literature on turbulence and coherent structures in boundary layers results from experimental studies using flow visualization techniques and time-series analysis of fluid velocities, e.g. (Hommema and Adrian 2002). Studies over the past half-century have investigated spatial and temporal characteristics of coherent structures by means of advanced flow visualization techniques and numerical simulations (Hoyt and Sellin 2001). First, observations of coherent spatial and temporal patterns in time-series measurements resulted in the identification of named patterns such as low-speed streaks which occur near smooth walls (Kline *et al.* 1967), and various types of eddies, including streamwise- and quasi-streamwise vortices, horseshoe vortices, u-loop vortices and ring vortices (Makita and Sassa 1993; Smith 1996; Dargahi 1997).

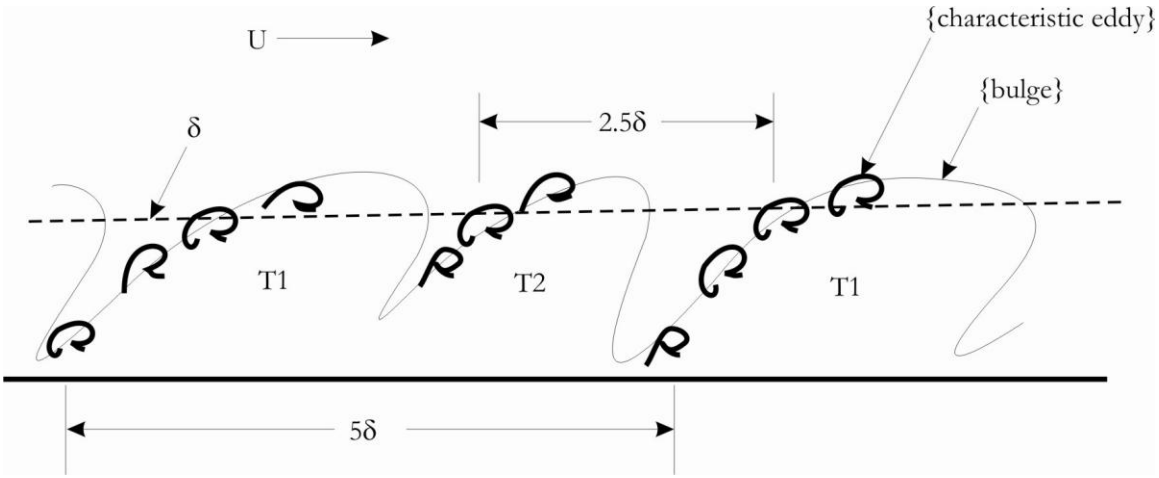

Figure 6. Large Scale coherent structures in smooth boundary layer after Falco (1977)

Later, some similar coherent structures were observed near roughened walls, such as low-speed streaks (Grass *et al.* 1991; Defina 1996), and long, slender structures oriented along the streamwise axis and lifting from the wall (Stoesser *et al.* 2005).

An early sketch of the shapes of experimentally observed eddies in boundary layers is shown in Figure 6, which is a sketch of large bulges (T1-T2-shapes) in a turbulent boundary layer containing "characteristic" eddies (mushroom-shapes) discovered by (Falco 1977). What are termed large football-shaped eddies in Yalin's model are analogous to what are termed large-spanwise, elliptical, inclined turbulent vortices or bulges in boundary layer research which is based on flow visualization methods, e.g. Falco (1997) and Robinson (1991).

Large internal fluid stresses have been associated with passing coherent structures in smooth turbulent boundary layers. Figure 6 is a structural model of large scale motions and "characteristic" or "typical eddies" observed in the outer layer (Falco 1977) in which the experimenter visualized turbulence in air at moderate Reynolds number flows over a fixed wall. Those experiments were conducted in a wind tunnel illuminated by laser light and seeded with an oil-fog originating in the boundary layer. Moving cameras were used to follow typical characteristic motions of passing "bulges" that contained "characteristic eddies" advecting along their surfaces. These bulges have alternate speeds and sense of twisting motions and were typically paired or coupled, i.e. the bulges labeled T1 and T2 in Figure 6, over a streamwise distance of 5δ where δ is the local boundary layer thickness. Individual bulges were typically spaced $5\delta/2$. The tops of the bulges extended above the boundary layer thickness and the characteristic eddies moved along bulge surfaces at higher velocities in the outer layer and were slower near the bed, often becoming amalgamated into the upstream bulge. Falco concluded that a passing characteristic eddy caused a strong, intermittent burst of Reynolds stresses in the outer layer. The bulges and characteristic eddies were further used to develop a conceptual model for parallel lamination of plane beds (Allen 1984), who assumed a spatial array of eddies in the classical Kelvin's cat's eye pattern (Thomas and Bull 1983) that produces quasi-periodicity in the instantaneous bed shear stress due to compression of the velocity isovels and hence alternating deposition and erosion patterns. The dimensions of these turbulent bulges are consistent with the dimensions of large eddies in rivers suggested by Figure 5; however, the relationship between these smooth boundary layer-type vortices and vortices that may occur in gravel-bed rivers is unknown.

Falco's experimental studies of large scale organization in the outer layer suggest that a vortex bursting process associated with the passing of large coherent structures strongly influences the internal fluid stresses and energy dissipation throughout the boundary layer. Bursting had previously been studied in terms of small vortex motions observed at very low Reynolds numbers, i.e. gentler flows, in the region very close to the wall, most notably in the experiments of (Kline *et al.* 1967). Many types of vortices were observed to form at the wall and their interactions were associated with the term "burst", as fluid near the wall tends to roll up and then eject outwards during the passing of a coherent vortex structure, causing strong instantaneous changes to the fluid stresses. Falco's observed mushroom-shaped characteristic eddies were different than the typical "hairpin" or "horseshoe" shaped vortices observed in (Kline *et al.* 1967) in that the mushroom-shaped eddies are larger, possibly linked vortices.

A model for the formation of the larger vortex motions in the outer layer of smooth turbulent flows was further developed by (Robinson 1991), as sketched in Figure 7, which indicates that the presence of multiple horseshoe or hairpin type vortices aligned with the streamwise axis produces vortex stretching and twisting of the legs of a downstream

hairpin, causing them to "bridge" and then the head portion entrains the pinched-off portions of the legs. The eddy becomes transformed into a spanwise spheroid that moves into the outer layer. These processes describe vortex reconnection events and streamwise velocity discontinuities at the wall. It is unclear if the mushroom-shaped characteristic eddies observed by Falco (1997) are the same as the ring vortex or large-scale spanwise vortex described in Figure 7, also it is unclear if the largest vortex then somehow grows into a sustainable turbulent bulge.

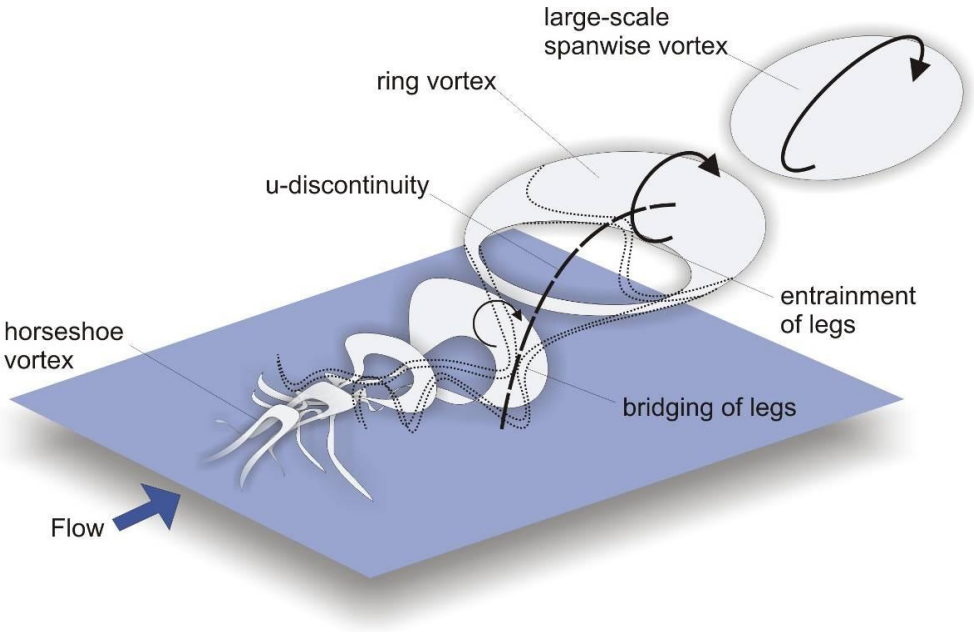

Figure 7. possible mechanism for creation of large eddies vortex further from the wall in boundary layers - after Robinson (1991).

The most intense Reynolds stress producing events in turbulent boundary layers are attributed to the presence of hairpin vortices (Panton 1996). A recent model of the structural organization of hairpin vortices in smooth turbulent boundary layer flows is that of (Adrian, Meinhart *et al.* 2000) shown in Figure 8. This model shows a vortex organization of hairpin vortices into packets of varying ages, speeds and sizes. The packets have a common feature which is the angle of inclination, γ, connecting the heads of the vortices within a given packet. The packet of hairpins is thought to induce a low-speed fluid region that loses strength with distance from the wall.

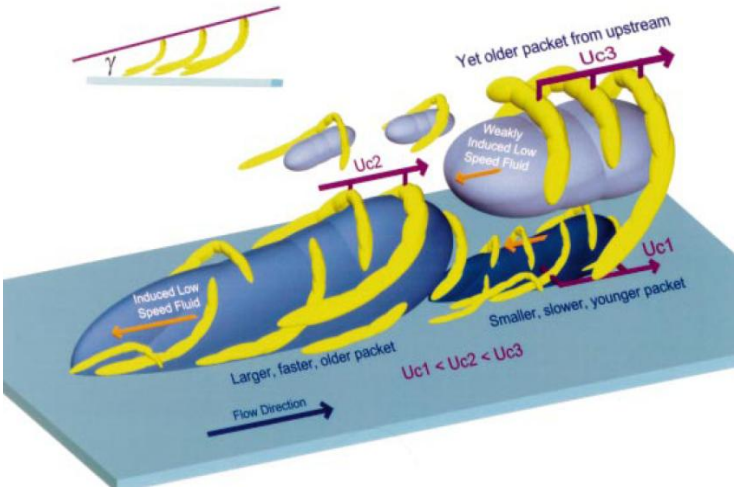

Figure 8. Outer layer vortex packet model in boundary layers - reprinted from Adrian et al. (2000)

The main findings of (Adrian, Meinhart *et al.* 2000) include that (1) eddies propagate together with packet convection speeds; (2) the inclination angle of the eddies in the packets is small close to the wall and increases towards the head of the largest hairpin head in the packet, ranging from 45-90°; however, the average angle of packet inclination was 12°, which is similar to other recent findings of inclination angles of wedge-like flows ; (3) packets have approximately linear growth angles that are smaller than the angle of the inclined hairpin heads within the packet; (4) newly formed packets are small and convect more slowly than older, faster packets; (5) small packets exist within larger packets and may be overtaken by larger packets; (6) backflow zones near the wall in packets, or regions of uniform negative streamwise turbulent momentum, have much larger spatial extents in the streamwise direction than individual eddies due to a 'solenoidal' effect of coherence between hairpins in a packet; (7) the number of hairpins in a packet increases with Reynolds number up to observed groupings of ten hairpins; (8) the spatial organization of nested packets explains the uniform zones of high-momentum and low-momentum fluid often observed in turbulent wall-bounded flows; and (9) packets may form nesting arrangements that extend many boundary layer thicknesses in the streamwise direction. Evidence that suggests that the hairpin vortex packet is the fundamental structure in wall-bounded flows, including most boundary layers, channel flows, pipe flows and the atmospheric boundary layer (Hommema and Adrian 2002).

2.3. Structural Models of Vortex Structures in Laboratory Channels

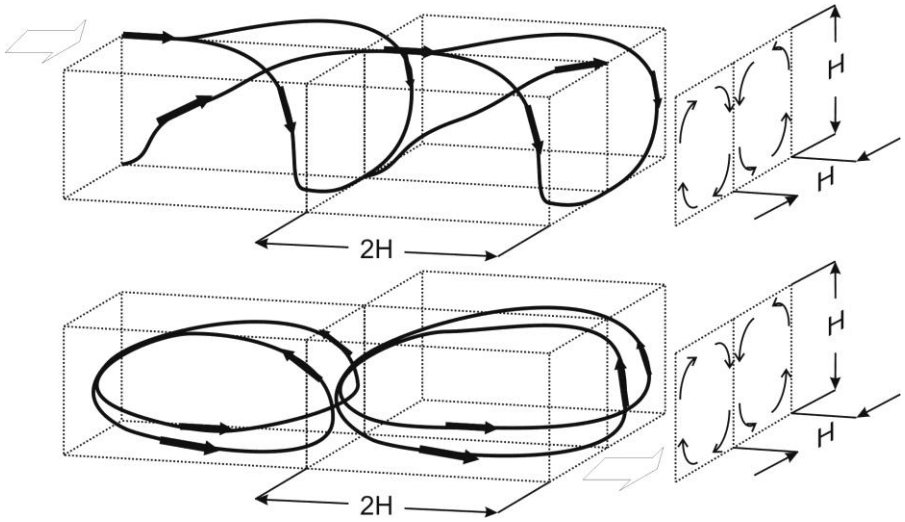

Figure 9. Sketches of large secondary current patterns observed in smooth open channel flows (Imamoto and Ishigaki 1985) (Top) and (Tamburrino and Gulliver 1999) (Bottom)

Large-scale coherent structures specific to smooth open channel flows of water have also been the subject of laboratory research. Based on laser-doppler measurements in an open channel flume (Imamoto and Ishigaki 1985) proposed a model of the turbulent structure in the outer region of an open channel flow that suggests a helicoidal braid of vortices is responsible for the secondary circulation patterns known as Prandtl's second kind (Prandlt's first kind are the large secondary motions known to occur in river bends (Kundu and Cohen 2004)). These findings are supported by the experimental results of Tamburrino and Gulliver (1999) in which a similar type of outer-region behavior was observed in an open channel flow driven by the motion of a smooth belt at the wall. Figure 9 includes two sketches of the outer region of the flow in straight, smooth open channels characterized by a flow depth H. Tamburrino and Gulliver (1999) concluded that these two patterns in Figure 9 are the same coherent structure viewed in different frames of reference, and that secondary currents were observed to occur in both cases due to this structural arrangement of large vortices, as shown projected onto the end planes. In both cases the streamwise length of the instantaneous structure is shown to be about 2H where H is the flow depth, resulting in secondary circulation cells that measure H x H in cross section. The dimensions and streamwise pairing of these structures are consistent with the model of turbulent bulge structures (Falco 1977); however, the smaller, mushroom-shaped vortices are not apparent.

Funnel-shaped coherent turbulent structures have been observed in smooth, horizontal open channels by means of laser Doppler anemometry and flow visualization techniques (Kaftori *et al.* 1994). Therein the experiments indicated the turbulence was dominated in the wall region by a structure containing large scale streamwise vortices with origin at the wall and expansion into the outer layer. The topology of the structure

was described as a collection of vortices spiraling around a funnel laid sideways with its open end in the direction of flow. The authors concluded that this funnel-shaped vortex topology describes most observations of wall turbulence phenomena made previously, such as streamwise vortices, ejections and sweeps, as illustrated in Figure 10.

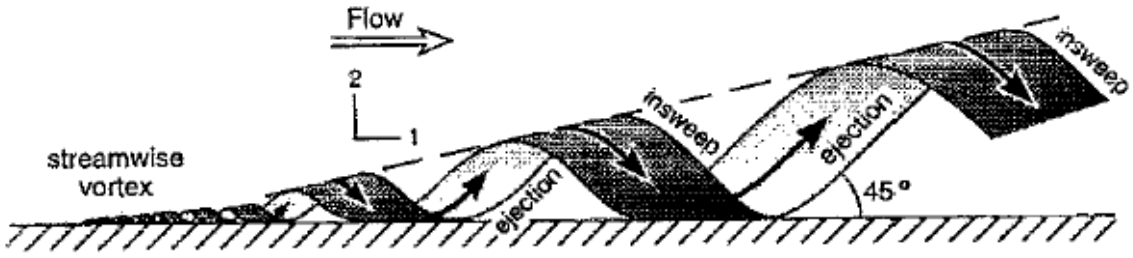

Figure 10. Funnel-shaped vortex structure observed in boundary layer - reprinted from Kaftori et al. (1994).

For a set of controlled experiments, the general form of large coherent structures in an open channel with a gravel bed has been visualized (Shvidchenko and Pender 2001). The structures were observed to move slowly in the direction of the mean flow, which is to the left of the page, in a three-dimensional rolling motion. These large structures had dimensions that scale with a multiple of the flow depth and have an asymmetric form with high forward speed that is a form of downwelling or sweep-like motion on the downstream side, and ejection-like or upwelling on the upstream side (Shvidchenko and Pender 2001). These structures were somewhat periodic and were observed to have streamwise lengths ranging from 1.4*H* to over 7*H* with average lengths about 4*H* (Shvidchenko and Pender 2001).

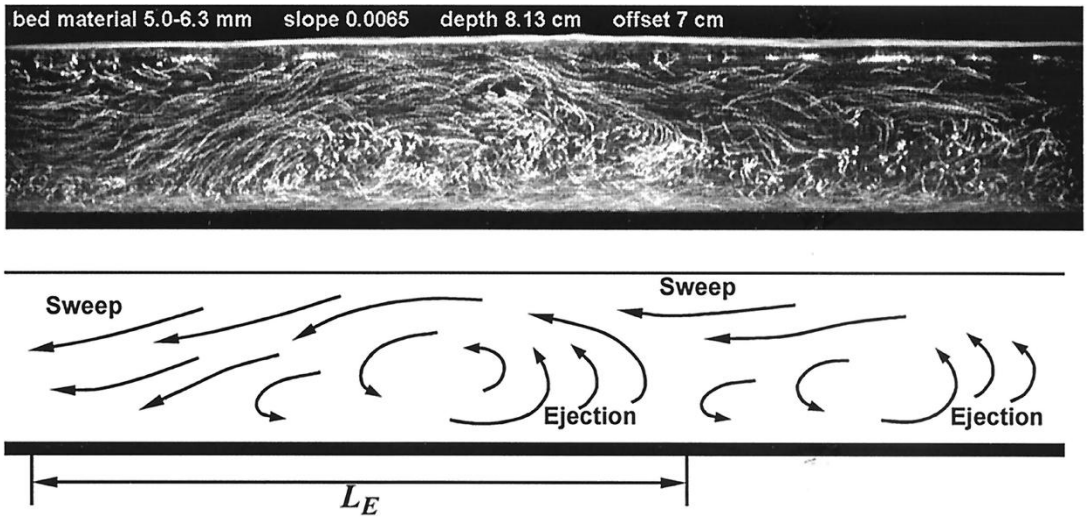

Figure 11. Very large eddy in a gravel-bed flume reprinted from (Shvidchenko and Pender 2001), flow is right to left

Research measurements conducted in the field are less conclusive than laboratory measurements; however, a study of a gravel-bed river in Canada indicates that large-scale,

wedge-like turbulent structures are common and that some similarities exist with outer-layer structures observed in smooth boundary layers and the coherent structure shown in Figure 11 (Roy *et al.* 2004). The structures observed in rivers are slender and scale with dimensions approximately H, $H/2$ to H, and $3H$ to $5H$ in the vertical, horizontal and streamwise directions where H is the flow depth (Roy *et al.* 2004). The streamwise length scales of these structures are in the range of other large eddies observed in rivers at flood stage and the model of (Yalin 1992).

Simultaneous velocity and pressure measurements in recent laboratory experiments using gravel-bed flows have identified structures with the same characteristics as the large wedge-like structures observed in rivers (Detert *et al.* 2007). The latter experiments had an aspect ratio $B/H = 4$, where B is the channel width. This low aspect ratio value is much smaller than what occurs in many natural gravel-bed rivers, for example rivers shown in photographs used by engineers to estimate roughness values for flow models (Hicks and Mason 1998), and the influence of strong secondary currents due to corner vortices is unclear.

Based on the literature, coherent turbulent structures play a dominant role in the turbulent processes; however, additional large scale fluid motions may coexist with these coherent structures, such as what have long been termed secondary currents, which are known to form in both laminar and turbulent flows.

2.4. Secondary Circulation

It is known that the point of maximum velocity in a river is often located below the free-surface and this phenomenon is thought to be due to the action of secondary currents which are described as circulations of flow lines in the plane of the channel cross-section (Henderson 1966). Laminar secondary currents describe mean circulatory motions such as the flow through a meander bend in a river or closed duct flow with sharp corners, and are thought to be caused by curvature of the channel boundary (Kundu and Cohen 2004). These types of fluid motions have been termed Secondary Currents of Prandtl's First Kind, or simply corner-flows, and are denoted by the arrows pointing along the span-wise direction of a cross-sectional boundary (Figure 12).

In Figure 12, cross-sections 1 and 5 are riffles, which tend to occur at the cross-over between river meanders; whereas, pools tend to occur in the bends, i.e. cross-section 3. Cross section 2 is termed a run and cross section 4 a glide. These types of secondary currents have been used to describe the shape of river bends and the velocity distribution in river meanders; however, researchers still have relatively poor understanding of the form of the secondary currents for variable conditions; moreover, the causes for rivers to develop meanders are unknown and it is a difficult task to predict their form and function.

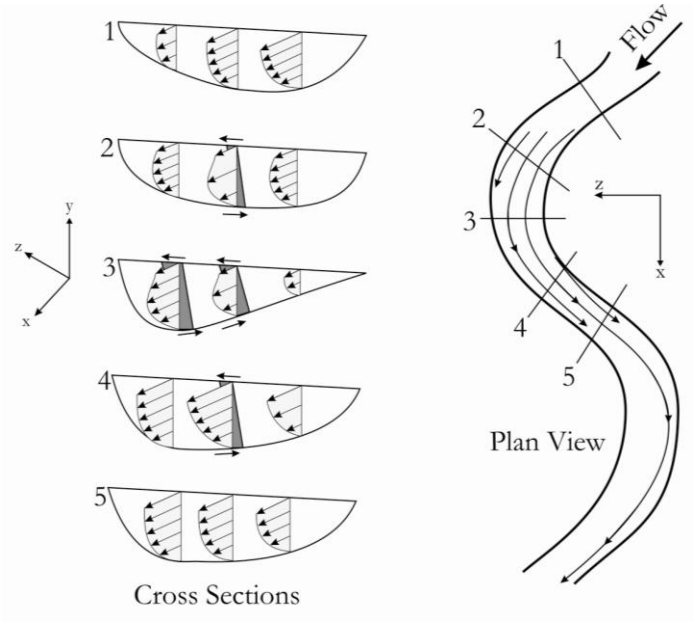

Figure 12. Secondary currents of prandtl's first kind in a river meander after Leopold et al. (1964)

These large-scale secondary currents are thought to be due to the inviscid streamlines on the channel boundary, which is curved and has singularities at the corners where the walls intersect the channel bed. In a river it is often not clear where the channel walls intersect the bed, e.g. Cross Section 3 in Figure 12. Secondary currents in river meanders have long been known (Leopold *et al.* 1964) however their origin is unknown. Although secondary flows in curved rivers and laboratory channels have been observed and well documented there is currently no theory that explains why these secondary currents develop or why river meanders themselves develop, often with the same pattern that occurs in a different river which may be much larger or smaller (Leopold *et al.* 1964). For the same reasons researchers are unable to understand or predict why a river may exist in a stable form, i.e. long geologic time periods with regular change in form of the channel cross section and planform geometry, as a straight, meandering or braided channel. Based on laboratory experiments and observations of natural rivers on Earth there appear to be more than one stable form for gravel bed rivers; for example braided or meandering. In the case that the river planform is nearly straight with respect to the gradient of the valley the channel thalweg is sinuous, which has been observed in laboratory experiments and in the field (Leopold *et al.* 1964). It is well known that channels formed in non-cohesive sediments in a straight laboratory flume become sinuous and braided in some cases.

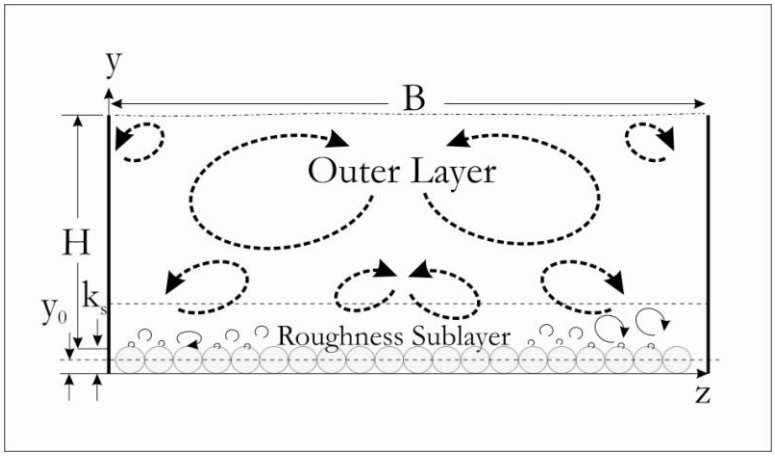

Figure 13. Secondary currents of prandtl's second kind in a rectangular test channel after Nezu (2005)

Another type of secondary current is thought to be generated primarily by Reynolds stresses generated due to turbulence anisotropy in straight open channels (Muller 1982; Nezu 2005). Turbulence anisotropy is known to be heavily influenced by the roughness geometry and the channel aspect ratio. Secondary currents of this type have been termed Prandtl's Second Kind and are shown in Figure 13. These circulation patterns are known to change form in a straight channel at some critical value of the channel aspect ratio. For smooth open channel flow experiments $(B/H)_{cr} \approx 5$ (Nezu 2005). It is unclear how secondary currents of the second kind interact with the first kind in rivers because they have different origins. Clearly the second kind must be intimately related to the dynamics of the turbulent coherent structures near the bed; however, it is unknown if these are the same eddies in Yalin's model.

No complete explanation has been found for the occurrence of these circulations in straight channels and why they change form at a critical value of the aspect ratio. It has long been known that secondary currents frequently occur as two cells in narrow channels and with many more than two cells that have alternate sense of rotations for the case of very wide rivers; however, in channel bends there is usually only one large cell of secondary circulation and possibly a few smaller cells. Rosgen (1994) found that a stream classification system could be developed for natural gravel-bed rivers with aspect ratio as one of the delimiting criteria and in that system a value of 12 divides narrow streams from wider streams. Very wide channels have aspect ratios > 40 and tend to become braided (Rosgen 1994).

2.5. Vortex Shedding from 3-Dimensional Particles

In addition to the discussion of large-scale turbulent field structure, a review of some important research on bluff-body shedding and production of turbulent wakes behind three-dimensional objects immersed in a fluid flow is provided below. These types of fluid motions are known to be the dominant kinetic energy production and dissipation processes very close to the surface of a gravel-bed river.

Much work has been done in order to quantify the flow processes around single and primarily spherical particles and from these results it is known that the flow contains vorticity and the streamlines are complicated due to the shedding of vortices from the solid surfaces of the particle. Experimental and computational results show that a bluff

body immersed in a flow may cause vortices to form on the surface of the body and these vortices then tend to grow to a downstream length of about twice the particle diameter (Manhart 1998) prior to shedding into the turbulent wake, which is presumably filled with other such vortices.

It has been suggested that three-dimensional vortex surfaces in an ideal flow follow a shedding process that is a continuous, self-similar shedding of a portion of the circulation from one vortex ring to the next; whereas, two-dimensional vortex sheets, (e.g., vortex pairs shed from planar bodies like bridge piers) roll-up into vortices that do not shed their circulation (Nitsche 2001). Ideal three-dimensional vortex surfaces roll-up into a series of vortex rings; each vortex leaves a tail that eventually rolls up into another vortex with a new tail and the time interval between formation and shedding is proportional to the inverse of the circulation. This mathematical treatment of Nitsche (2001) revealed that the shedding process of a three-dimensional body may be viewed as a mechanism by which the vortex reconnections approach a steady state.

Strong streamwise vortex braids are sometimes attached to a bluff body that is shedding vorticity (Poncet *et al.* 2006). The braids interact with the larger vortices shed in the wake of the body through patterns in the fluid streamlines with topological properties of knotted or linked vortex tubes.

Flow close to a gravel-bed includes these mechanisms and is impacted by a distribution of particles on the bed; however, the turbulent dynamics are controlled by the largest particles on the bed (Manhart 1998).

The above review highlights some limitations in the existing research concerning turbulence structure as applied to gravel-bed rivers. There is of yet no turbulence model that describes how "eddies" in rivers (Roy *et al.* 2004), relate to vortex packets observed in boundary layers (Adrian, Meinhart *et al.* 2000; Hommema and Adrian 2002), or to the large coherent structures observed in smooth-bed open-channel experiments (Tamburrino and Gulliver 1999), and finally to secondary currents which may be turbulent or laminar (Nezu 2005). It is unclear why the large eddies occur in rivers, i.e. how they were initially formed or how far away they came from. Yet many individual models which show coherent structures and turbulence organization have been conceived for boundary layers, though very few have been for rough bed situations. The most important structural models applicable to gravel-bed rivers include the large secondary current and vortex patterns observed in open channels (Imamoto and Ishigaki 1985), the conceptual model of large eddies in rivers (Yalin 1977, 1992), and the recent boundary layer organization model of vortex packets (Adrian, Meinhart *et al.* 2000).

3. EXPERIMENTS

Next a description is provided of the experiments conducted for the purposes of testing the hypothesis that the structural organization of turbulence in gravel bed flows and also specifically for visualizing the turbulence and coherent structures which may exist for a set of controlled laboratory conditions. It is expected that reach-scale secondary currents such as those shown in Figure 13 may exist under these test conditions, which were performed in straight flumes; however, the presence or absence of smaller or larger-scale structures which may be responsible for secondary currents setup by the corner-flows or the roughness elements is not inferred prior to flow visualization. At first a somewhat intuitive or arbitrary approach is taken, as is often the case with experimentalism, and then models are developed which rely on the data to make inferences about larger scale events.

A suite of flow visualization experiments representative of gravel-bed river flows at bankfull depth under hydraulically rough, fully turbulent conditions were designed for this research. These experiments relate to the objective of developing a model to describe observable fluid motions due to turbulent coherent structures evolving in space and time in an open channel with a gravel bed. The experiments are used to investigate the hypothesis of turbulence structural organization by measuring instantaneous fluid particle displacements, velocities and accelerations in a controlled environment in order to conclude whether or not vertical velocity fluctuations exist and in what form they occur, i.e. if any structure is observable in otherwise randomly fluctuating velocity vector field or time-series plots. Statistics were computed from the experimental data that allow comparison of these new results to the previous research in turbulent boundary layers and to assess how sampling methods, including temporal and spatial sampling frequency, impact mathematical structures such as mean and variance. The latter is important in order to determine to what extent our observations may be considered different than truly random observations of point velocities in gravel-bed rivers.

The experimental data were collected in laboratory channels having fully turbulent flows as later verified from the measured velocity data. The channel conditions, including fluid parameters such as density, temperature, flow rate, roughness elements and operating methods were fixed during each experiment and then the velocity data were measured for an arbitrary, but long enough time to assess temporal statistics. A single flow-visualization test lasted about four seconds. Longer duration measurements were acquired with an independent velocity vector measurement probe as will be described below. This allowed the turbulent flow to develop for a very long time relative to the time scales of the anticipated fine structure of the turbulent velocity field in the boundary layer. To obtain the steady or quasi-steady turbulent flow conditions for each test, typically the bulk flow rate, Q, was adjusted between tests to achieve target mean depths, H, in the range of 2-9 cm. This allowed flows which have aspect ratios defined by the dimensionless quantity $B^* = B / H$ to be in the range of gravel-bed rivers observed in nature, e.g. the experimental aspect ratios include values in the range from low to moderate with respect to gravel-bed rivers at bankfull flow or statistical equivalence, in single-thread rivers classified as the B, C and E streamtypes (Rosgen 1994).

Channel slopes S were in the range 0.001 to 0.02, which is consistent with slopes of mild to steep rivers in nature where gravel-bed conditions would be expected. Smaller particles would be more easily mobilized in these flows than in much lower gradient

flows. For each test hydraulically rough conditions were established by forcing the flow to have a dimensionless relative smoothness parameter $R^* = H / D_{84}$, which describes the physical roughness heights of the particles on the bed, to be in the range which is representative of rivers with coarse beds composed of gravels, cobbles or boulders. For example, a gravel-bed river having a mean flow that is one meter deep would be expected to have relative smoothness determined by the range of particle sizes greater than about 4 mm, or R^*= 500. The same flow over a coarser bed, e.g. describable by the upper end of the gravel fraction of 64 mm, would have $R^* = 15.6$. The flow visualization tests were fixed in smoothness values less than about 12.

In open channels gravity waves are sometimes the most important physical processes and these experimental conditions are meant to be dynamically similar to rivers that are mildly sloping with respect to the water surface. These flows are typical of rivers which have mean velocities characterized by a dimensionless speed, or Froude number $F = V / (gH)^{1/2}$, which expresses the speed, V, relative to the speed of a normal deep-water gravity wave. The Froude number for all experiments was in the subcritical range < 1 which is representative of nearly all flood flows in gravel-bed rivers. Flows in the supercritical range F > 1 are called shooting flows and typically are very erosive and tend to scour river channels into bedrock or to highly resistive soils.

Another important dynamic similarity variable used in fluid experimentation is made between the characteristic velocity length scale and the viscous dissipation time scale. The latter is called a Reynolds number and there are a great many different Reynolds numbers that can be determined for any given flow and usually they are all related. In the case of most laboratory-scale experiments it is not possible to achieve scaling based on viscous properties of the fluid as expressed in dimensionless numbers such as a Reynolds numbers simultaneously with the Froude number. It is customary to use a Reynolds number based on the thickness of the boundary layer or flow depth in the form $Re_H = VH / \nu$ (Rodriguez and Garcia 2008). The depth Reynolds numbers computed from the measured velocity data in these experiments compare well with previous laboratory experiments of velocity distributions and secondary currents in open channels, e.g. Muller (1982); Nezu and Rodi (1985); Tamburrino and Gulliver (1999); Shvidchenko and Pender (2001); Rodriguez and Garcia (2008). Depth Reynolds numbers in field conditions are often considerably higher, for example the study of Roy *et al.* (2004) $Re_H \sim 200{,}000$.

A particle Reynolds number can also be defined as $Re_P = VD_{84} / \nu$ based on the bulk velocity, mean depth and representative roughness element size, respectively. In these tests this particle Reynolds number was fixed in ranges representative of natural rivers based on the comparison with the relative smoothness parameter. The particle Reynolds numbers are sufficiently high for all experiments such that in reference to a boundary layer having spherical roughness height represented by the D_{84} particle size, all tests represent conditions where a so-called "laminar" flow would separate over the surface of the particle, possibly resulting in an attached toroidal vortex fluid surface that periodically breaks off in the form of distorted vortex loops eventually resulting in a turbulent wake (Kundu and Cohen 2004) lacking a regular vortex street or dominant periodicity, but perhaps having noticeable spirals (Panton 1996).

Two different laboratory facilities were used for the experiments, each having a open channel laboratory flume. These flumes were modified to have experimental parameters in the ranges of values representative of natural rivers to compare the general results of

the flow visualization tests with velocity measurements. Flow visualization tests were used to provide most of the experimental data and to develop the turbulence model in one laboratory setup. Unfortunately, flow visualization tests were not conclusive in the wider of the two experimental channels, primarily due to uncontrolled fluid conditions including chemical pollutants, primarily detergents, which interfered with the laser light used in the PIV measurement technique. However, time-series velocity data were obtainable with the ADV device in both channels. This allows useful comparison of the structural model developed herein with the turbulent time-series for two independent channel conditions, representing different gravel-bed rivers and providing a larger range of channel aspect ratios and particle Reynolds numbers from which to derive comparisons with previous research and field measurements.

The experiments were conducted in flumes at two separate facilities at the University of Kentucky, the Hydraulics Research Laboratory of the Civil Engineering Department (Figure 14) and the Hydrology and Hydraulics Laboratory of the Biosystems and Agricultural Engineering Department (Figure 15), referred to herein as the CE Flume and the BAE Flume, respectively. Information is sought on the origin of large eddies and secondary motions and therefore straight experimental channels were used in order to eliminate motions of Prandtl's first kind as much as possible. It is known that straight channels carved into alluvium tend to develop meanders by an erosion and deposition process; therefore, it is natural to research the origins of coherent structures and secondary currents of Prandtl's second kind in a straight channel before attempting to expand a theory that may also include Prandtl's first kind.

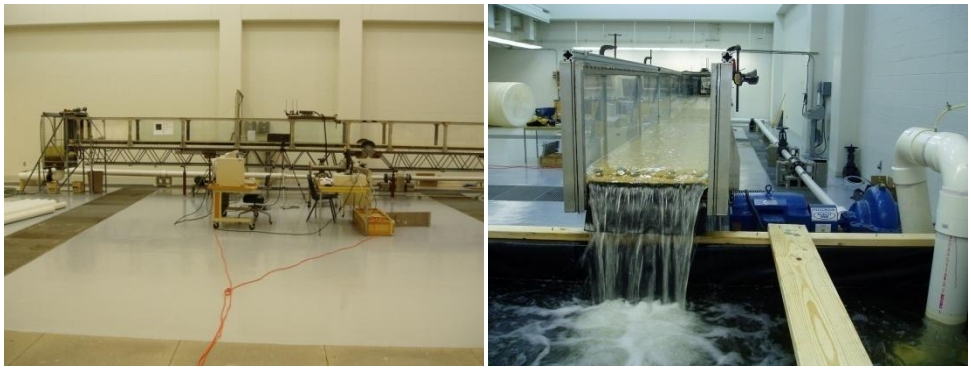

Figure 14. Photographs of CE Flume Copyright © Brian J. Belcher 2009

Figure 15. Photographs of BAE Flume Copyright © Brian J. Belcher 2009

Existing flumes were restored and modified for purposes of these experiments and structurally altered to enable flow visualization and advanced velocimetry instrumentation platforms. Both flumes are 12 m long and rectangular in cross-section. The CE Flume is 0.61-m wide and the BAE flume is twice as wide (1.22-m). A sketch of the common mechanical features is provided in Figure 16.

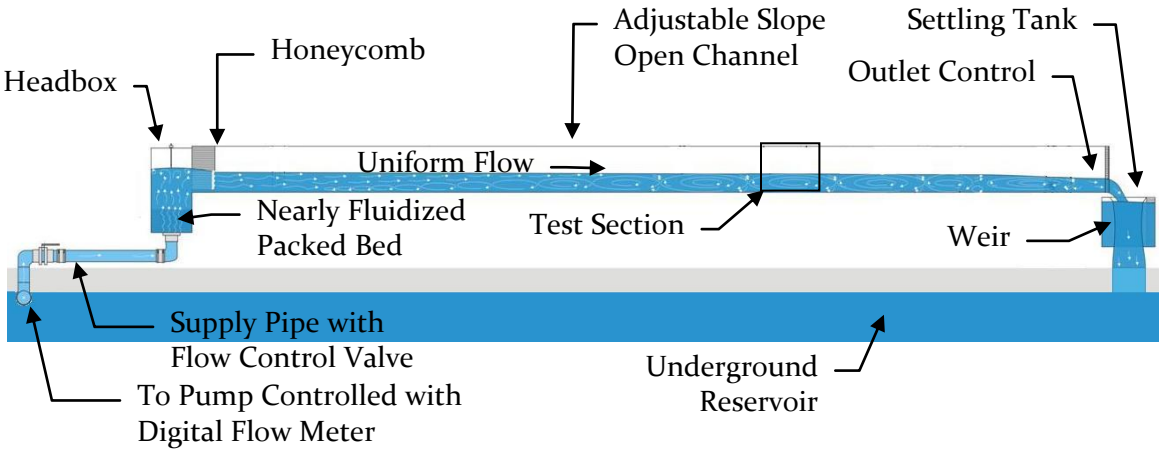

Figure 16. General diagram of experimental channels

For both flumes the flow was extracted from an underground storage reservoir with an electronically controlled sump pump with 6-inch-diameter supply pipe fitted with flow control valves. The flow was forced upwards through a packed bed of rounded river gravels at the point of fluidization. A fluidized or nearly fluidized bed conditions was established in the flume headbox to dampen any large scale fluctuations that might be attributed to the flow recycling mechanics and to produce a well-mixed volume of fluid for dispersing seed particles, which are powders of fine suspended sediments used as fluid motion tracers. In both flumes the flow was straightened horizontally with respect to the bed at the channel inlet with a 127-mm long honeycomb of 6.4-mm-dia. plastic tubes. Steady flows were established in the test sections approximately 6-m or further downstream of the channel inlet.

These flumes are equipped with hydraulic jacks that allow variable channel slopes. The outlet conditions were controlled to produce minimal drawdawn and stable upstream conditions. Downstream control could be established with stones glued to the bed near the free overfall to establish a control section. Random patterns of stones were used with gaps measuring about half the particle diameter, itself on the order of the flow depth, and also sometimes specific patterns of stones were arranged according to the geometry of the observed coherent structures; either method of arranging the downstream control stones worked well for these test conditions. Bed and water surface heights were measured with a point gage mounted on an instrumentation panel suspended above the flow (Figure 15). The instrumentation panel was constructed as a sliding platform having a firmly mounted digital camera for imaging the bed materials, an acoustic Doppler velocimeter, high-powered laser and an array of lenses and prisms used for particle image velocimetry.

Prior to testing in each flume, the bulk flow rate was calibrated with a Venturi meter and Doppler flow meter in the supply pipe, and a settling tank at the discharge end of the channel having a 45° weir for an outlet. The bulk flow rate calibrated with these devices is measured with an error of less than 2%.

The experiments were run with fixed granular beds. The channel beds were surfaced with angular aggregates embedded on thin, fiberglass-resin panels. Gravel-sized roughness elements were installed in the CE Flume and coarse sand-sized elements in the BAE flume. Particle size distributions of the gravel-sized materials were measured using a photogrammetric microscopy technique. A high-resolution digital camera was mounted on the instrumentation sled with its axis normal to the bed and an ensemble of photographs was acquired on a grid of non-overlapping rectangles measuring approximately 20 cm x 26 cm. The image size was selected so that intersecting the photograph with a rectangular coordinate system intersects about 100 stones, on average, as shown in Figure 17, a representative sample of the test section of the CE Flume.

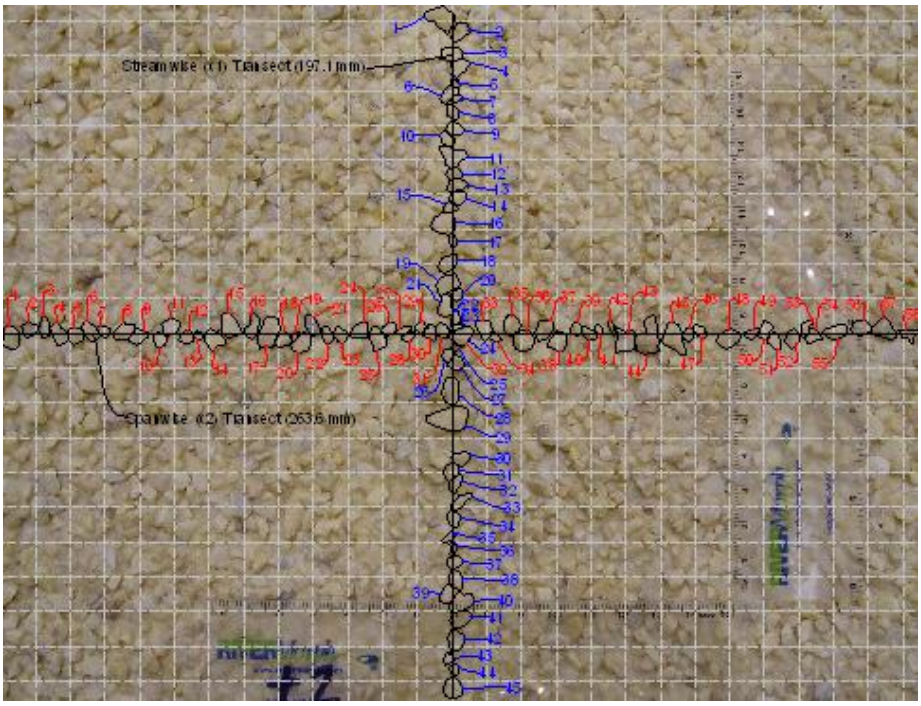

Figure 17. Particle size distribution measurement (CE Flume)

In Figure 17 the particles intersecting the streamwise flow axis (vertical line) and the spanwise flow axis (horizontal line) have been identified by digitizing their projected boundaries with a vector drawing software. The 1 cm x 1 cm grid superimposed on the image (gray dashed lines) indicates the relative sizes of the individual particles. For each particle identified in the photograph, the area of the enclosed boundary was measured as the equivalent area of the enclosed polygonal digitization in the imaging plane. Spline curves were used to digitize the particles and to measure the projected particle areas and then characterized each particle in terms of a single dimension using an equivalent circle diameter (Rhodes 1998) of the area in the imaging plane as described by the diagram in Figure 18.

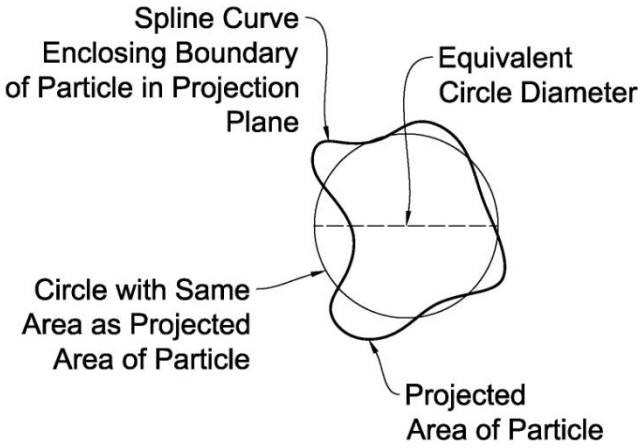

Figure 18. Definition sketch of equivalent circle diameter used to describe bed roughness elements in the CE Flume

A total of 300 particles were measured by adding transects from two additional photographs (not shown). A statistical analysis of the equivalent circle diameters was performed using standard methods (Nielsen and Wendroth 2003). Standard statistics assuming random samples, including the first four moments of the size distribution, are tabulated below in Table 1, where the D84 is the size for which 84-percent of the sizes are smaller. The D84 is an arbitrary representative value that is typically used to describe a collection of particles in a gravel-bed river. If the particles are normally distributed the D84 corresponds to the mean plus two standard deviations of variance. Here, however, the distributions have a slight kurtosis, thus are not normally distributed and the median value of 4.4 mm is perhaps best to describe the distribution of particles. The maximum particle size is twice the median value for the sampled population.

Table 1. Results of a statistical analysis of 300 equivalent circle diameters on the bed of the CE Flume

Minimum (mm)	2.0
Maximum (mm)	8.8
Median (mm)	4.4
Mode (mm)	2.8
Arithmetic mean (mm)	4.48
Population Variance (mm^2)	1.89
Coefficient of Skewness (mm^3)	0.58
Coefficient of Kurtosis (mm^4)	3.50
Coefficient of Excess (mm^4)	0.50
Standard Deviation (mm)	1.38
D84 (mm)	5.70

For the BAE flume a coarse sand was used and an alternate particle size distribution method was needed due to the problems of higher resolution photography needed to measure smaller particles and the higher number of photographs and particle digitization required; however, the surface was carefully swept after installation of the panels and

particle size distribution parameters were estimated as D_{50} = 1 mm and D_{84} = 1.5 mm using a pebble count procedure on the remaining fixed grains.

3.1 Velocimetry

The objectives of this thesis deal with formulating a turbulence model to describe observable events which are measureable fluctuations in the velocity fields. The fluid velocity fields allowing to evolve steadily under these test conditions were sampled with two types of instrumentation used to obtain instantaneous values of fluid velocity measurements: acoustic Doppler velocimetry (ADV) and particle image velocimetry (PIV). The ADV is a device that measures the three components of the velocity vector at a point in space by using the Doppler effect of high-frequency sound waves emitted from a probe and refracted by the seed particles in the flow. The ADV is used to detect patterns in time-series of fluctuations in the velocity field at a point in space. The PIV is a photogrammetric device which collects data useful to describe the spatial variations in turbulent phenomena and is used for visualizing coherent structures as observable patterns in space, i.e. multiple points simultaneously, and in time-series. These devices utilize the most modern methods for measuring turbulent velocity fields in the laboratory.

3.1.1. ADV

The ADV was used to collect velocity data at higher temporal resolution than allowed by the present PIV setup. This allows a comparison of trends that may be apparent in the time-series data to trends that may be observed in the spatial fields measured with PIV. A turbulent coherent structure would by definition be measureable in either case.

The ADV probe was mounted on a measurement carriage and suspended it side-looking into a very small region near the upstream boundary of the PIV field of view as shown in Figure 19. For each experiment using this measurement device the probe was positioned at the mid-depth of a quasi-steady flow and used to measure the three-dimensional velocity components u, v and w (streamwise, vertical and spanwise) which are the three orthogonal components of the average velocity of a small volume recorded at a sampling frequency of 50 Hz. The instrument has a sampling volume of 9×10^{-8} m^3 with a resolution of 1×10^{-4} m s^{-1} and accuracy of 1% of measured velocity. The ADV probe was oriented side-looking due to the shallow flow conditions. Errors that may produce erroneous values are caused by (1) turbulence or eddies created by the presence of the instrument in the flow, (2) other sources of acoustical waves such as noises which accompany particle collisions and reflections from walls, and (3) misalignment of the probe with the local coordinate system; all of which were carefully considered and minimized as much as possible during the experiments. Data collected with the ADV was processed with a computer software WinADV32 which was used to rotate the data into the local coordinate system to account for the effect of using a side-looking probe and also to remove outlying data points as suggested by the probe manufacturer using the software's phase-space threshold outlier removal method, which removed less than 3% of data points. This method is further described in the WinADV32 technical manual. The output from WinADV32 was used as the basis for time-series analysis using computer algorithms written in the MATLAB software.

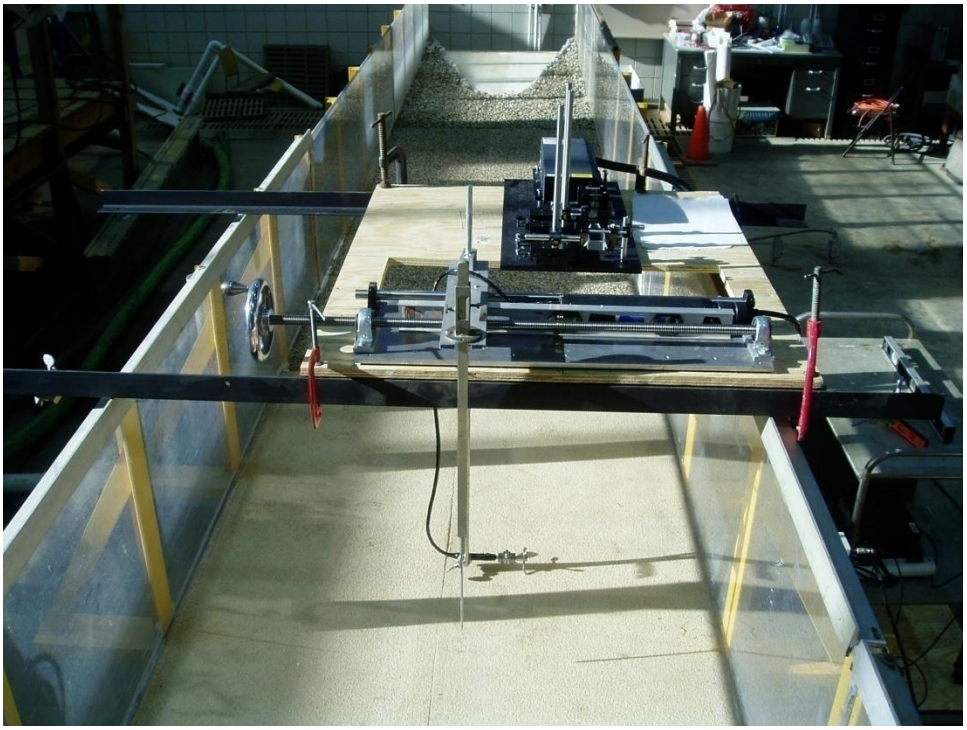

Figure 19. Photograph of the measurement carriage showing side-looking ADV probe head Copyright © Brian J. Belcher 2009

3.1.2. PIV

The PIV system was also used to measure a space-time-series of the velocity data. This method includes a much larger sampling volume than the ADV and is also useful for flow visualization following accepted methods used in past turbulence research (Adrian, Christensen *et al.* 2000). Unfortunately, a gain in spatial resolution results in a loss of temporal resolution due to the limitations of computer hardware and software processing of high-resolution photographs required for PIV analysis. In general, the PIV technique is based on the process of tracking fluid elements by identifying the light scattered by seed particles in photographs separated by small time intervals. The seed particles are illuminated by a pulsed laser light source in the form of a thin, vertical sheet and displacements and deformations in the sheet are recorded with a high-resolution camera. Thereafter, velocity, vorticity and Reynolds stresses are calculated from the displacements and deformations measured from the digital photos using a digital PIV algorithm. The Wall Adaptive Lagrangian Parcel Tracking (WaLPT) digital PIV algorithm was used for processing the images. A detailed description of the algorithm and its formulation and additional uses in fluid mechanical systems can be found elsewhere (Sholl and Savas 1997; Santhanakrishnan and Jacob 2007). The output from WaLPT was located at nodal points of a square grid measuring 82 nodes in the streamwise direction. WaLPT output was further analyzed using custom MATLAB codes.

The PIV laser sheet was projected in the streamwise-vertical plane with a 50 mJ double-pulsed, Nd: YAG laser with pulse separations fixed at 132 μs. A 10-bit Kodak Megaplus CCD camera with a 1008 x 1018 pixel array was used for capturing images of the flow field illuminated by the laser. The sampling rate of the PIV system was 15 Hz. The camera was positioned approximately 0.5 m away from the light sheet and its optical field

of view was focused on the light sheet through the channel's clear sidewall using a 75-mm zoom lens. Uniform seeding was accomplished using the same fine sediments which were used during the ADV measurements. The seed particles are assumed to be neutrally buoyant and therefore are very close to the actual fluid motions in the test channels. Later this assumption was tested by performing additional tests in the same flumes using filtered water mixed with neutrally buoyant, silver-coated, hollow, glass spheres as seed particles. The results of the mean velocity and visualization tests were the same for the two types of seed particles. For each test, 122 digital photographs were recorded for processing which resulted in 61 vector fields covering the entire flow depth for approximately 2.5 times the flow depth in the streamwise direction.

3.2 Individual Test Descriptions

Velocimetry measurements were acquired at steady or quasi-steady flows having the fixed experimental parameters identified in Table 2, where the fluid density, dynamic viscosity and kinematic viscosity were estimated based on tabulated values of water and are known to vary with temperature (Kundu and Cohen 2004).

Table 2. Fixed experimental conditions

Parameter	Symbol	Value	Units	Tolerance	Estimated Error
Width (CE, BAE)	B	0.61, 1.22	m	0.002	0.16 %
Fluid Temperature	T	19.8	°C	1	5.05 %
Fluid Density	ρ	997.06	kg/m^3	0.52	0.05 %
Dynamic Viscosity	μ	1.01E-03	Pa s	5.32E-05	5.27 %
Kinematic Viscosity	ν	1.01219E-06	m^2/s	5.22E-08	5.16 %
Gravitational Constant	g	9.8100	m/s^2	0.0500	0.51 %
Roughness Size (BAE)	D_{84}	0.0015	m	0.00005	3.33 %
Roughness Size (CE)	D_{84}	0.0057	m	0.0005	8.70 %

Independent experiments were performed in these flumes for various combinations of flow parameters described in Table 3. The flow in each test has a cross-sectional area A = BH and hydraulic radius R = A / (B + 2H), where the quantity B + 2H is the length of the wetted perimeter made with the channel depth H and width B. As mentioned previously Channel slopes S were in the range of 0.001 to 0.02 and were held the constant during each test. The bulk velocity is defined V = Q / A and the shear velocity $V^* = (gHS)^{1/2}$.

Table 3. Independent test conditions

Test	Flume ID	Method	Bulk Flow Rate (liter/s)	Mean Depth (cm)	Flow Area (cm^2)	Hydraulic Radius (cm)	Bed Slope (cm/cm)	Bulk Velocity (cm/s)	Shear Velocity (cm/s)	Aspect Ratio	Relative Smoothness	Froude Number	Depth Reynolds Number	Particle Reynolds Number
1	CE	PIV	24.8	7.0	426.7	5.7	0.0063	58.1	6.6	8.7	10.0	0.70	40,157	3,270
2	CE	PIV	31.5	7.6	463.3	6.1	0.0063	68.0	6.9	8.0	10.7	0.79	51,091	3,832
3	CE	PIV	9.5	3.9	237.7	3.5	0.0063	39.8	4.9	15.6	6.1	0.64	15,327	2,240
4	CE	PIV	18.9	5.8	353.6	4.9	0.0063	53.5	6.0	10.5	8.5	0.71	30,654	3,013
5	CE	ADV	25.2	7.0	426.7	5.7	0.0063	59.1	6.6	8.7	10.0	0.71	40,873	3,328
6	BAE	ADV	19.1	6.9	814.9	6.2	0.0011	23.4	2.7	17.1	41.2	0.28	15,978	347
7	BAE	ADV	16.2	6.0	708.6	5.4	0.0011	22.9	2.5	19.7	36.3	0.30	13,552	339
8	BAE	ADV	24.5	8.0	944.8	7.0	0.0011	25.9	2.9	14.8	47.0	0.29	20,495	384
9	BAE	ADV	35.0	9.0	1062.9	7.8	0.0011	32.9	3.1	13.1	52.1	0.35	29,279	488
10	BAE	ADV	35.0	6.0	708.6	5.4	0.0050	49.4	5.4	19.7	36.3	0.64	29,279	732

4. TURBULENCE DECOMPOSITION METHODS AND RESULTS

A decomposition method is the application of a mathematical filtering technique which allows for the visualization of structures in temporal or spatial data. A need exists for a decomposition method contribution because the velocity fields measured under these test conditions have high turbulence intensity and therefore may have "background noise" which may be considered due to random fluctuations. Also, the Reynolds numbers in these rough-turbulent flows are very much higher than in flow visualizations of smooth turbulent boundary layers which initially led to the development of vortex models. Because of the high Reynolds number there are many more sizes of eddies present in the flow as compared to a more gentle, nearly laminar flow. The intent of any turbulence decomposition is to separate the random fluctuations from the more coherent, though possibly very less noticeable, large-scale or slower fluctuations in a set of measured vector data. Thereafter the decomposed turbulent vector fields can be used to better test the hypothesis of structural organization in the gravel bed flows and may be visualized, examined for patterns, and the scales of various eddies or other patterns may be determined from the resulting plots.

4.1 Time-Series Decomposition Methods and Results

The ADV instrument may be run for a very long time compared to the current PIV setup and at higher temporal frequency of data acquisition. Although the focus of the experiments is flow visualization it best to begin by describing the methods used for time-series decomposition because they rely heavily on classical statistics and have been used extensively in previous research on turbulence structures. The spatial decomposition methods are extended from the time-series methods and will be described in detail later. Example ADV results are provided below in

Figure 20 for illustrating the time-series methods, where the data have been truncated to fit in a time window of about 120 s. The length of the time window may be combined with the statistical mean of the data within the window to define a bulk transport length scale, for example if the mean streamwise velocity is determined to be 50 cm/s then a streamwise length scale in the 120 s time window is 6,000 cm, which is much larger than length of the experimental channel and the flow depth for all tests. Of course, a bulk transport length scale as defined above is only possible if the expected value of the ensemble is equivalent to the expected value within an arbitrarily chosen interval of time. This is possible if the data are stationary with respect to time and the streamwise direction, a typical assumption in equilibrium flows such as boundary layers. The ADV time-series data are shown in

Figure 20 where the experimental conditions for each plot are identified by the test number identified below each time axis. The first plot shown in

Figure 20 contains data from Test 5 taken under similar conditions in the CE Flume as the PIV experiments. Test 6 and the remaining tests (BAE Flume) are generally in order of increasing flow strength and are for much smoother bed surface conditions than Test 5. Each plot shown below has three series representing the three orthogonal components of the velocity vector $u_i(t) = \vec{u}(t) = [u, v, w]$ for the i=1, 2 and 3 components in the streamwise, wall-normal and spanwise directions, respectively.

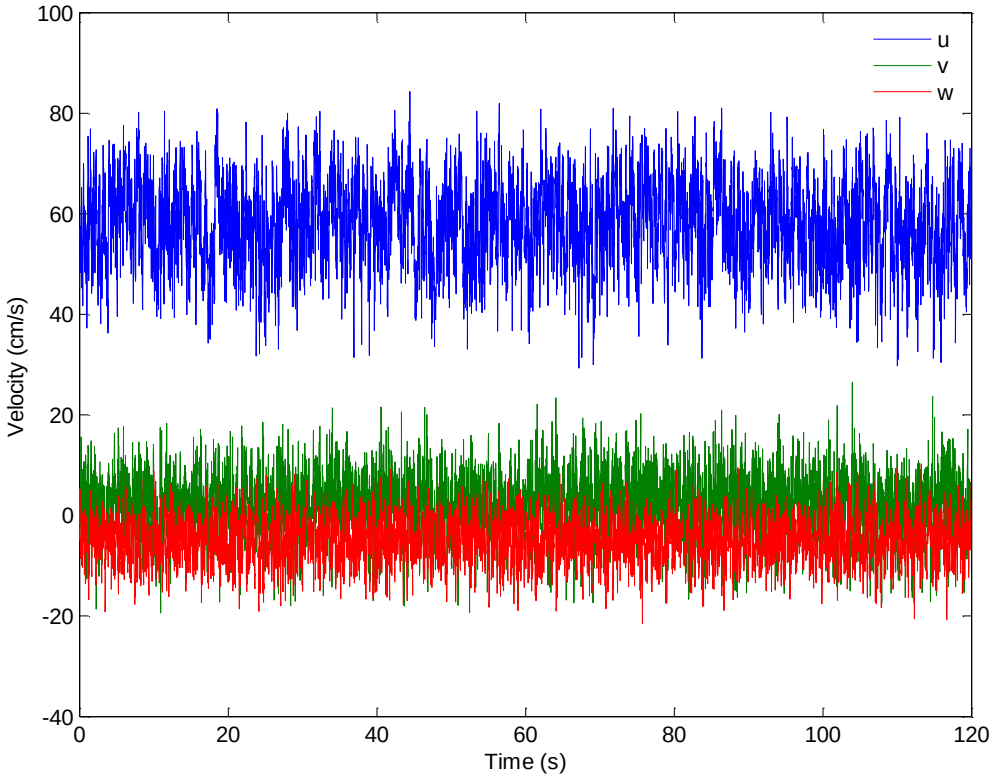

Test 5

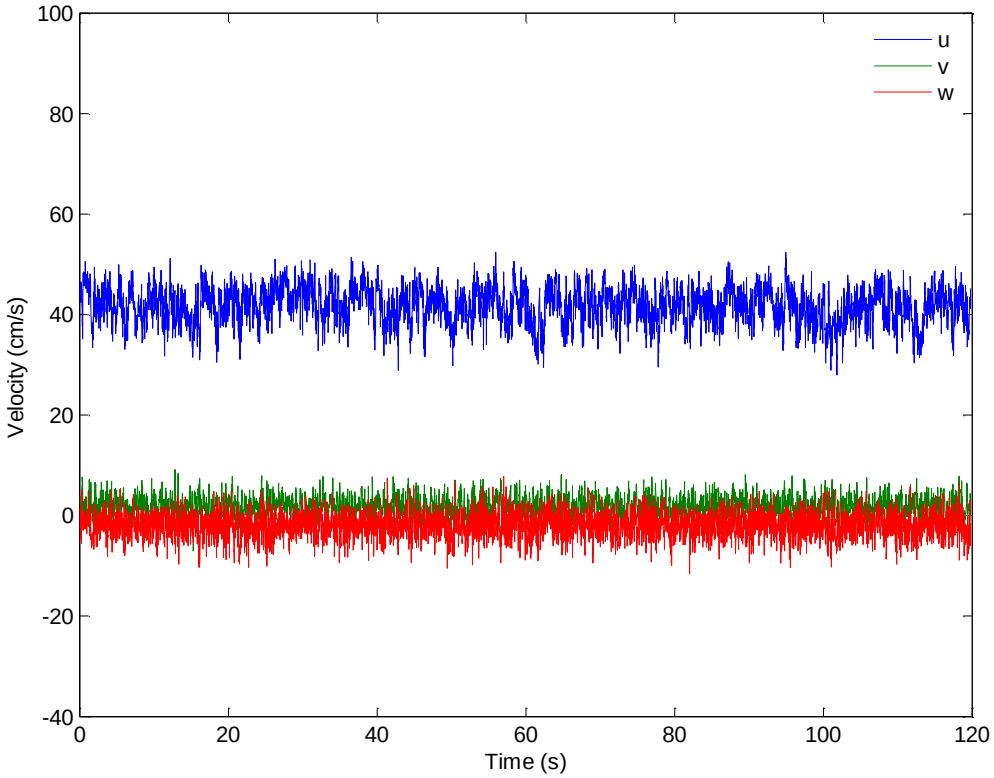

Test 6

Figure 20. ADV time-series data

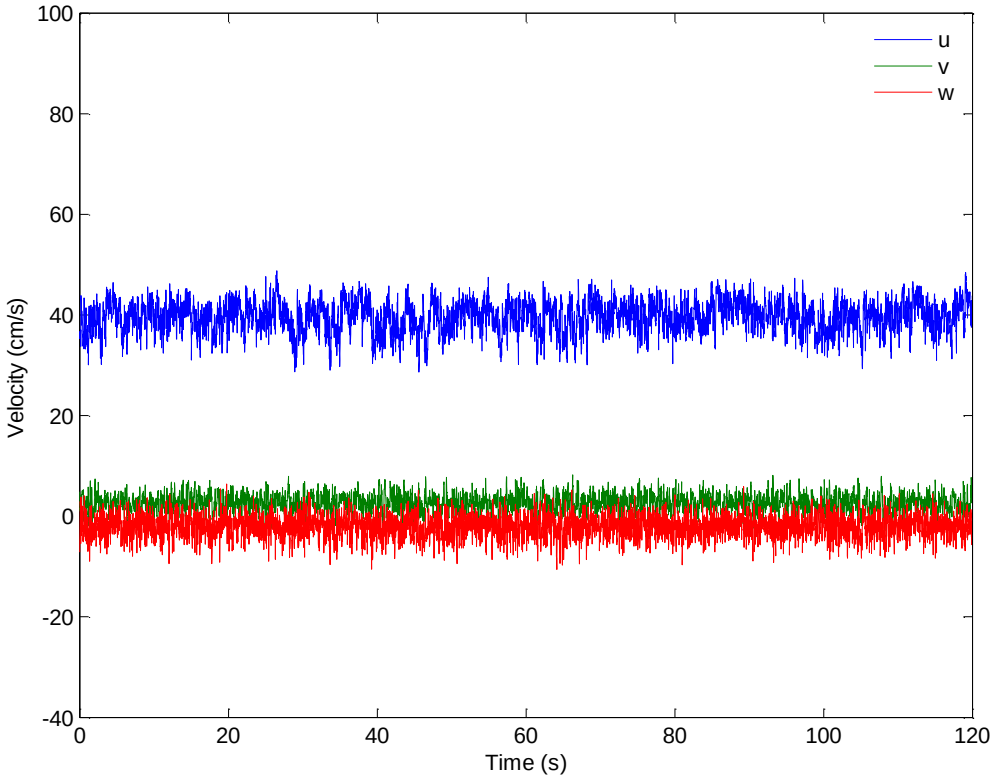

Test 7

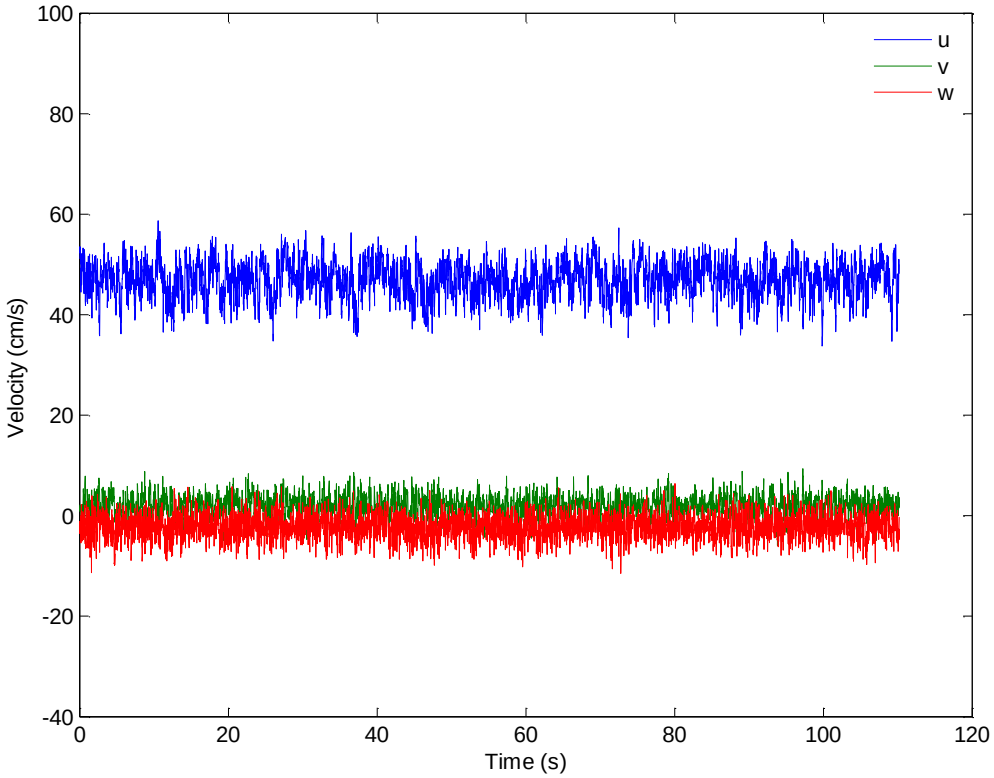

Test 8

Figure 20. continued

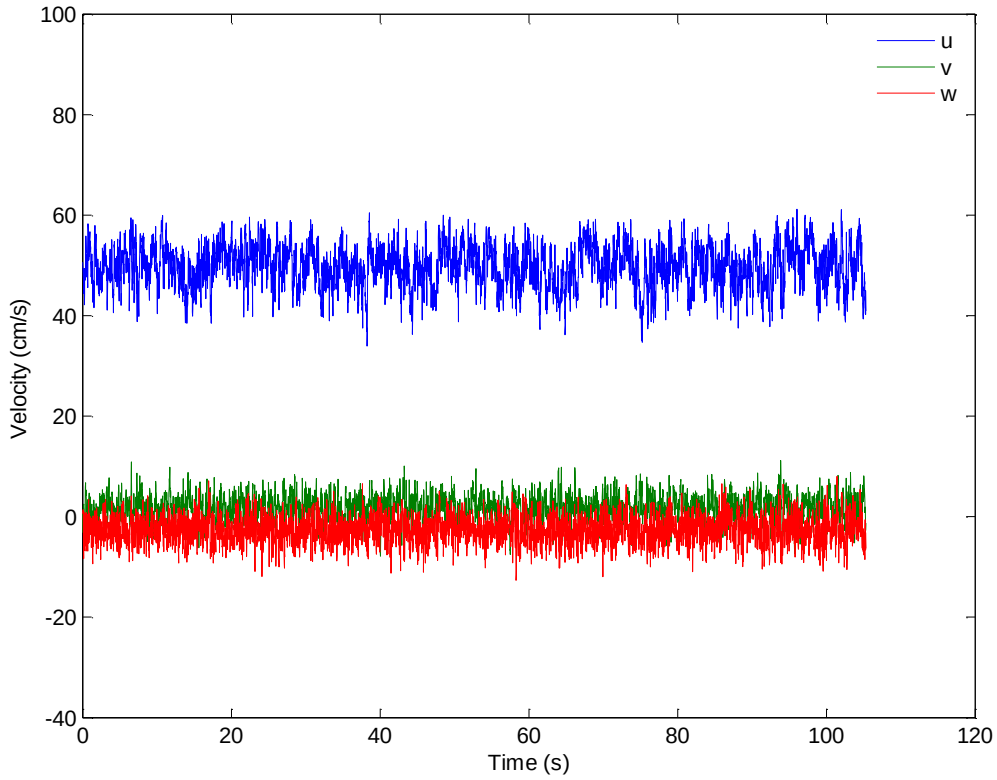

Test 9

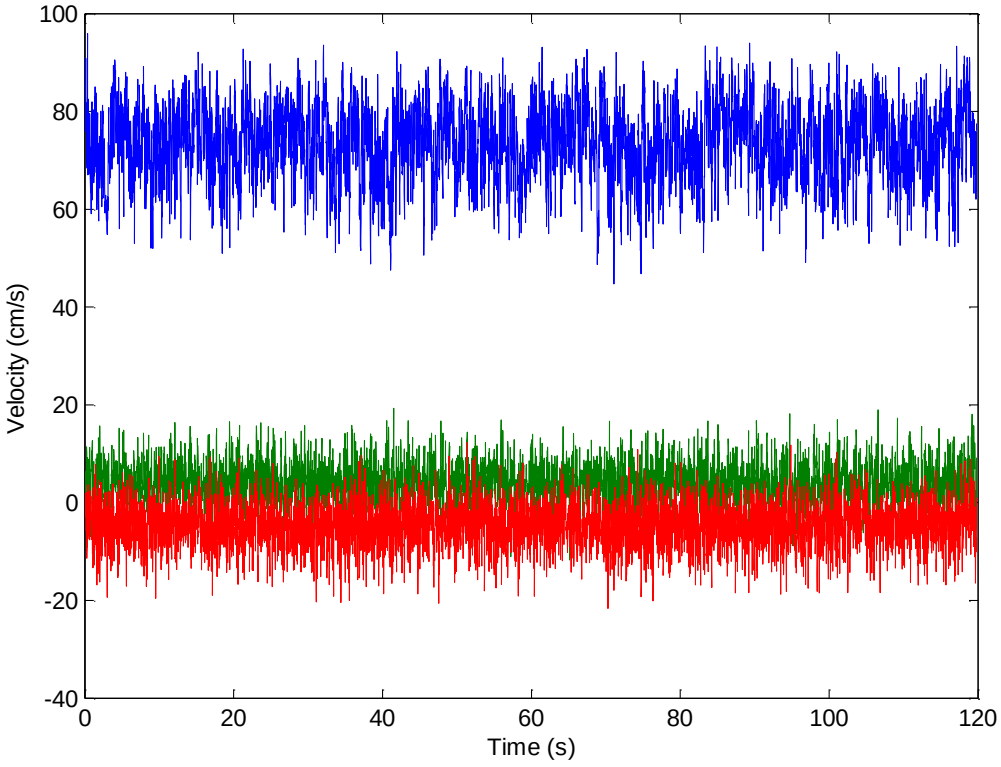

Test 10

Figure 20. continued

The time-series plots shown above indicate that the turbulent fluctuations are not the same in both channels. The test representative of the PIV flow visualization tests in the CE channel has much higher point-to-point variance than the tests performed in the wider and smoother BAE flume. However, there are also similarities between the time series measured in the two flumes. For all these time-series plots the streamwise velocity component of the velocity vector has much higher magnitude than the other directions, as is expected of a straight open channel, and thus the series within each test are ordered relative to magnitude as u > v > w and u is always positive, whereas, v is mostly positive and w is mostly negative.

Even though the point-to-point fluctuations have a considerable range of values for these different test channels and test conditions; however, the series representing either channel may be described as having potentially large cyclic patterns. Perhaps a cyclic structure is most evident in the data from Test 6 for the streamwise velocity u, resembling humps in the time-series with wavelengths between troughs measuring ~5 s and possibly an even larger wavelength ~10 s.

The major difference between the tests is that Test 5 has a higher amount of point-to-point fluctuation than the other tests with exception of perhaps Test 10. Statistical parameters describing the individual velocity components for the time-series shown above are listed below in Table 4 through Table 6.

Table 4. Streamwise velocity component time-series statistics

Test	5	6	7	8	9	10
Number of Samples	5,752	16,038	8,432	5,423	5,168	8,932
Maximum (cm/s)	93.65	52.40	50.07	58.68	61.18	96.90
Minimum (cm/s)	33.38	27.99	27.10	33.73	33.96	44.70
Average (cm/s)	65.37	41.79	39.67	46.96	49.82	73.59
Variance $(cm/s)^2$	70.33	13.14	9.79	12.90	17.87	59.74
Standard Deviation (cm/s)	8.39	3.63	3.13	3.59	4.23	7.73
Coefficient of Skewness $(cm/s)^3$	-0.32	-0.28	-0.31	-0.31	-0.27	-0.25
Coefficient of Kurtosis $(cm/s)^4$	3.14	2.84	2.88	2.92	2.82	2.75
Coefficient of Excess $(cm/s)^4$	-0.14	0.16	0.12	0.08	0.18	0.25

Table 5. Wall-normal velocity component time-series statistics

Test	5	6	7	8	9	10
Number of Samples	5752	16,038	8,432	5,423	5,168	8,932
Maximum (cm/s)	22.92	9.99	8.75	9.37	11.16	19.28
Minimum (cm/s)	-23.00	-7.06	-3.63	-6.04	-7.86	-11.76
Average (cm/s)	0.41	1.68	2.49	1.82	1.64	3.99
Variance $(cm/s)^2$	41.23	4.56	3.48	4.84	6.58	17.87
Standard Deviation (cm/s)	6.42	2.13	1.87	2.20	2.57	4.23
Coefficient of Skewness $(cm/s)^3$	-0.17	0.01	-0.05	-0.07	-0.07	0.04
Coefficient of Kurtosis $(cm/s)^4$	3.46	3.05	3.01	3.07	3.09	3.15
Coefficient of Excess $(cm/s)^4$	-0.46	-0.05	-0.01	-0.07	-0.09	-0.15

Table 6. Spanwise velocity component time-series statistics

Test	5	6	7	8	9	10
Number of Samples	5,752	16,038	8,432	5,423	5,168	8,932
Maximum (cm/s)	9.08	7.77	6.42	6.39	8.04	12.33
Minimum (cm/s)	-21.34	-12.22	-10.60	-11.47	-12.70	-21.64
Average (cm/s)	-6.13	-1.94	-2.06	-2.25	-2.62	-4.68
Variance $(cm/s)^2$	19.52	5.88	4.96	5.78	7.18	20.50
Standard Deviation (cm/s)	4.42	2.43	2.23	2.40	2.68	4.53
Coefficient of Skewness $(cm/s)^3$	-0.18	-0.17	-0.21	-0.13	-0.02	-0.17
Coefficient of Kurtosis $(cm/s)^4$	3.13	3.27	3.22	3.14	3.25	3.29
Coefficient of Excess $(cm/s)^4$	-0.13	-0.27	-0.22	-0.14	-0.25	-0.29

These statistics reveal that with respect to turbulent properties the u-series variance is the highest variance for all these tests. Interestingly, the vertical fluctuations indicated by the v-series variance is larger than spanwise w-series variance for Test 5 and vice versa for the other tests. Test 5 had the highest total variance, or turbulence intensity, although Test 10 is very close and in fact the w-series variance is slightly higher for Test 10 than for Test 5.

For all these tests the calculated u-series coefficient of skewness is negative and in a narrow range between -0.25 and-0.32. The v-skewness ranged -0.17 to 0.04 where Test 5 and Test 10 are the lower and upper values, respectively. Coefficient of w-skewness is negative and in a narrow range -0.18 to -0.02 and Tests 5 and 10 have nearly the same value. Past research has shown that skewness is related to the passing of coherent structures through the measurement region of the fluid domain (Wang and Larsen 1994; Balachandar and Bhuiyan 2007).

The u-series coefficient of kurtosis is in the range 2.75-3.14 with Test 10 and Test 5 forming the smallest and largest values, respectively. A Gaussian (normal) distribution has a value 3. The v-kurtosis ranges from 3.01 to 3.46, with Test 5 the highest, and the w-kurtosis is in a narrow range from 3.13 to 3.29 where Test 5 and Test 10 are the lower and upper values, respectively. The u-excess is negative for Test 5 and positive for the other tests with Test 10 having the highest value, v-excess is negative for all tests and Test 5 is the most negative, and, w-excess is negative for all tests and Test 10 is the most negative.

From the statistics it is clear that the average three-dimensional turbulence intensity determined from the ADV device (for example Test 5 = 0.04) reflects a high amount of turbulence intensity compared to, for example, a set of experiments performed in a wind tunnel with fine mesh at the inlet, where the intensity may be as low as 0.0002 (Schlichting and Gersten 2000). This is expected in the case of gravel-bed flows and validates the need for turbulence decomposition methods.

These results indicate that the average flow is nearly two-dimensional at the channel half-height, however all tests have mean flow into the spanwise direction as the w-series average value was non-zero in all tests. This may be indicative of secondary circulations present in the location of the ADV probe. The unfiltered time-series plots and statistical results do not tell us much about the coherent structures other than cyclic variations may be present in an otherwise nearly random set of point-to-point fluctuations. These time-

series indicate that it may be possible for large, cyclic structures to exist on the mean flow depending on the flow depth and other parameters including. Next a time-series decomposition method is described to further investigate the similarities between the structure of these data for all these test conditions.

4.2 Turbulence Decomposition and Characterization of Temporal Structures

Separation of the total velocity vector into three parts is a way of defining turbulent scales associated with small, intermediate and large eddies as described in Yalin (1977) based on a statistical method introduced by Hussain and Reynolds (1972). The method can be described by writing the velocity time series in the form (Fox *et al.* 2005):

$$u_i(t) = \bar{u}_i + u_i'(t) = \bar{u}_i + \hat{u}_i(t) + u_i''(t)\,. \qquad (1)$$

In Equation (1) the mean $\bar{u}_i$ is the average shown in the above tables of time-series statistics. The total turbulence is statistically represented by the series variance written $u_i'(t)$, which is decomposed in equation (1) into large-scale, or, slowly fluctuating components $\hat{u}_i(t)$ by using a low-pass, moving-average filter. This method has been applied in past research, e.g. Muller (1982), Tamburrino and Gulliver (1999) and Fox et al. (2005). The method is a temporal version of the large-eddy simulation (LES) decomposition which will be described further in the section on spatial decomposition methods. The temporal version is also known as triple-decomposition when the variance is further subdivided into two parts consisting of the slower fluctuations written in the form

$$\hat{u}_i(t) = \left(\frac{1}{2n+1}\right)\sum_{t-n}^{t+n} u_i(t) - \bar{u}_i\,, \qquad (2)$$

and $u_i''(t)$ are the remaining faster fluctuations that represent the smaller-scale eddies. Once the large-scale field is obtained from the moving-average filter, the small-scale field is constructed from Eq. (1). The moving average is applied over the time interval T = (2n+1)/f, where n is the number of data points on either side of the value being averaged and f is the ADV sampling frequency of 50 Hz.

Interpretation of the time interval used to filter the turbulence was performed with the aid of autocorrelation and spectral analysis. In turbulence research the spectral function is defined by the Fourier transform of the normalized autocorrelation function as:

$$S(\omega) = \tfrac{1}{2\pi}\int_{-\infty}^{\infty} r(\tau)e^{-i\omega\tau}d\tau\,, \qquad (3)$$

where $\omega = 2\pi f$ is the angular frequency and $f = 1/p$ where p is the period of the fluctuation (eddy) and is interpreted as the frequency distribution of the percentage of the square average of the fluctuations $\overline{u'^2}$ (Schlichting and Gersten, 2000). Autocorrelation coefficients were defined by

$$r(\tau) = \frac{\overline{u'(t)u'(t+\tau)}}{\overline{u'^2}}\,, \qquad (4)$$

from which integral time scales were estimated as:

$$\Im \equiv \int_0^\infty r(\tau)d\tau \,. \tag{5}$$

First the ensemble averages were subtracted from the instantaneous time-series data, resulting in a plot of the total turbulence time-series $u_i'(t)$ (not shown). Then the normalized correlation tensor was calculated, which has components of autocorrelation coefficients shown in Figure 21 and cross-correlation coefficients shown in Figure 22, each having six plots representing six different tests. Each plot in Figure 21 and Figure 22 contains three data series representing streamwise, u', vertical v' and spanwise w' normalized autocorrelation, denoted by time lag variable "τ" or cross-correlation coefficients denoted by time lag variable "tau". These plots, for example Test 5 in Figure 21 shown below, indicated differences in correlation functions that depend on direction, e.g. typically the blue (u') series is more highly correlated with itself for longer times than the green (v') and red (w') series. The size of the region in which the streamwise velocity fluctuations (u') are correlated changes depending on the test conditions and much larger for Test 9. Although the plots below have been truncated to 3 s time windows, the entire correlation series were used for further analysis. For all tests the autocorrelation and cross-correlation were not significant beyond the 3 s time windows and tended to stabilize near zero with high frequency point-to-point fluctuations not distinguishable between series.

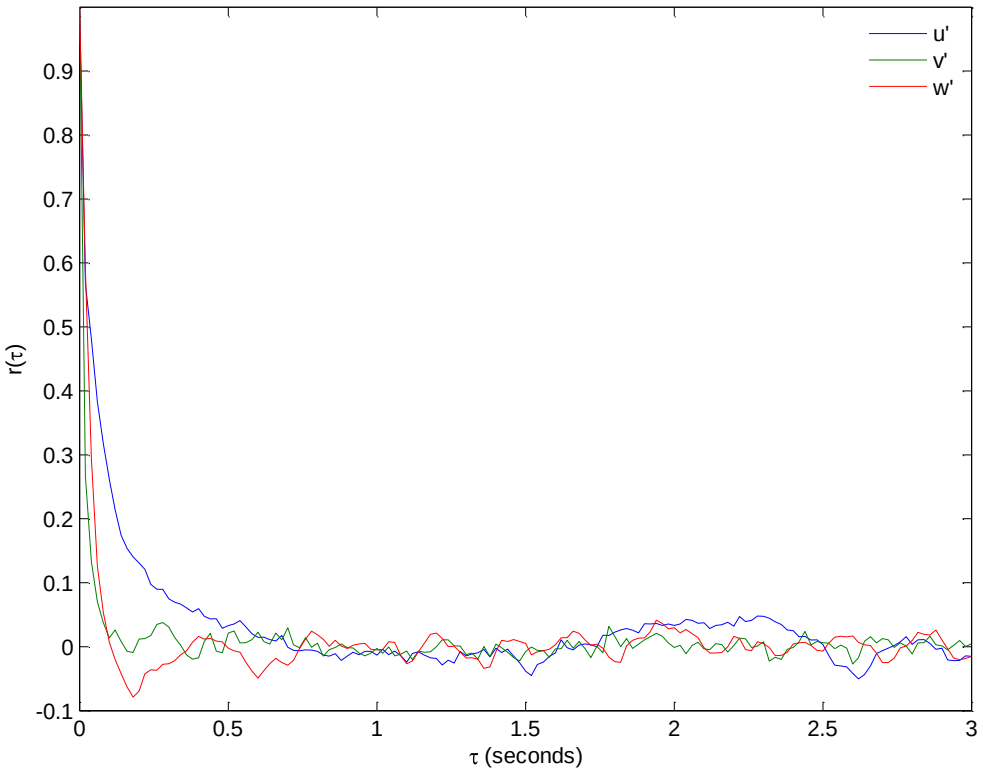

Test 5

Figure 21. Autocorrelation

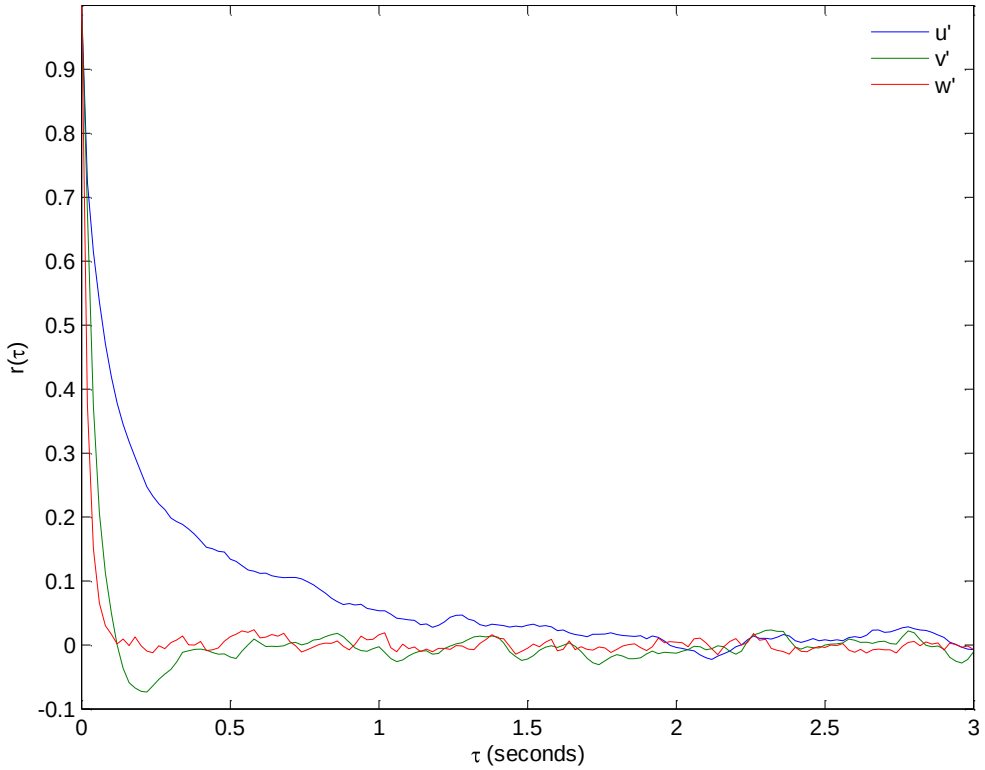

Test 6

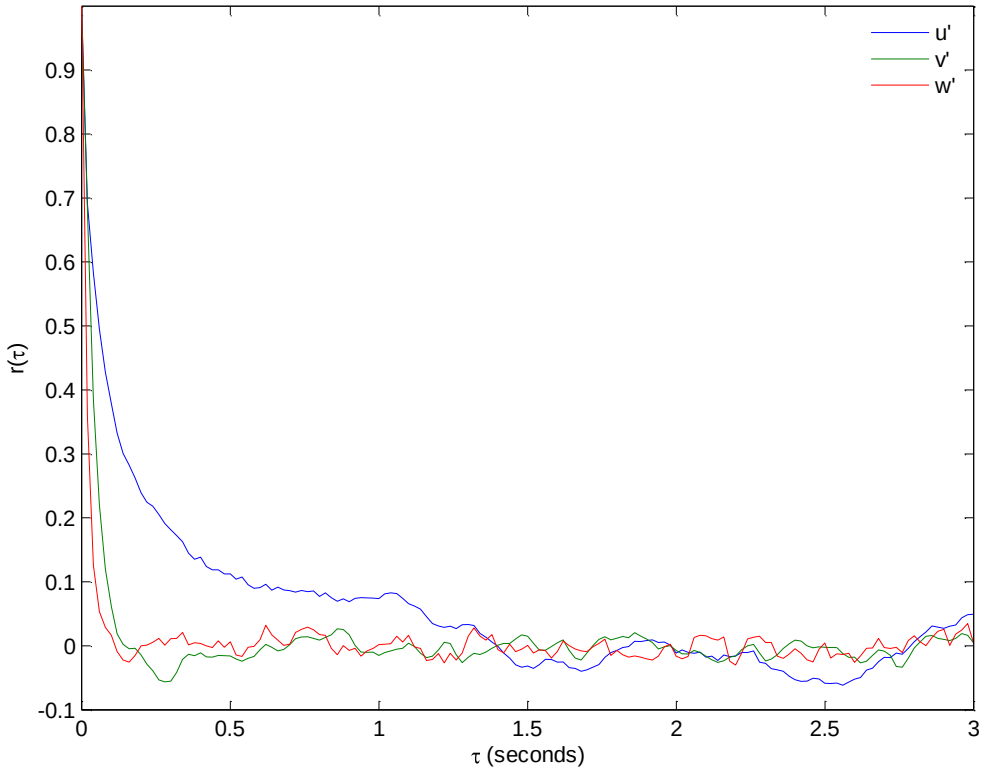

Test 7

Figure 21. continued

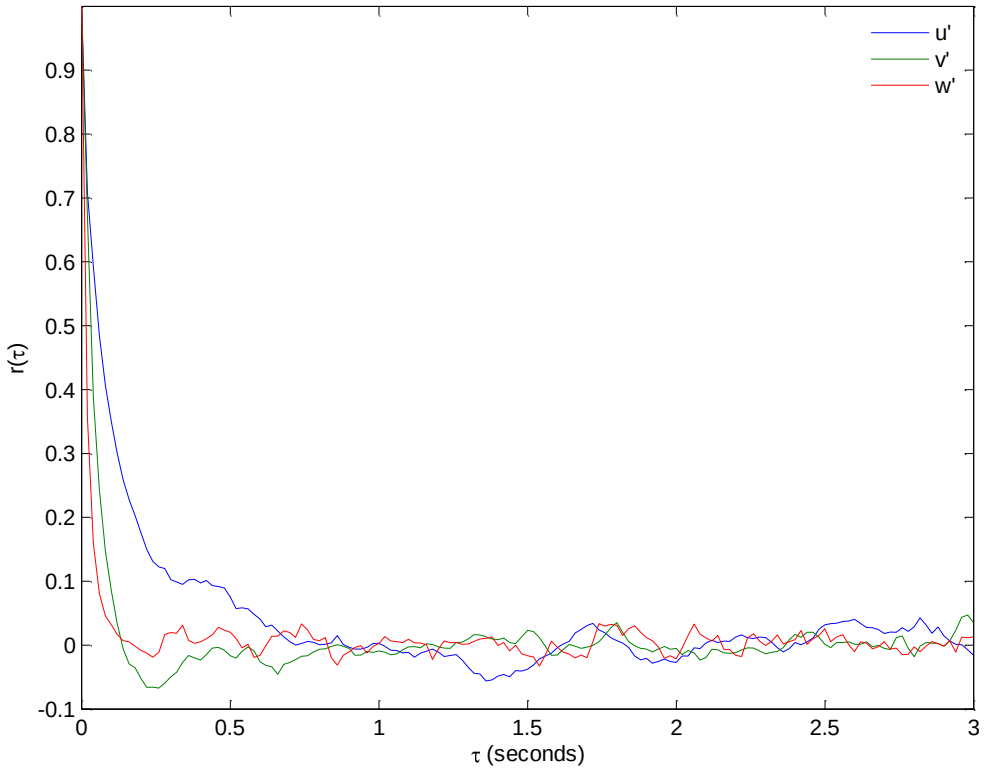

Test 8

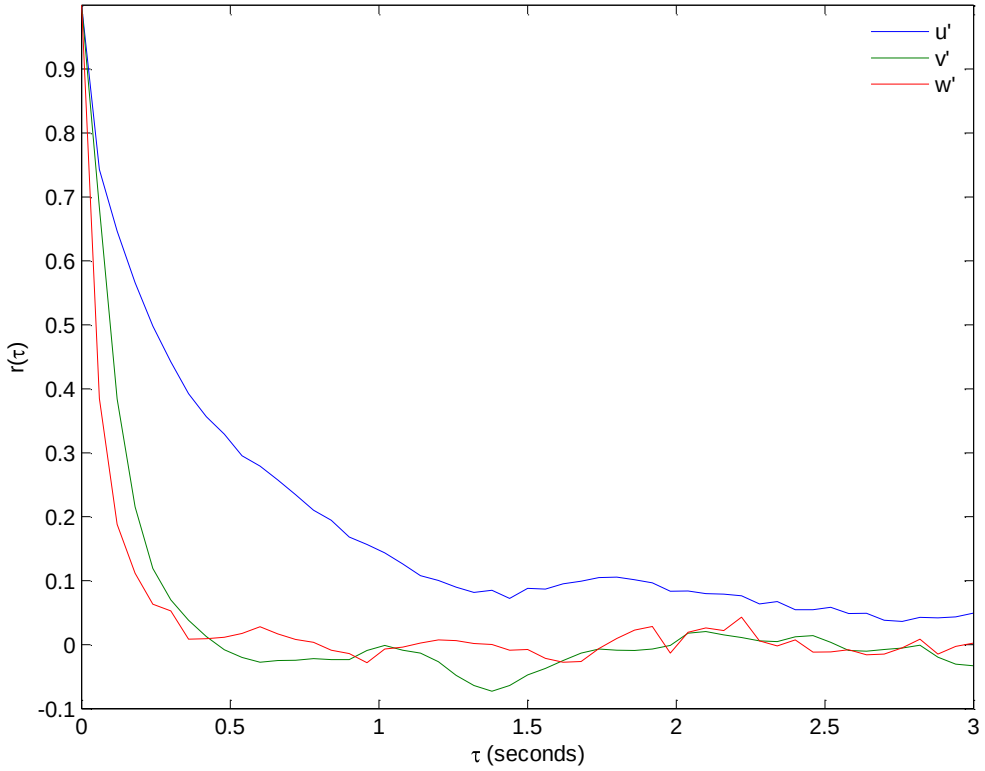

Test 9

Figure 21. continued

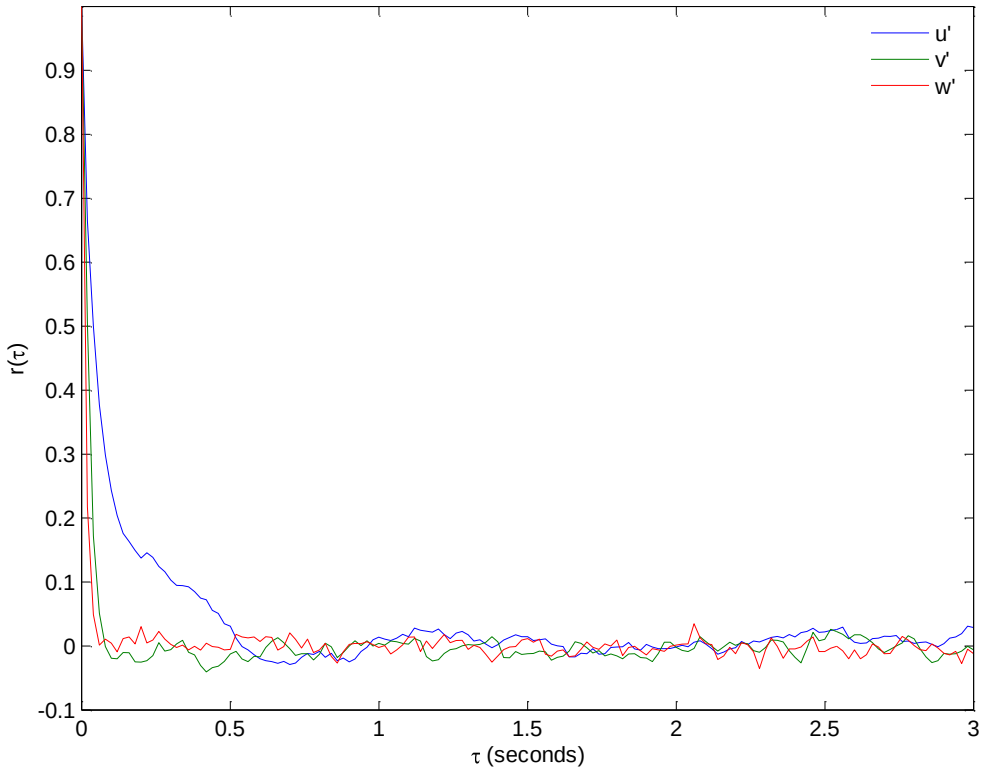

Test 10

Figure 21. continued

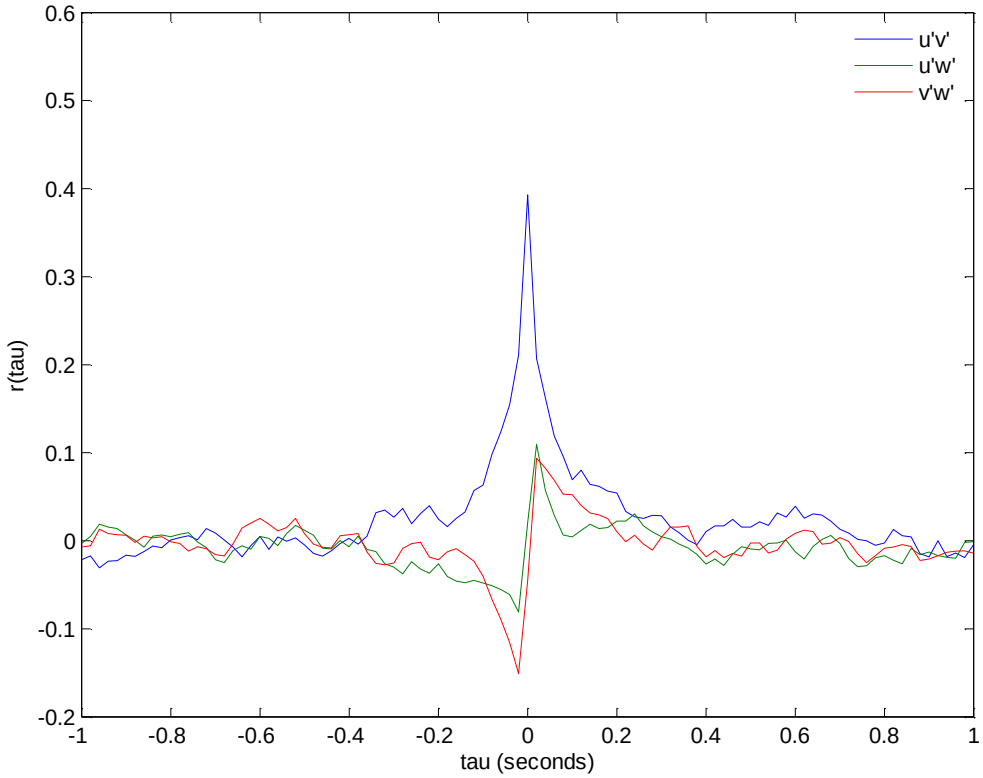

Test 5

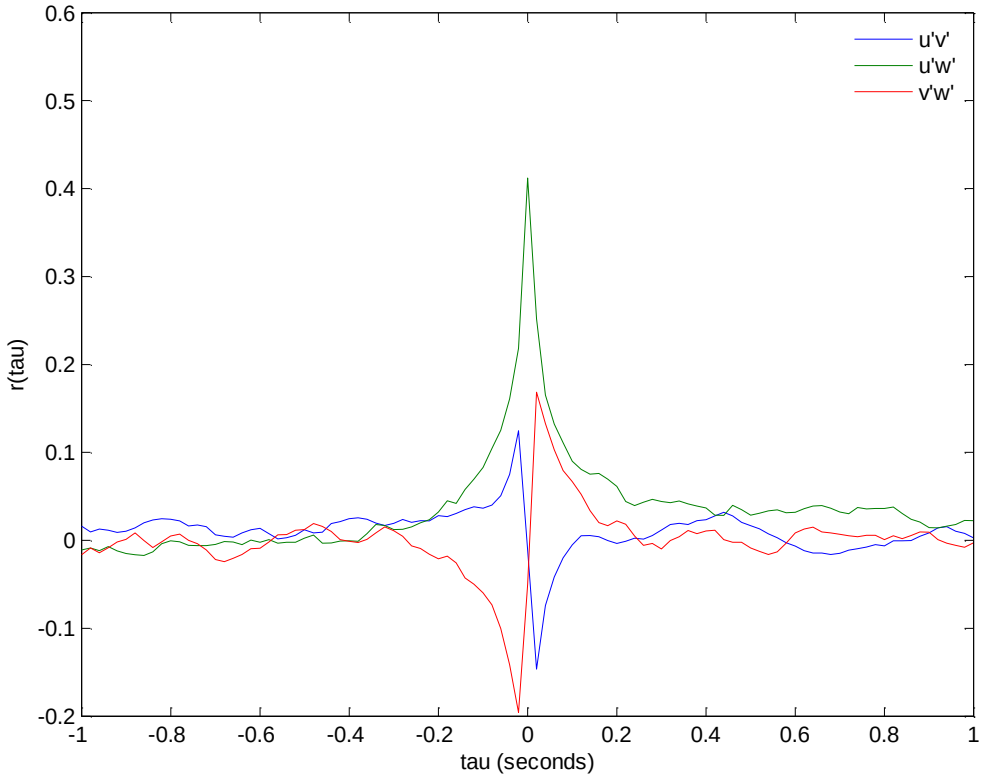

Test 6

Figure 22. Cross-Correlation

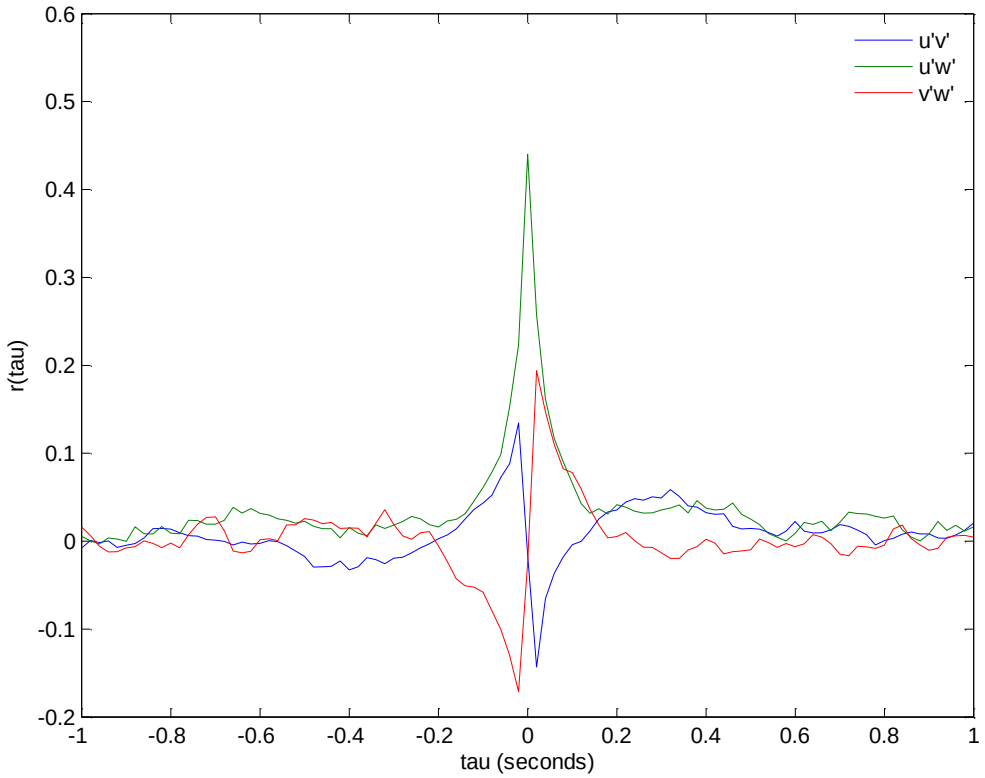

Test 7

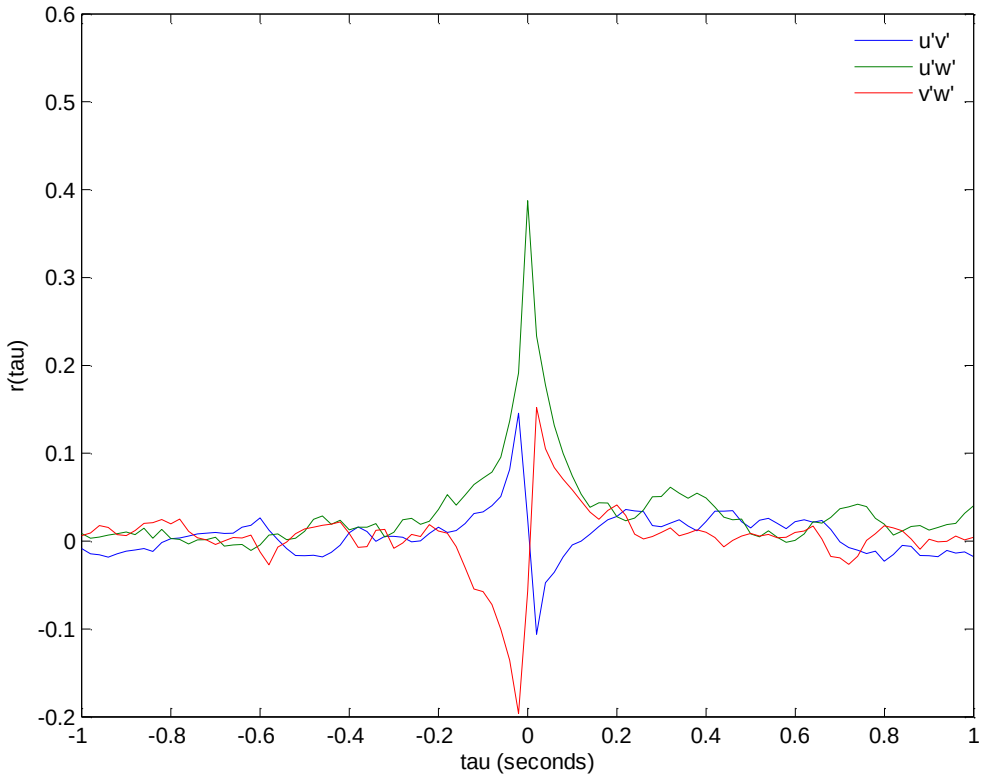

Test 8

Figure 22. continued

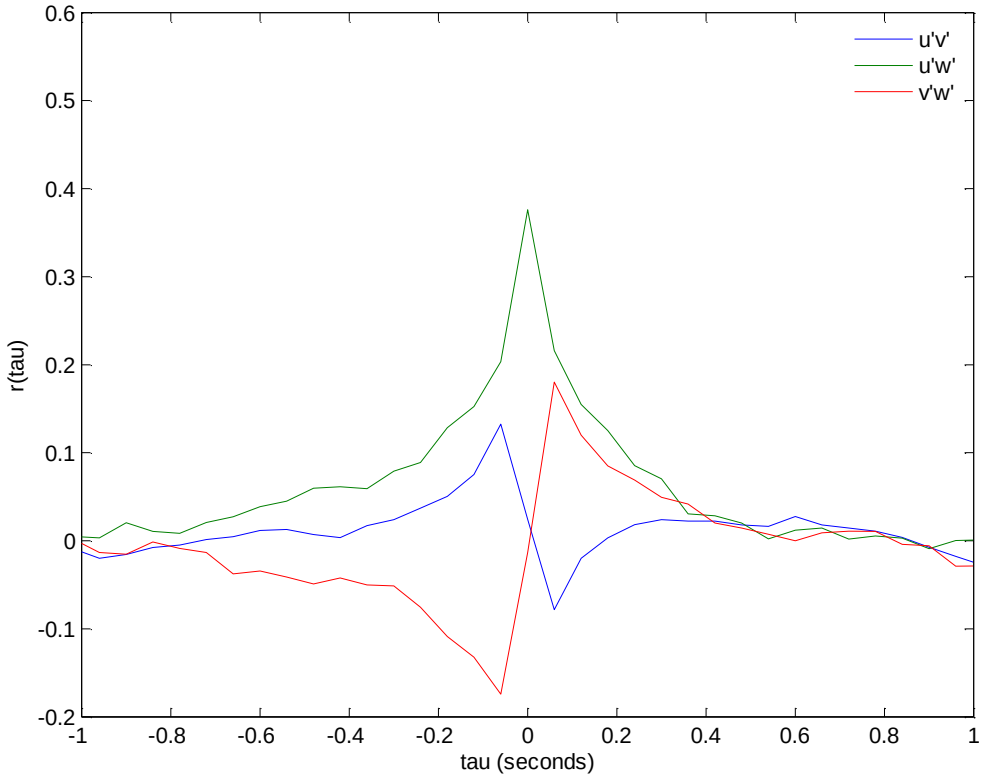

Test 9

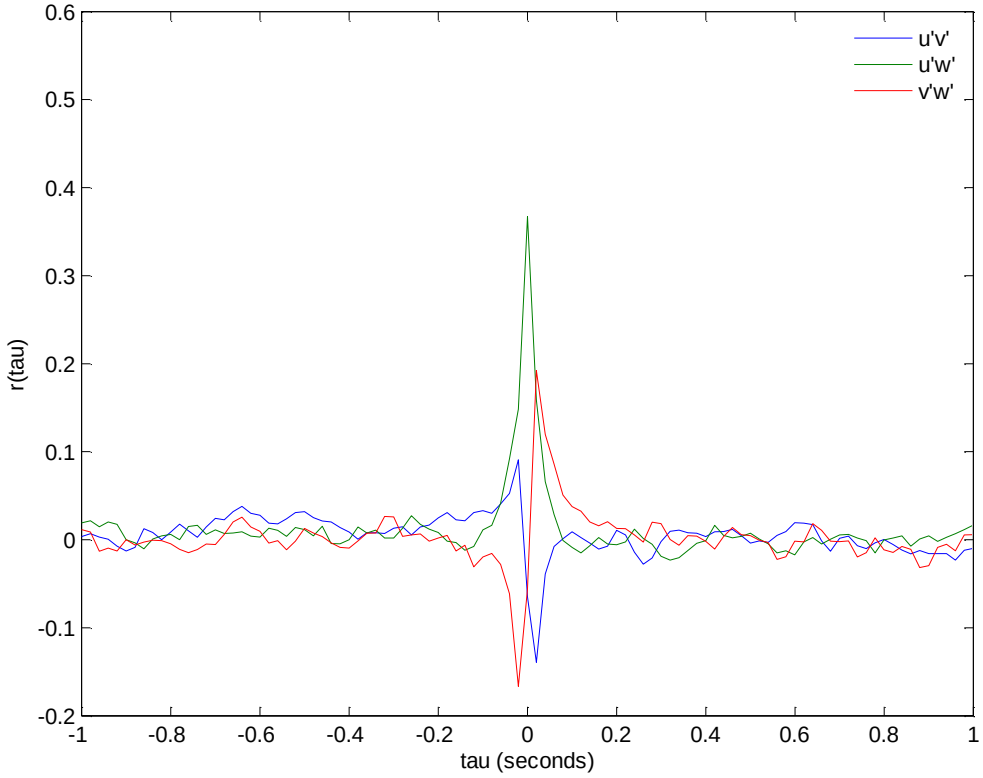

Test 10

Figure 22. continued

The correlation coefficient plots indicate that for all tests the streamwise fluctuations, u', are correlated for larger lag distances than the vertical, v' and spanwise w' series. Test 9 is unique in that the time for which autocorrelation is statistically significant exceeds that of the other tests considerably.

The cross-correlation patterns are not the same in the two channels. In the CE Flume the u'v' Reynolds stress is more dominant; whereas, in the BAE Flume the u'w' Reynolds stress is more dominant, suggesting a possible feedback mechanism involving the channel width, reduced roughness scale, or combination of flow parameters. The behavior in the v'w' cross-correlation is similar for all tests (both flumes).

Next the spectral density function was calculated with MATLAB and plotted in Figure 23, where the argument of the spectral function has been transformed by converting to wavenumber space from frequency space. The previous plots do not contain any smoothing, i.e. the data points are connected by straight lines. This is not the case of the spectral density function. Here the plots are shown as a continuous function which best fits the data and are smoothed as little as possible. For smoothing a numerical method in MATLAB was used which returns the B-form of the smoothest function that lies within a given tolerance, ϵ, of the given data points. This smoothing function may have any parameter value however non-zero values are only useful for smoothing the data in the spectral density plots and not for further calculations. Any estimates of large-scale phenomena, i.e. the lowest wavenumbers, were inferred by interpolating directly between peaks in small groups of adjacent data points without smoothing. The presence of large-scale eddies are expected to produce peaks in the graph of the spectral density function at the lowest wavenumbers. The SPAPS smoothing spline was implemented in MATLAB with parameter values shown in Table 7. A value $\epsilon = 0$ returns a cubic spline interpolation of the data and values as small as possible were found by a trial and error approach such that peaks observable in the lowest wavenumbers shown in the plots are the same peaks identified by setting $\epsilon = 0$. A unique tolerance parameter was found for each component (u,v,w) and then assumed constant for the next test upon which the trial and error procedure lead to the figures corresponding to the values shown in Table 7. Test 5 required the most smoothing, reflecting the high amount of turbulence intensity compared to the other tests.

Table 7. Smoothing spline tolerance parameter ϵ

	Test 5	Test 6	Test 7	Test 8	Test 9	Test 10
u	0.0029	0.0029	0.005	0.005	0.006	0.001
v	0.000003	0.000005	0.00001	0.00001	0.000009	0.000009
w	0.000064	0.000001	0.000004	0.000004	0.000005	0.000003

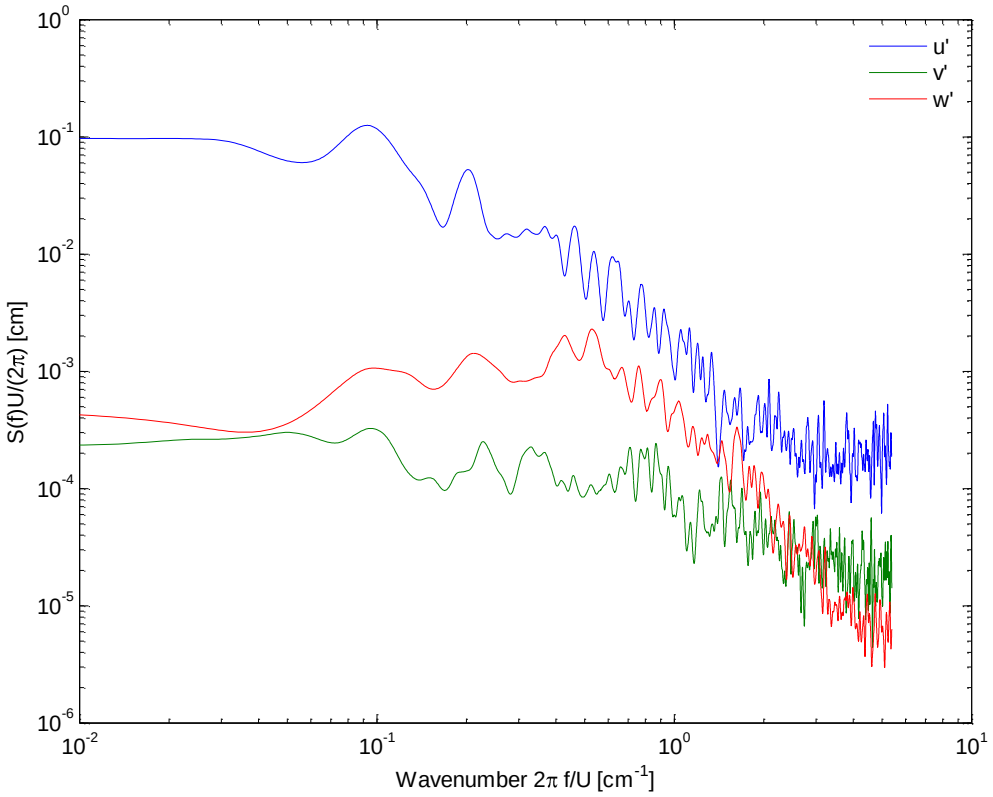

Test 5

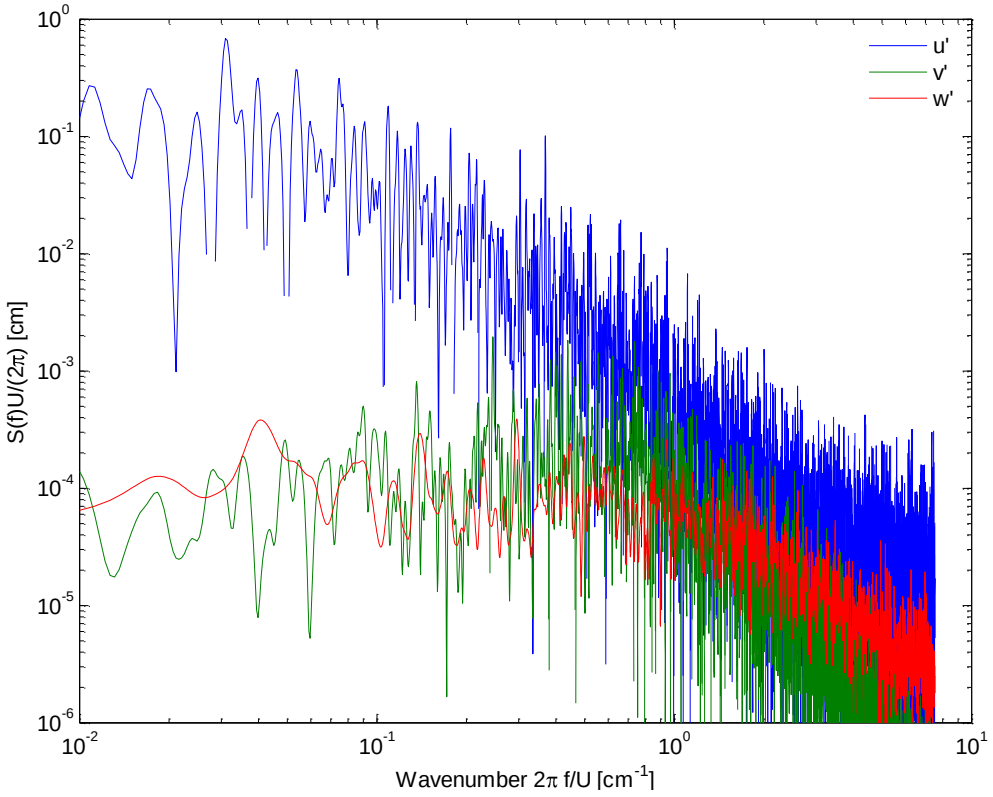

Test 6

Figure 23. Smoothed spectral density function

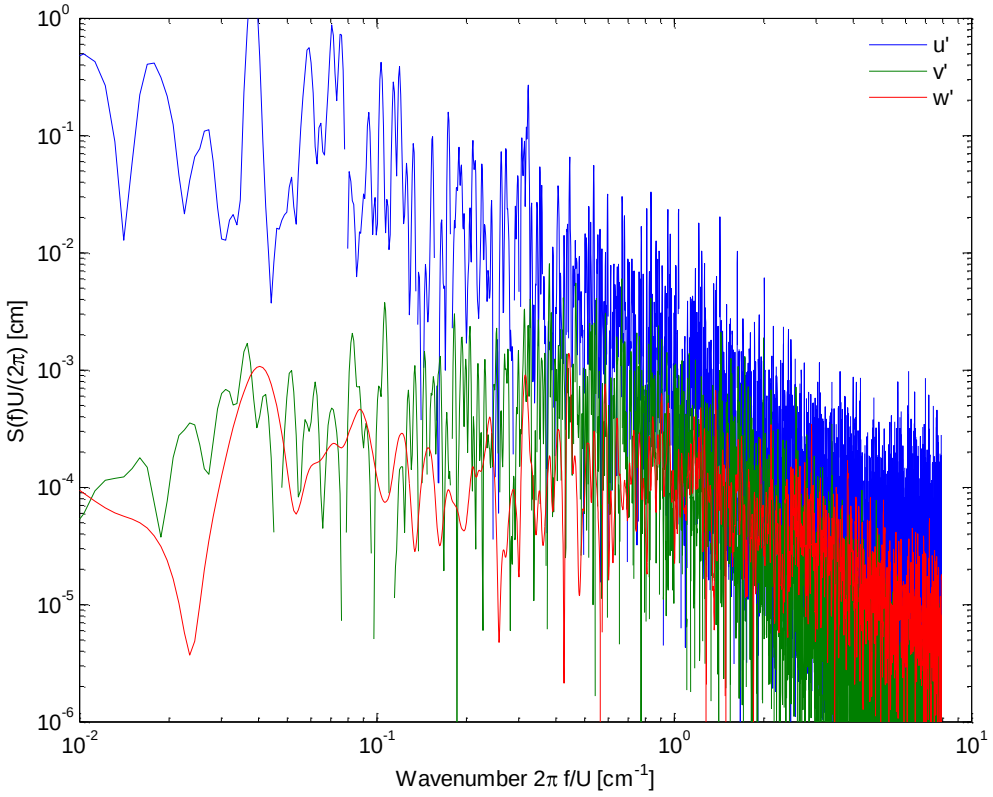

Test 7

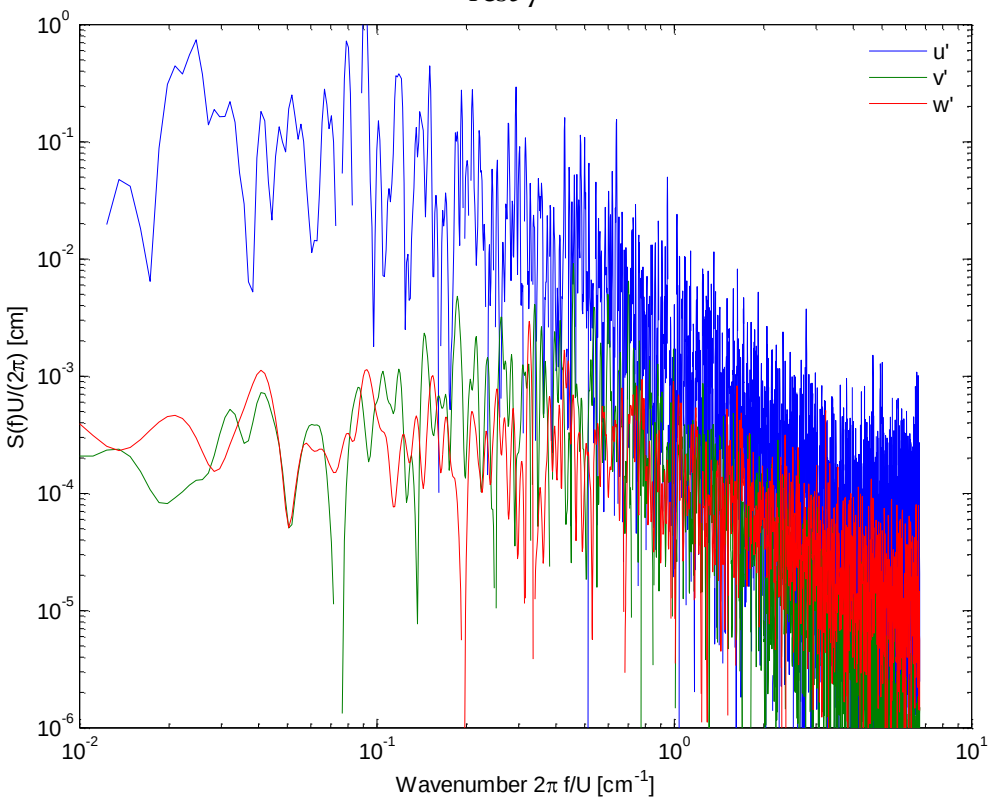

Test 8

Figure 23. continued

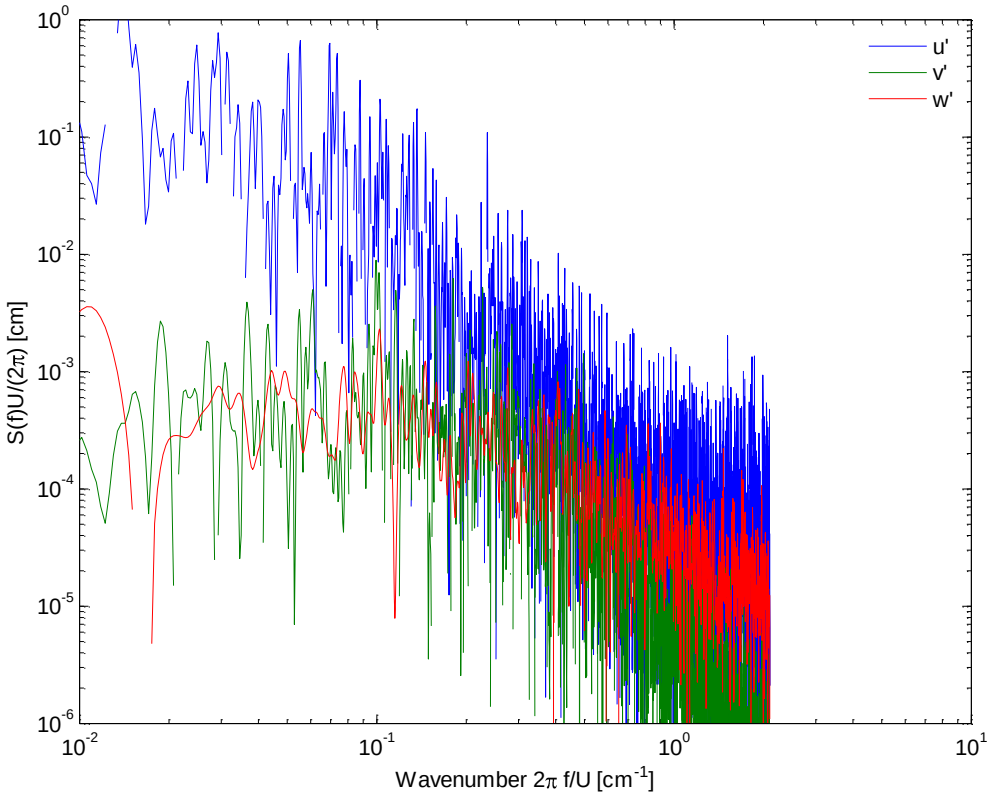

Test 9

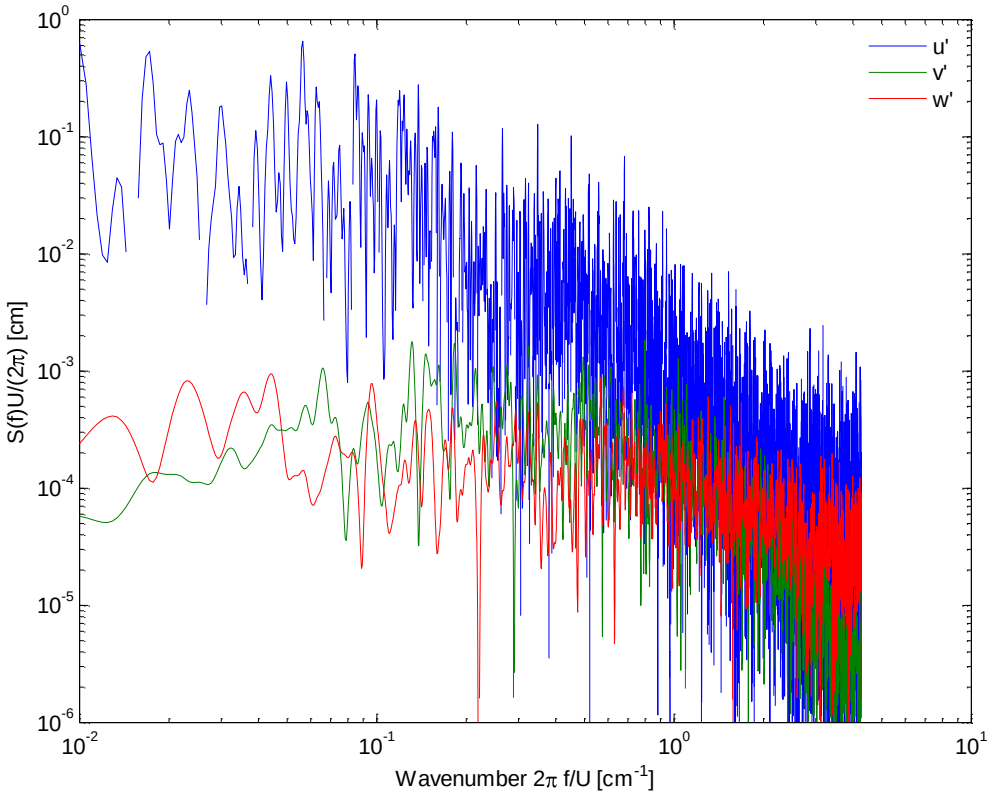

Test 10

Figure 23. continued

These spectral density function plots indicate that the u' series contains higher energy than v' and w'. The streamwise fluctuations, u', have spectral density plots that are nearly linearly sloping downward with similar slope for all tests at the upper end of the spectrum. The spectral density of the vertical and spanwise fluctuations exhibit broad peaks occuring in the central range of the spectra for all the tests, indicating a dominant large eddy size is easier to identify in these series than the u' series. Test 9 is unique in that w' has its largest peak at the lowest wavenumbers, a peak which contains more energy than the v' spectrum. The energy containing eddies have different length scales in the three directions and that these length scales vary with test conditions.

Finally, macroturbulent scales were estimated by numerical integration of the velocity autocorrelation functions. For consistency, a best-fit exponential function of the form:

$$r(\tau) = e^{-\tau/T} \tag{6}$$

was numerically integrated over the first 100 values of the time lag coordinate using a trapezoidal method, yielding an integral parameter T. The computed values of the parameter T represent macroturbulent time scales from which the length scales L were determined as $\overline{u}_i T_i$ for the i=1,2,3 components of the mean flow, as shown in Table 8.

Table 8. Calculated macroturbulent scales T (s) and L (cm)

	Test 5	Test 6	Test 7	Test 8	Test 9	Test 10
T_1	0.087	0.197	0.178	0.123	0.533	0.088
T_2	0.026	0.026	0.031	0.022	0.084	0.015*
T_3	0.019*	0.027	0.024	0.028	0.082	0.019*
L_1	5.07	8.23	7.07	5.79	26.55	6.46
L_2	0.05	0.04	0.08	0.04	0.14	0.06*
L_3	0.09*	0.05	0.05	0.06	0.21	-0.09*

* These scales are not possible to detect because they correspond to temporal lags $\tau < 0.02$ s; a lower limit is set by the sampling frequency of 50 Hz.

The estimated scales represent temporal and spatial dimensions of the average size of large eddies in the time-series u', v' and w'. The statistical analysis and the results shown in Table 8 indicate that in each test the streamwise dimension of this statistical eddy is about equal to the flow depth with one exception, Test 9, which had the deepest flow and the largest eddies, i.e. $L_1 \sim 3H$. Tests 5 and Tests 10 have similar length scales even though the flow parameters are very different. These streamwise results are consistent with the previously reported "large eddy" dimensions reported in the literature for observations in rivers and laboratory channels and thus supporting the hypothesis that the turbulence flow is structurally organized for these gravel bed conditions.

For each computed macroturbulent length scale a local peak may be identified in the spectral function which corresponds to a frequency associated with these dominant eddy scales in the inertial subrange, amidst a linear descending trend in the spectral function with increasing frequency.

The estimated correlation scales (temporal version) were used to define the filter width of the moving average in equation (2) resulting in the large-scale turbulence time-series plotted in Fig. 24, where only the streamwise series for each test are shown. Local

peaks and troughs in the following plots are understood to represent the larger-scale eddies as the variance associated with fluctuations smaller than the correlation length scales have been smoothed over. An arbitrary 40 s time window is shown for each test for comparison of large scale motions to see if any similarities exist in cyclic patterns of large scale eddies in time-series for the different test conditions.

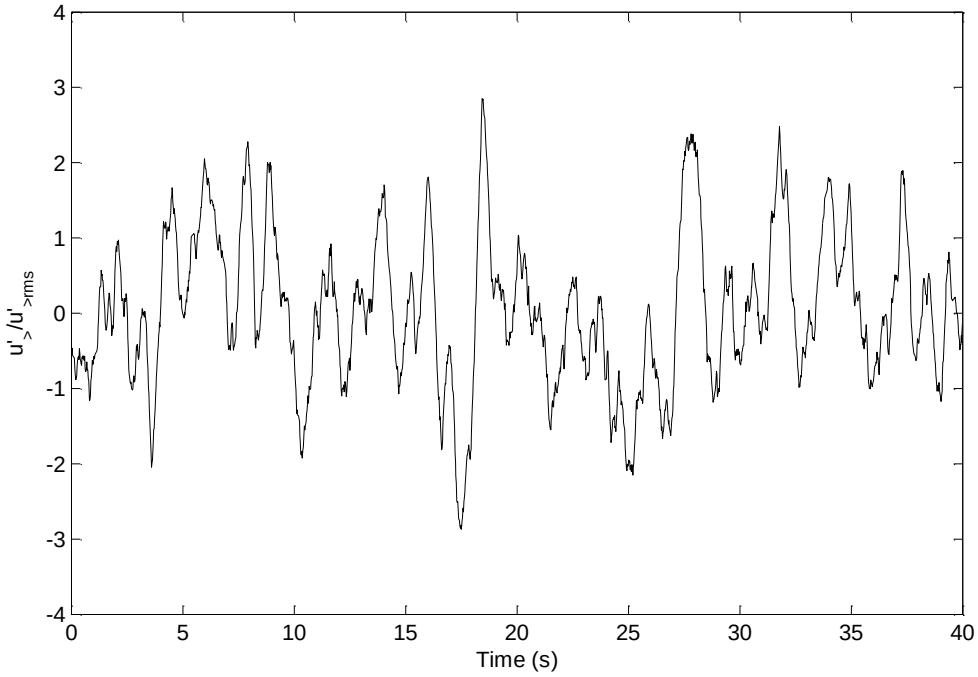

Test 5

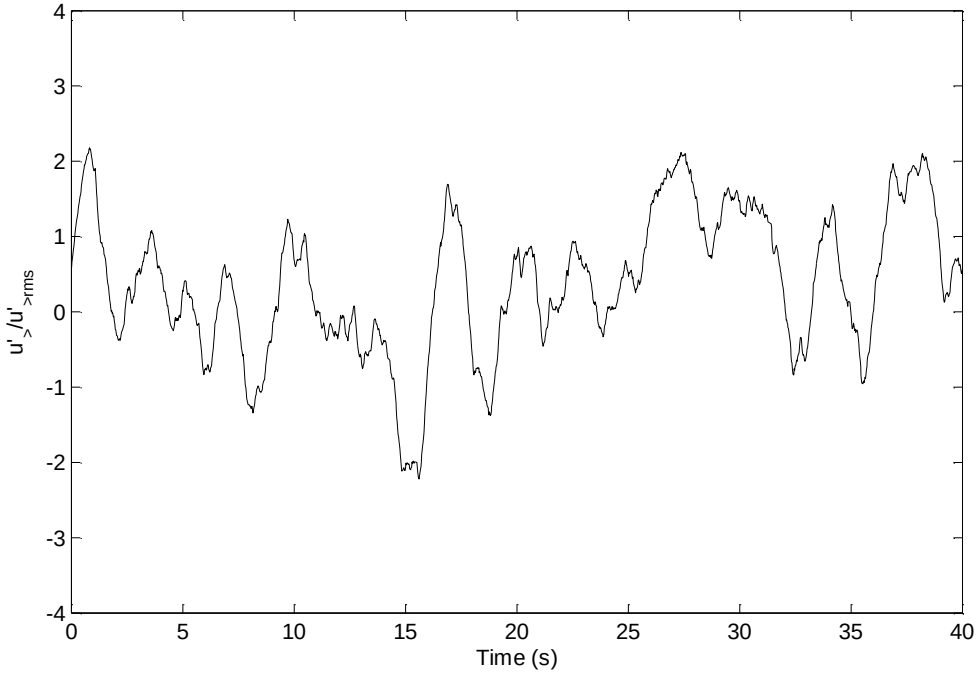

Test 6

Figure 24. Normalized large-scale streamwise fluctuations

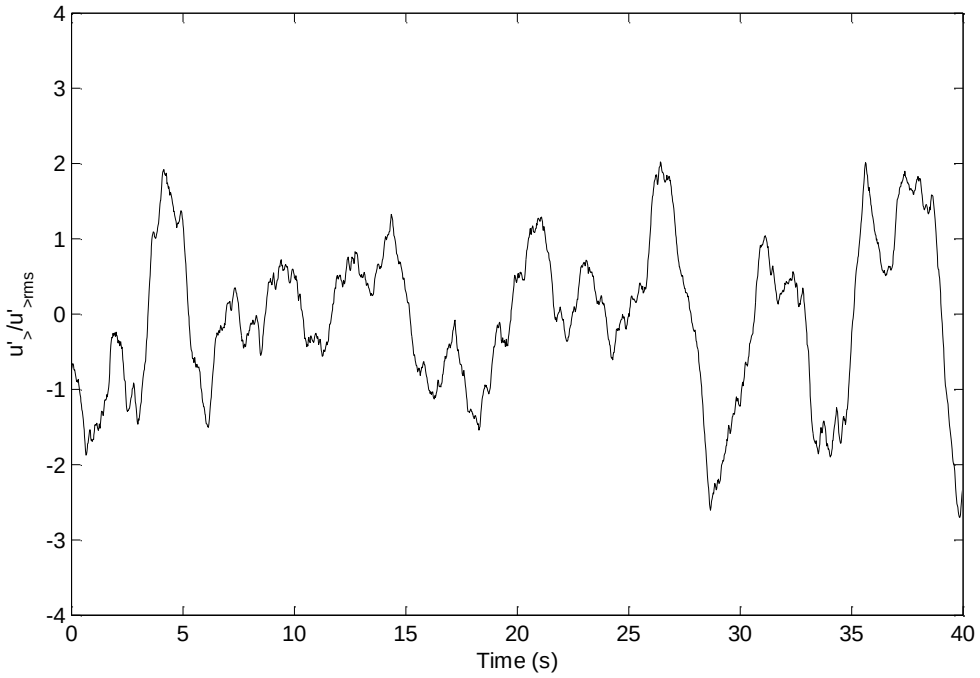

Test 7

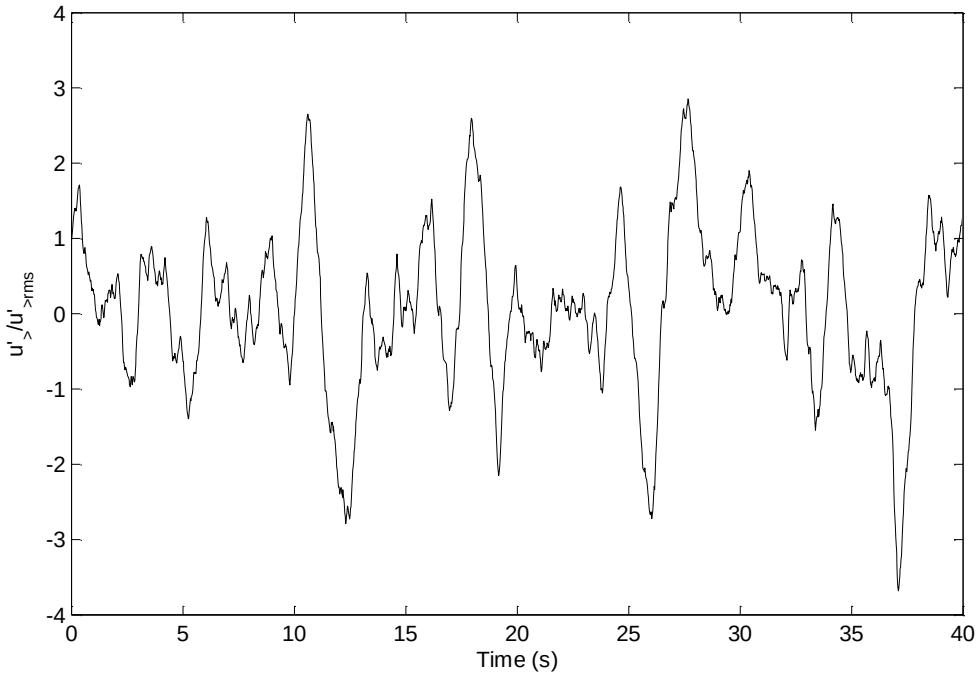

Test 8

Figure 24. continued

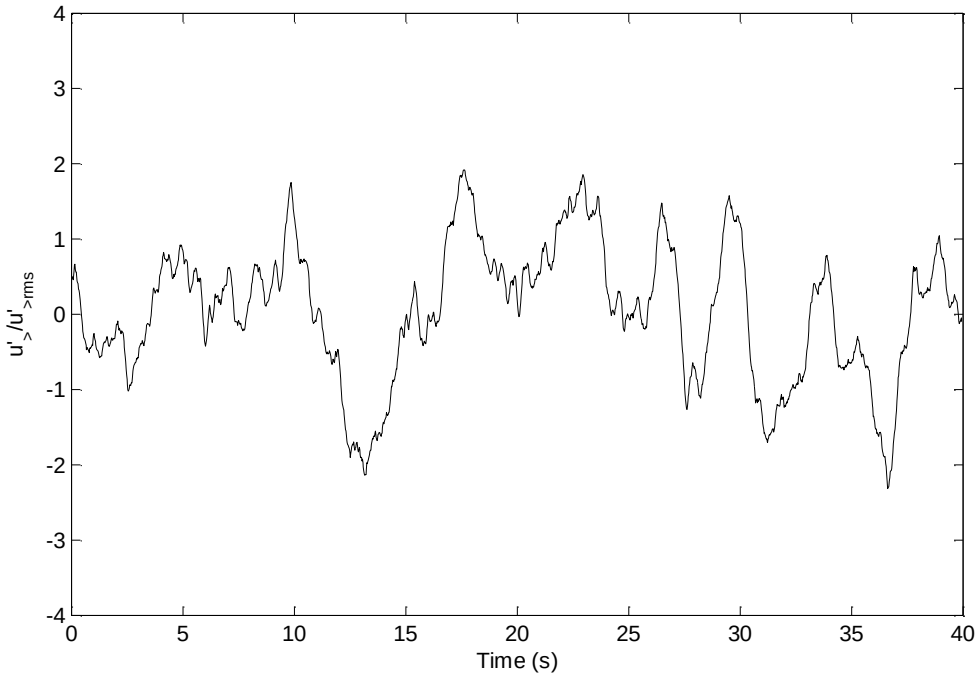

Test 9

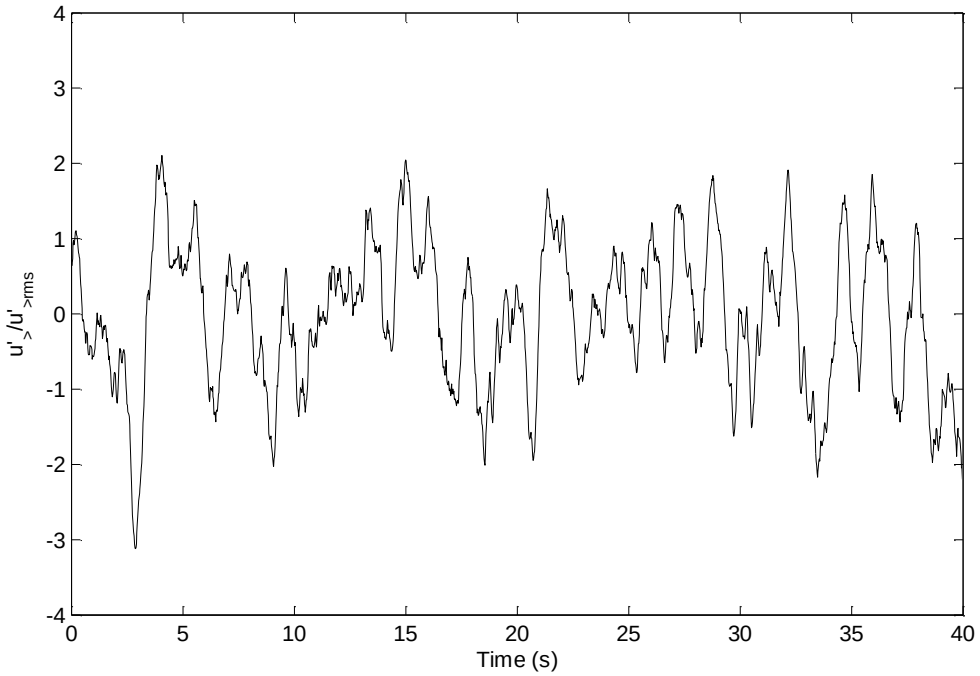

Test 10

Figure 24. continued

The time-series shown in Fig. 24 have similarities in that they all identify large-scale eddies as cyclic, broad peaks or troughs which have period on the order of 2.5 seconds or less, although the observed period is not the same for the different test conditions. The total variance is less for Test 9 than the other tests due to the longer moving-average time window based on autocorrelation length scales and it is easiest to identify the structure in this time-series that is also visible in the other tests, namely, a pattern of largest point-to-point variance between three consecutive data points, followed by packets of large peaks, usually in groups of about 4 but ranging from 3 to 6. For example, this large packet can be seen in Fig. 24, Test 9, beginning at t = 12.5 s and ending at t = 37 s, containing five local peaks of positive large-scale variance. The packets of large eddies in the time-series (Fig. 24) appear in groups lasting for a time period ranging from 5 s to 15 s and are the most spread out for Test 9. In general the packets are arranged in ~10 s groupings for all the tests. The finding that smoothed turbulent velocity time-series have a large-scale structure is similar to past research, e.g. Shvidchenko and Pender (2001), who have attributed similar structure to the passing of coherent structures and thus have been used to suggest that the flow contains turbulent structural organization.

The main point of the time-series analyses presented above has been to adopt a standard method for temporal decomposition that allows us to clearly define the notion of a large eddy as a structure in the variance in the streamwise velocity vector field and thus to support the hypothesis that the flow is structurally organized. It can be seen from the results that this statistical large eddy exists for both channels and in all test conditions. Much larger scale trends may exist in all of these time-series, for example, it appears that further smoothing would result in the identification of slow fluctuations with periodicity on the order of 1-min, most clearly identified in Fig. 24, Test 5 and Test 6. This interesting result may be attributable to even larger-scale coherent structures or cyclic processes which indicate a need for the use of spatial decomposition methods.

Another important result of the time-series analysis is that it allows us to make comparisons of temporal coherent structure to spatial coherent structure attributed to vortices or large eddies. The size of the peaks in the plot shown in Fig. 24, Test 5, indicates that the sampling window of the PIV equipment, which records approx. 4 s of sequential data, is adequate to bound one of these large peaks attributed to these large-scale eddies for identical flow conditions in the CE Flume, and thus it may be possible for us to identify the spatial structure of the velocity field which matches these large eddies in the statistical time-series analysis. The fact that similar decompositions performed for the BAE flume yield similar structure validates the hypothesis that turbulent structures organize vertical velocity fluctuations as large eddies may be observed in the streamwise fluctuating field.

4.3 PIV Results

Next the spatial composition of the velocity field in the CE Flume is examined in attempt to perform similar decomposition methods in order to educe the size and shape of the coherent structures responsible for the large-eddies in the time-series analysis and further assesses the structural organization of turbulence for the gravel bed flows. Next the average results of the PIV data for each test are shown in order to make some general comparisons of the spatial variations of the bulk velocity field.

The ensemble averaged PIV results are shown below in Figure 25 through Figure 40 for the experimental runs labeled as Tests 1-4. Here the results have been plotted using a consistent spatial resolution to compare large-scale flow patterns with spatial scales related to the flow depth for these tests. Below are the averages of the tensors returned by the PIV algorithm including mean velocity, mean vorticity and root-mean-square velocity fluctuations (Reynolds stresses). Probability of flow reversal, which is important for indicating the presence of turbulence and boundary layer separation near the gravel bed has also been computed and plotted in these figures. The latter was computed in MATLAB by comparing the direction of the streamwise velocity component at a point in space and time to the mean streamwise direction and assigning a cumulating value of 1 if the signs are different. This method was applied to each coordinate in the snapshot and then averaged over the ensemble to provide the spatial distribution of probability of flow reversal at a point. This type of plot can be useful to identify zones in the spatial field which have a high amount of temporal fluctuations and possible areas where flow separation from the boundary may be important long-term flow processes. The governing equations typically used in fluid analysis are the Navier-Stokes (N-S) equations; however, these equations do not apply to certain situations which involve shocks and other flow discontinuities (Holmes *et al.* 1998) such as in flow separation regions near the bed. Thus boundary layer formulations of these equations may not be solvable in regions which have a high probability for flow reversal. The probability of flow reversal plots give us an idea to what extent these flows may be modeled using boundary layer models of turbulence structure.

The point A, which is placed in the center of the image in the streamwise axis, x1, and at the flow half-depth on the x2 axis, represents the half-depth in each image. This point corresponds to the location of the ADV probe in Test 6 and allows for comparisons with the trends and large-eddy structure observed in the time-series plots shown above. It also allows us to examine the structure of time-series for mid-depths as the flow strength is varied for given channel geometric parameters and fluid properties. A goal is to understand why the length scales of large eddies may suddenly increase between test conditions, as suggested by comparison to the ADV data collected in a different channel under increasing flow strengths. Test 9 had much longer eddy scales than for other flows in the same channel and although exactly the same structures are not inferred to exist in the CE Flume, similar structures exist and therefore may also achieve maximum spatial scales for the right flow condition.

A time-series plot of the u-component at point A for each PIV tests is shown in Figure 41 for general comparison of temporal structure observed in the time-series plots of the ADV for Test 6. On each time-series have been superimposed the mean value at A as a dashed horizontal line and also limit lines set at plus and minus one standard deviation of the variance at A.

Spatial correlation scales were estimated for the tests similarly to the method used in the time-series analysis presented above. The spatial autocorrelation and cross-correlation functions were calculated for each coordinate using spatial lag units, fit the same exponential function as previously described in the time-series analysis of the ADV data, and similarly numerically integrated this function to get a length scale for comparison to the length scales listed in Table 8. For the PIV data, first the integral length scales were row-averaged, which averages in the streamwise direction, and then

ensemble averaged to get a plot of how the length scales vary with position relative to the average surface of the gravel-bed.

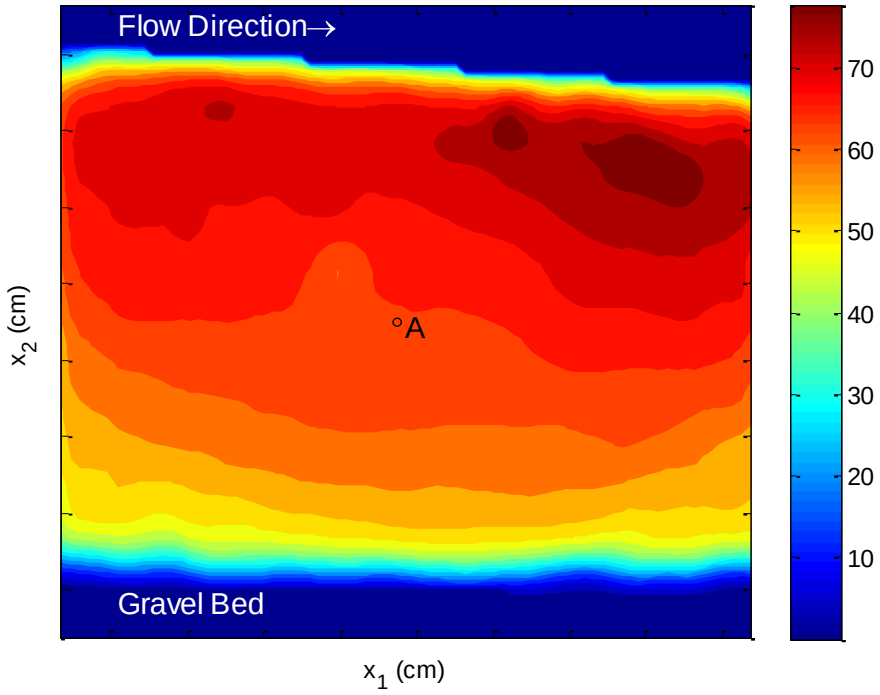

Figure 25. Test 1 Average Velocity Magnitude (cm/s)

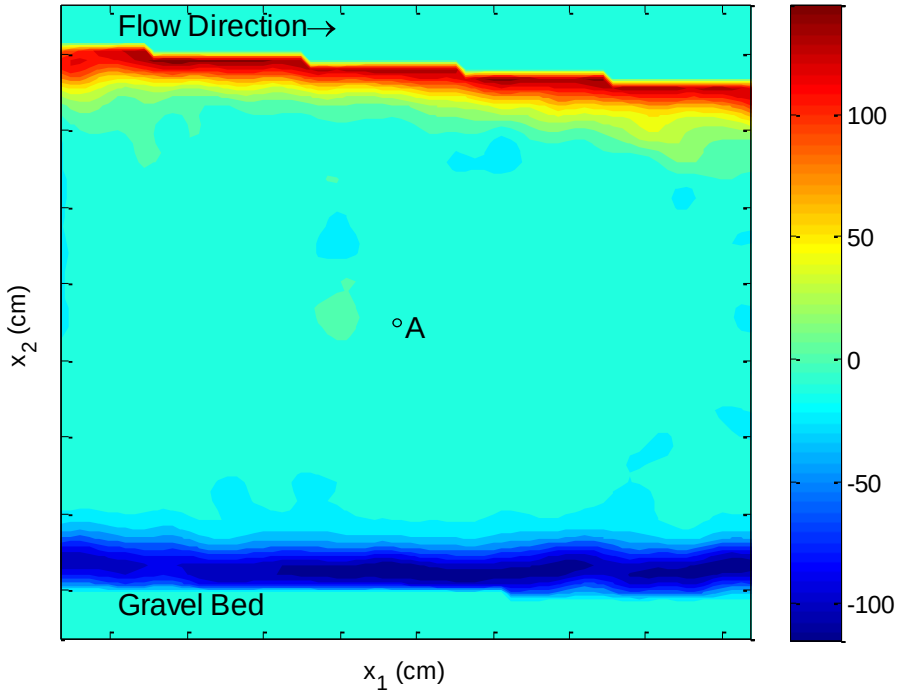

Figure 26. Test 1 Average Vorticity Magnitude (1/s)

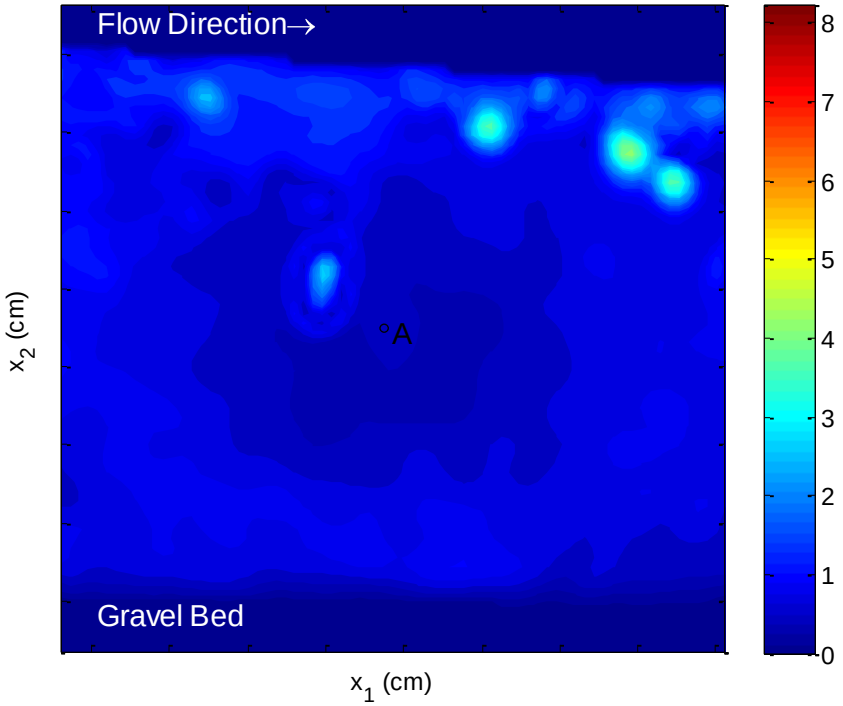

Figure 27. Test 1 Average Root-Mean-Square Velocity Fluctuations

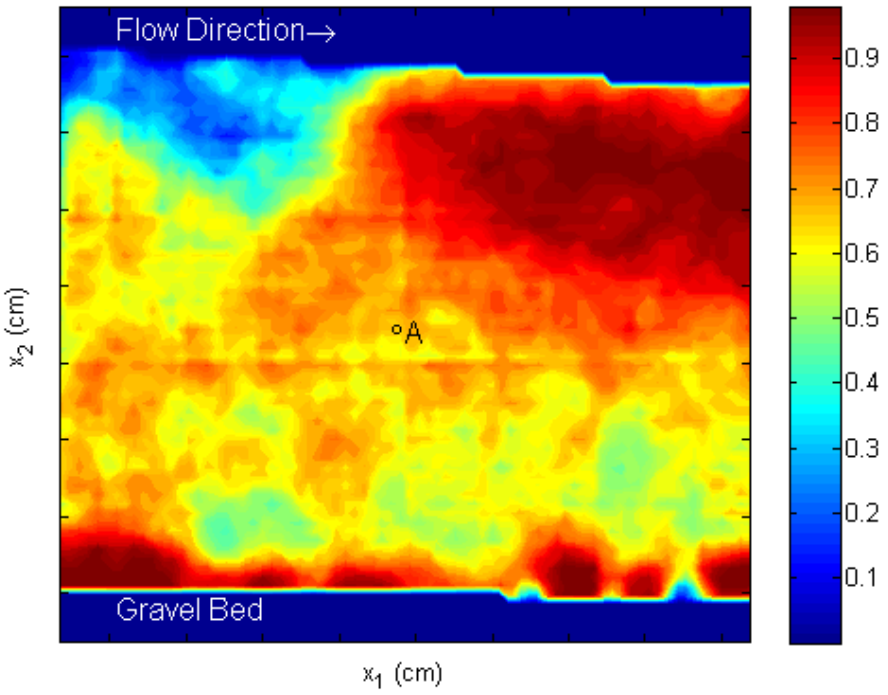

Figure 28. Test 1 Probability of Flow Reversal

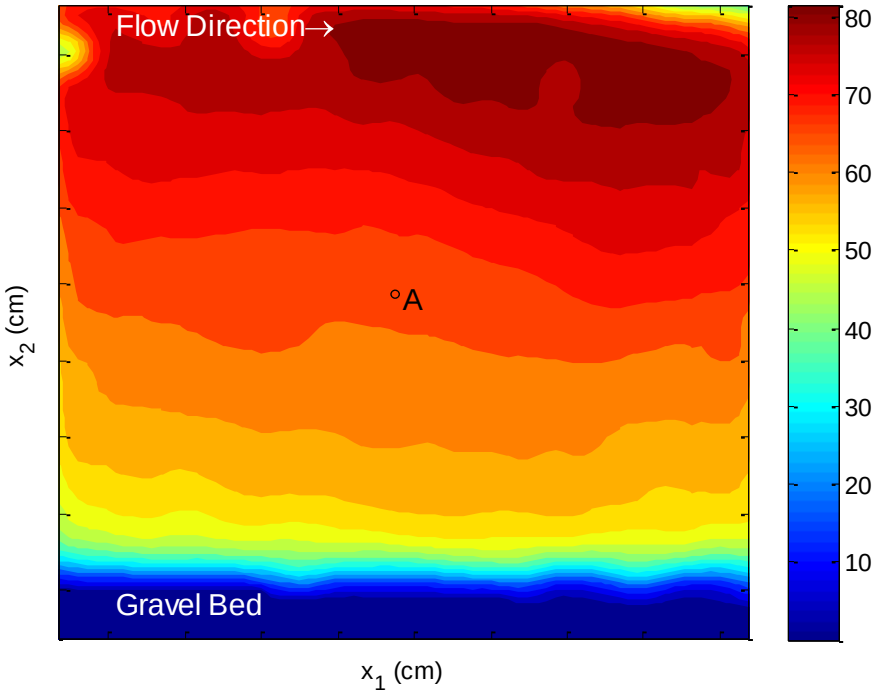

Figure 29. Test 2 Average Velocity Magnitude (cm/s)

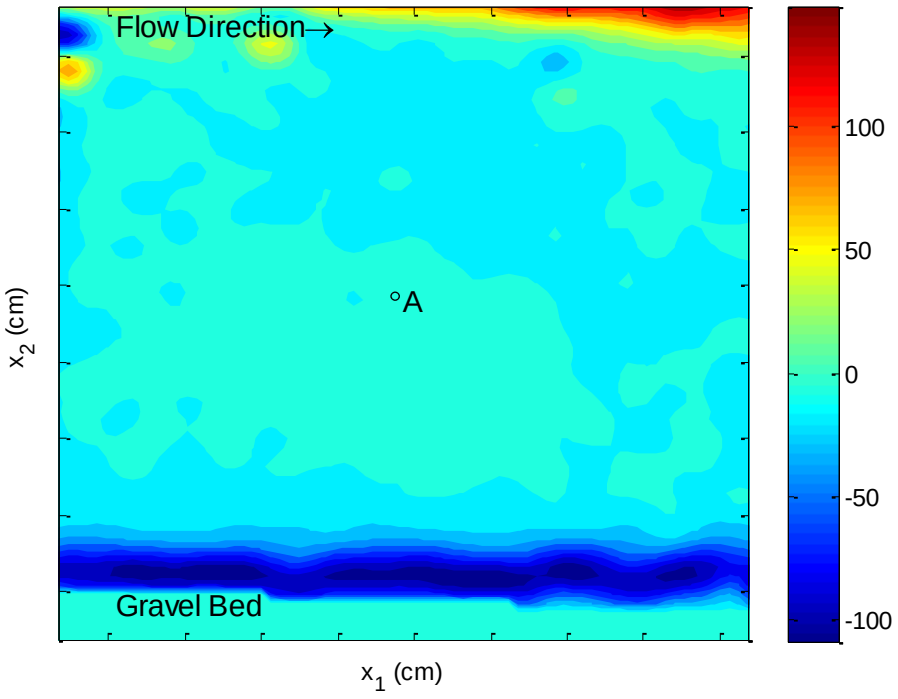

Figure 30. Test 2 Average Vorticity Magnitude (1/s)

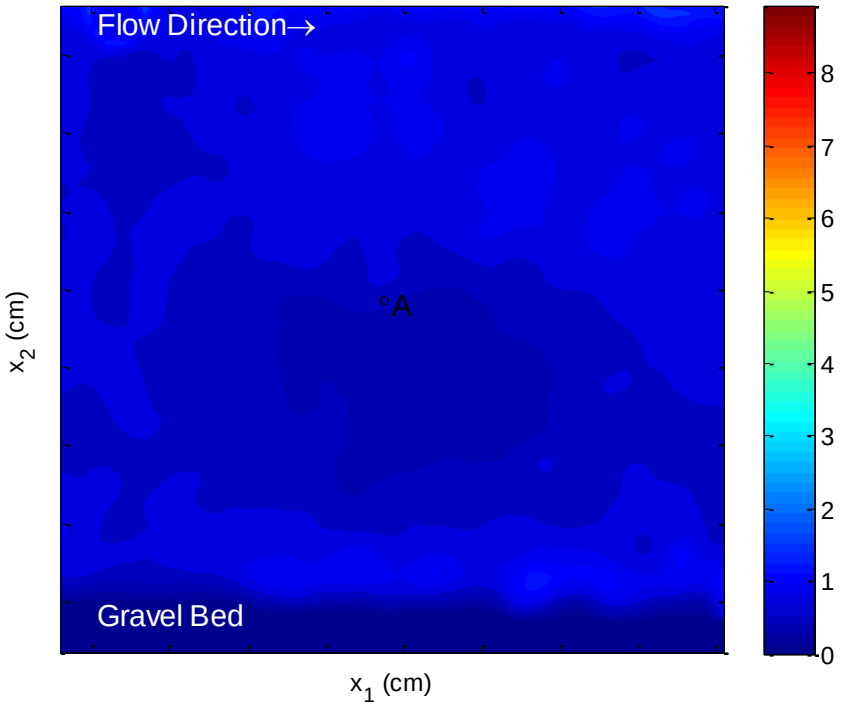

Figure 31. Test 2 Average Root-Mean-Square Velocity Fluctuations

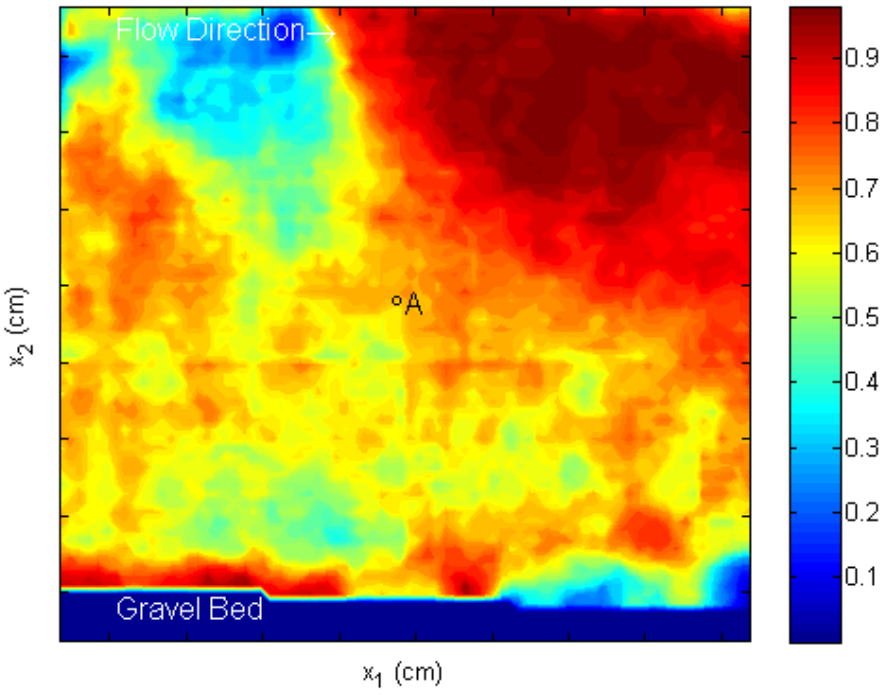

Figure 32. Test 2 Probability of Flow Reversal

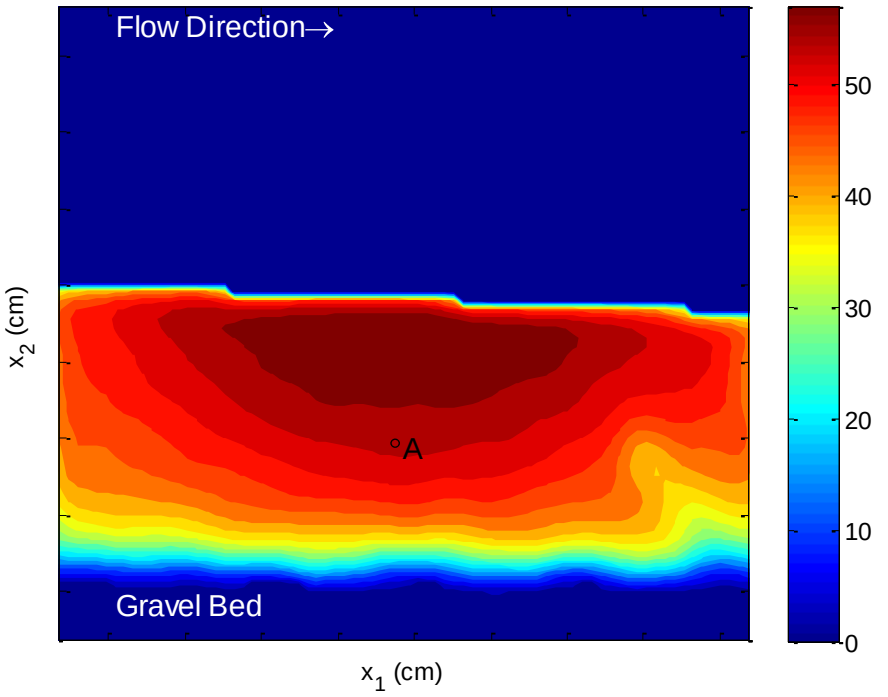

Figure 33. Test 3 Average Velocity Magnitude (cm/s)

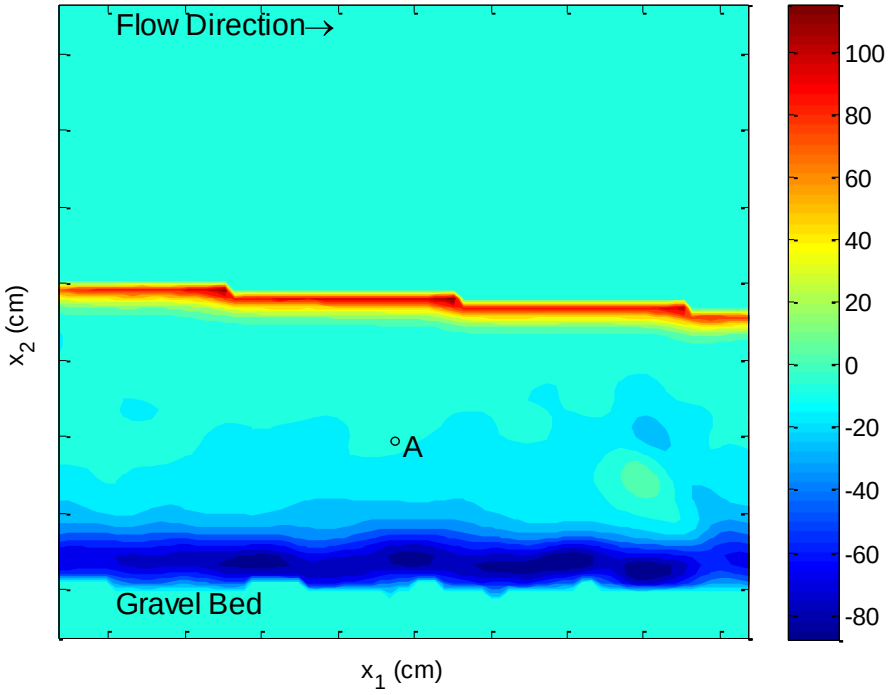

Figure 34. Test 3 Average Vorticity Magnitude (1/s)

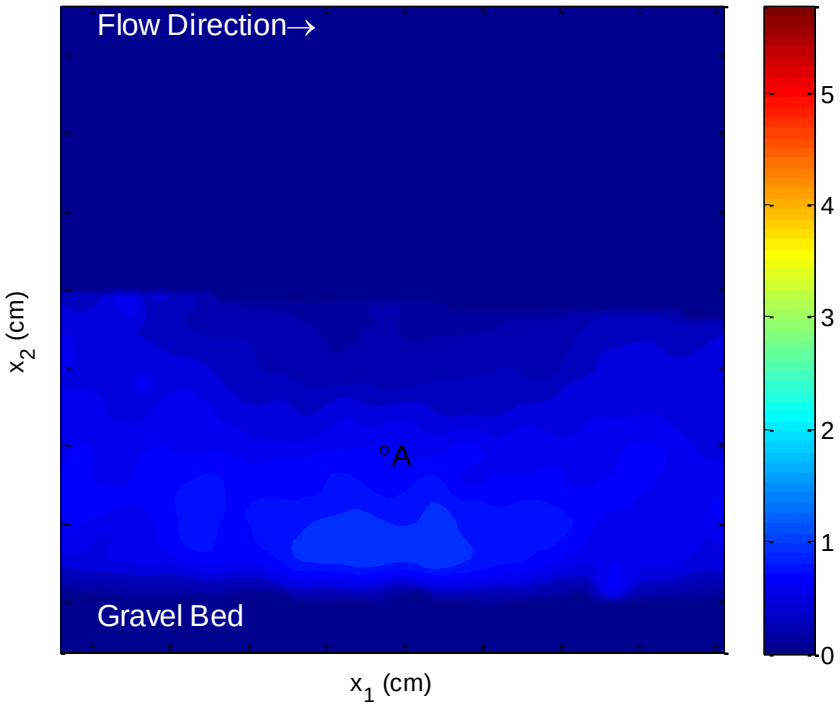

Figure 35. Test 3 Average Root-Mean-Square Velocity Fluctuations

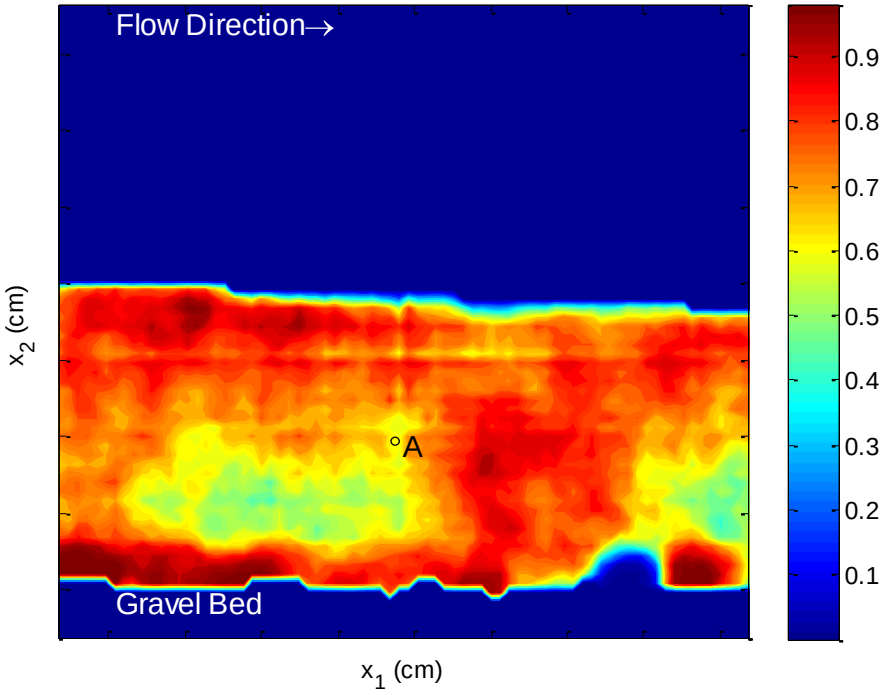

Figure 36. Test 3 Probability of Flow Reversal

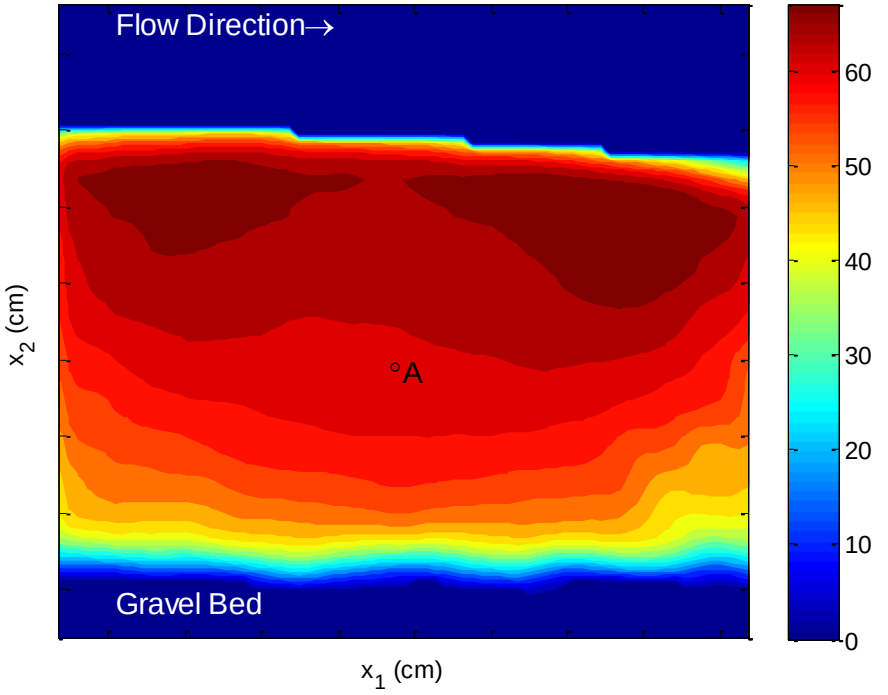

Figure 37. Test 4 Average Velocity Magnitude (cm/s)

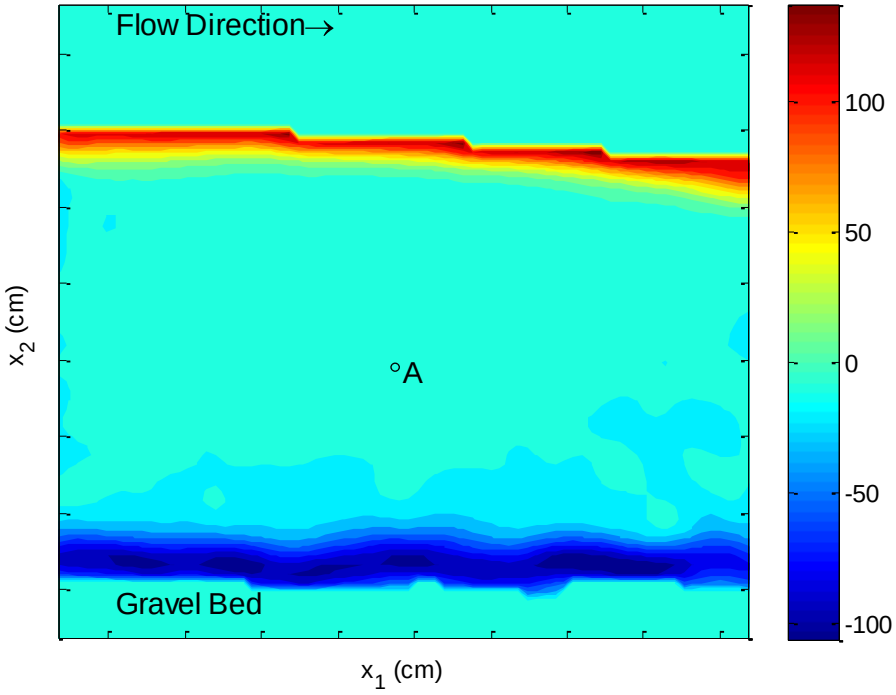

Figure 38. Test 4 Test 1 Average Vorticity Magnitude (1/s)

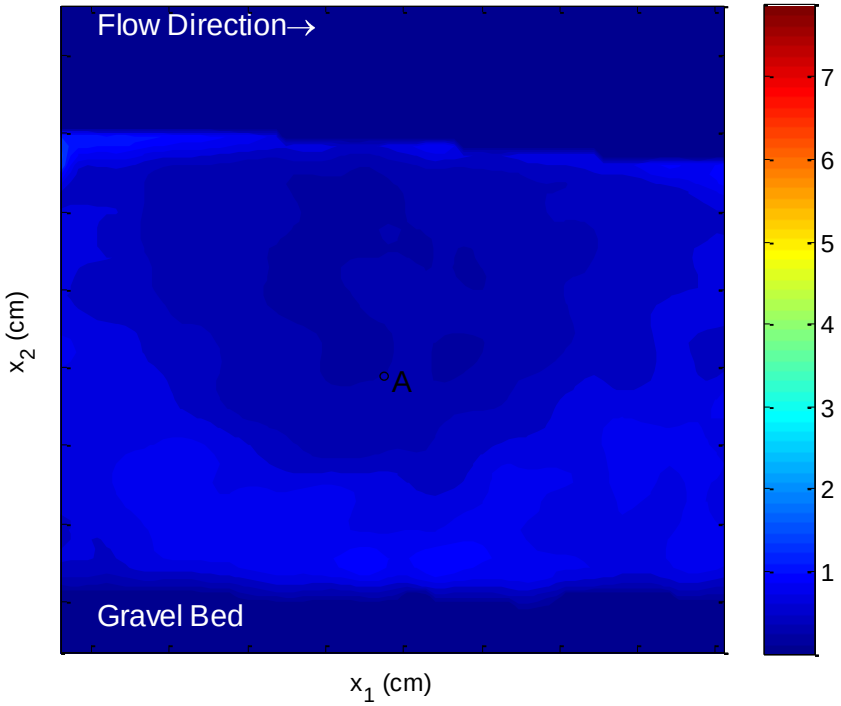

Figure 39. Test 4 Average Root-Mean-Square Velocity Fluctuations

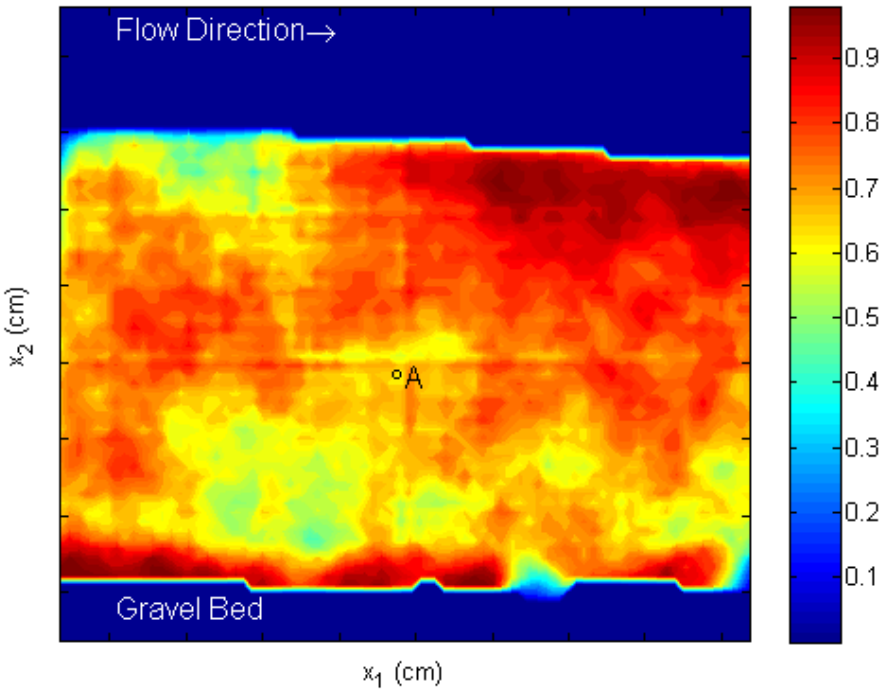

Figure 40. Test 4 Probability of Flow Reversal

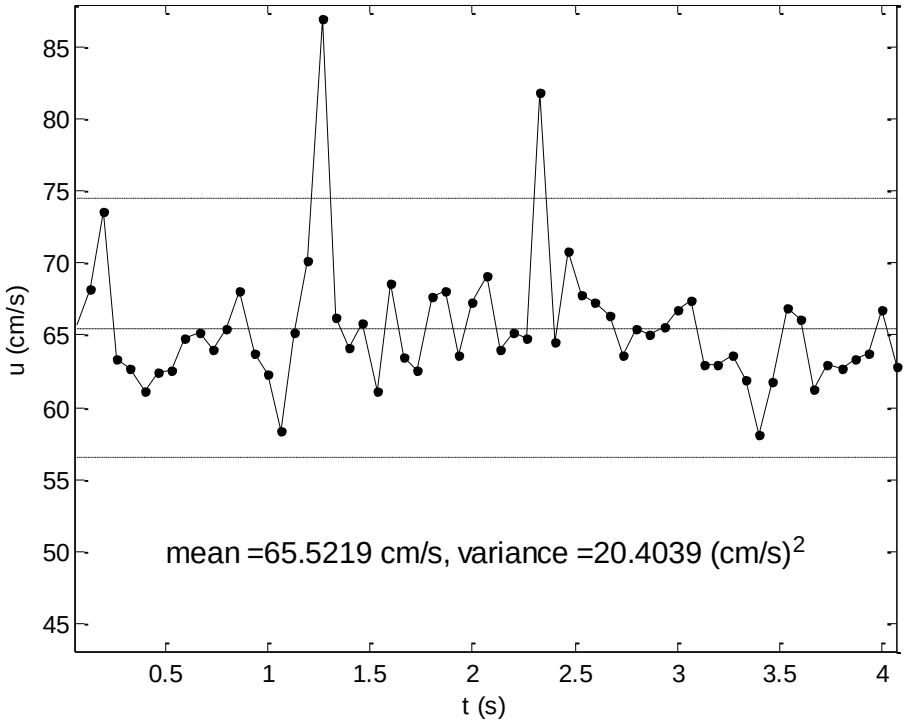

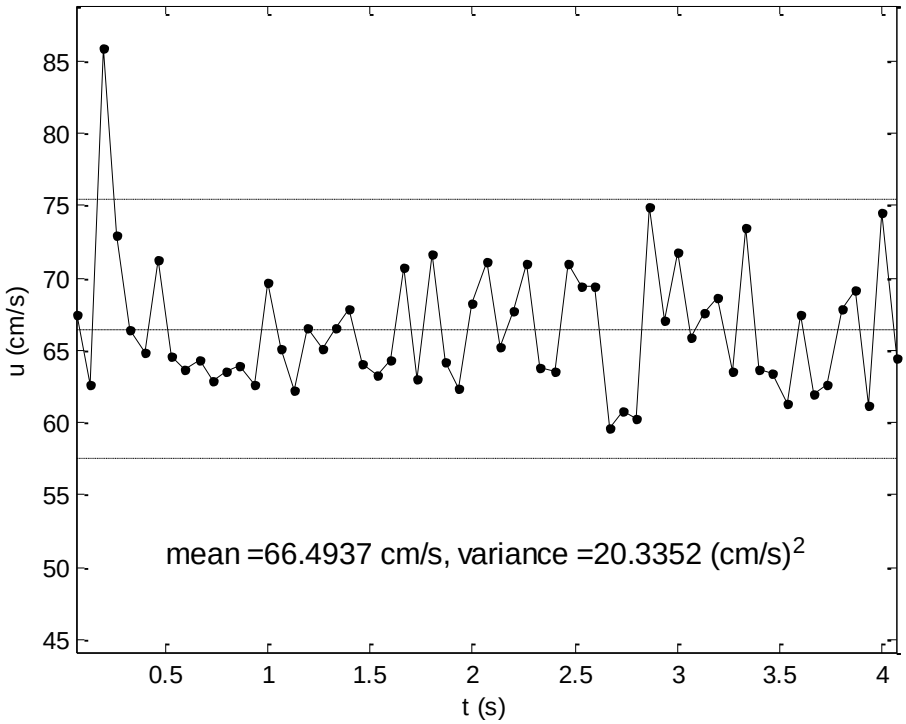

Figure 41. Time variation of streamwise velocity component at position A denoted by the circle plotted in Figures 25 through 40 (this figure contains four plots representing Tests 1-4, ordered top to bottom, respectively)

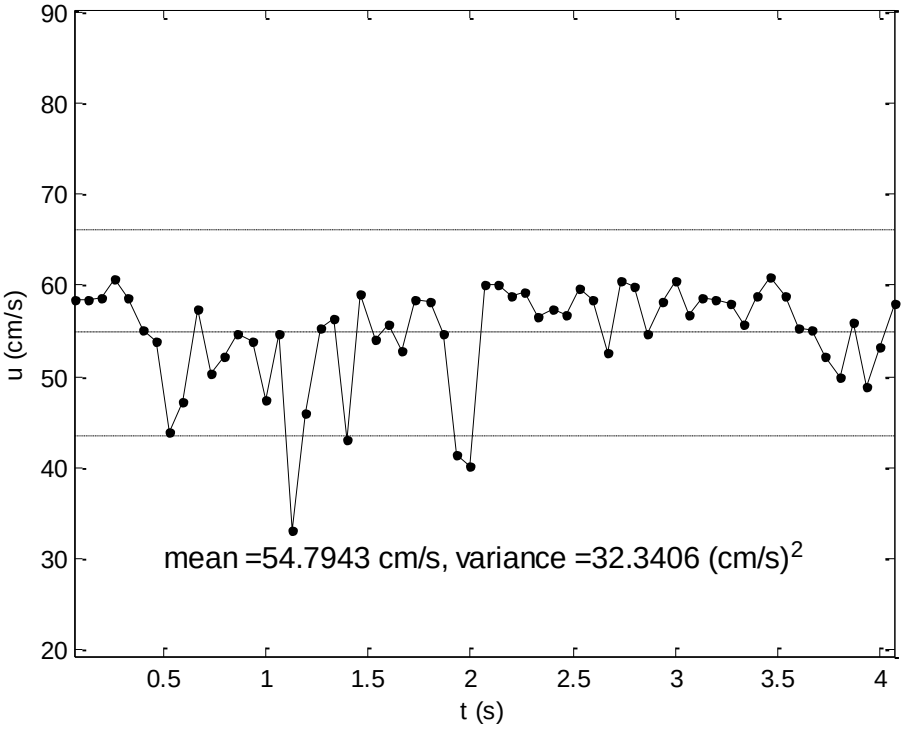

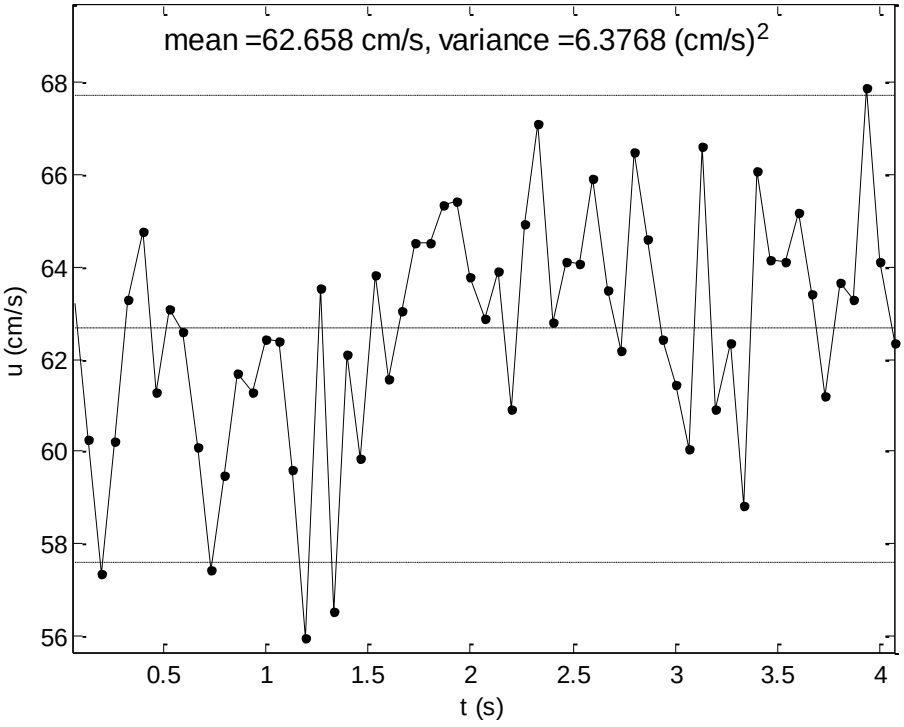

Figure 41. continued

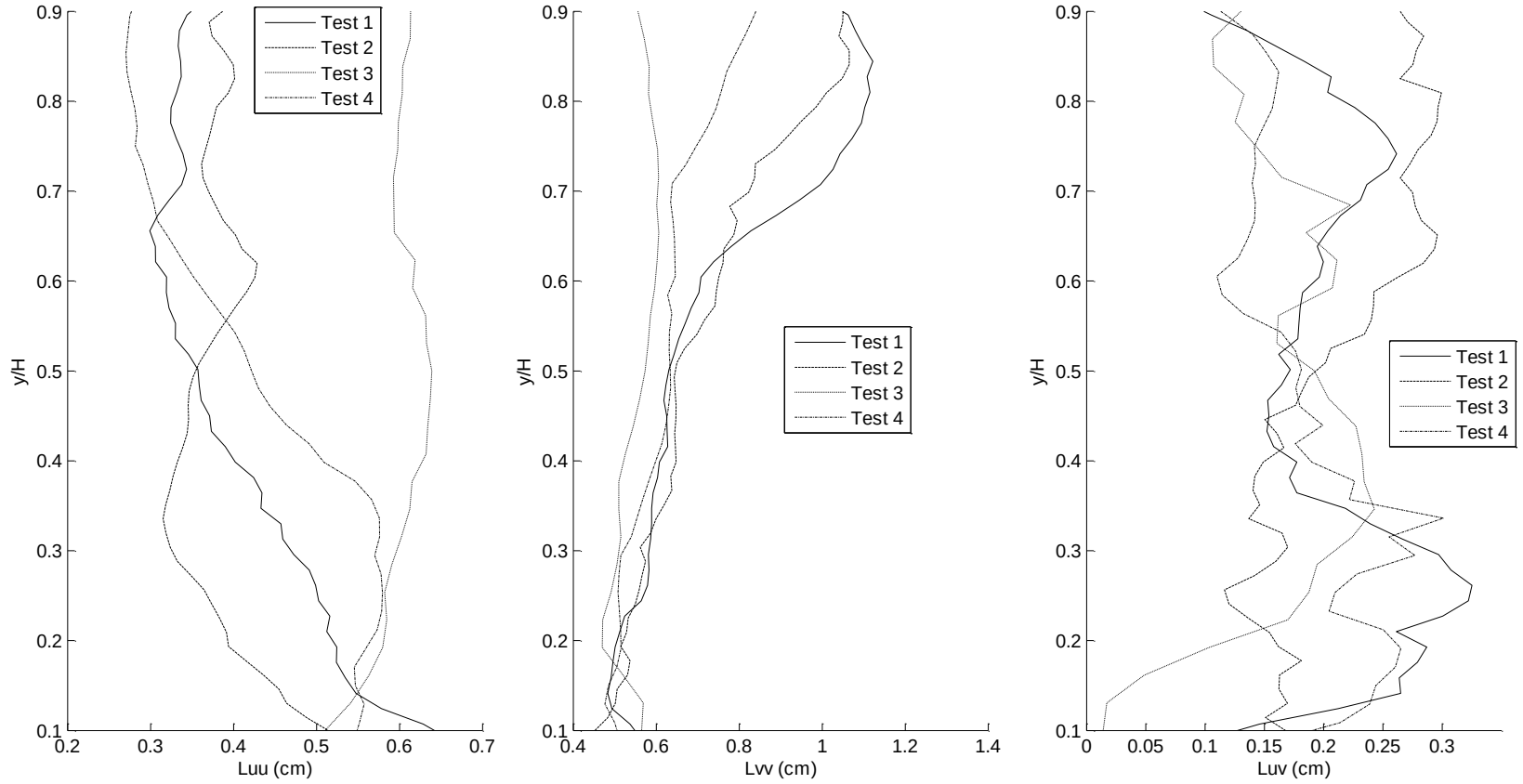

Figure 42. Dimensionless depth vs. streamwise averaged spatial correlation length scales

The main findings from the results plotted in Figure 25 through Figure 42 are that the spatial velocity fields are rich with statistical structure, including the same type of autocorrelation length scales of the vertical fluctuations and streamwise fluctuations that appeared in the time-series of the ADV data.

The average velocity magnitude (e.g. Figure 25) field has a similar structure for these tests characterized by undular spatial patterns near the bed attributed to the grain roughness elements. From the surface of the bed upwards the velocity magnitude increases quickly to reach maximum values closer to the free surface. Velocity gradients near the surface of the gravel bed are higher than in the central region of the flow, indicative of a viscous shear flow. The velocity magnitude is more spread out with lower gradients in the central or core region. Additional gradients in the velocity magnitude are seen near the free surface for each test and this may indicate secondary currents and/or interactions of vortices with the water surface. A spatial pattern which indicates the possible presence of flow separation or vortex shedding processes is identifiable in the average velocity of the lowest depth test shown in Figure 33 and this process appears to be present in each of the other tests. This may indicate that a particularly large, sharp or otherwise preferred particle dominates the turbulence in this region; however, careful investigation of the photographs of these particles (see Figure 17) did not reveal any unusual particles in this region of assumed randomly distributed particles.

The average vorticity plots, (e.g. Figure 26) show that the flow does have vorticity however it appears to be concentrated at the wall, forming an inner layer, and is diffusing upwards into the outer layer. The thin red layer near the free surface in each test shows that the vorticity is also concentrated in this region and is perhaps strongly influenced by surface tension. The average vorticity is approximately zero in the core region, meaning that there is no preferred direction of eddy motions on average.

The Reynolds stress plots (e.g. Figure 27) show that the fluid stresses are distributed with large-scale structure that contain areas or pockets of higher magnitude stresses. The patterns in the stress plots are very similar to the patterns of the velocity magnitude pots.

The plots of probability of flow reversal (e.g. Figure 28) are themselves rich with spatial structure. These plots indicate that for all test conditions areas of flow reversal are arranged into patterns connected to the wall. A striking example is shown in Figure 36, which may be interpreted as evidence of a stable turbulence bursting event which occurs over the duration of the PIV test. The blue regions in these plots are areas that tend to always be flowing in the streamwise direction regardless of the turbulence, as would occur if a large vortex ring is attached to the wall at this location.

One may conclude from the time-series plots shown in Figure 41 that at least one statistical large-eddy structure has passed into the field of view because in all tests at least one point in the time-series at the channel half-height has variance at least greater than the standard deviation, i.e. root-mean-square turbulence intensity.

In the spatial versions of the calculated correlation scales (see Figure 42) the eddy sizes appear to collapse into a narrow range below the dimensionless depth $y/H = 0.6$ for the PIV tests. The structure of the Lvv plots has a self-similarity for these tests; Lvv collapses linearly in the range $y/H < 0.6$ and then varies non-linearly to the free surface where they are ordered in terms of magnitude following increasing flow depth. This finding is an important supporting argument for the hypothesis that a structural model

may organize the vertical velocity fluctuations. The length scales due to cross-correlations appear to collapse at the channel half-height, indicating that only a narrow region may exist in which turbulence may be considered isotropic, near the location of our imaginary ADV probe, A in each test. These spatial autocorrelation length scales are indicative of very thin-cored turbulent eddies associated with hairpin-type vortex structures.

4.4 Spatial Decomposition Methods and Results

A spatial decomposition method is a filtering technique that removes a portion of the variance of the velocity vector field, which otherwise may have too much "noise" caused by the superposition of many sizes of vortices moving at different speeds for us to identify large coherent structures using a visual determination. The need for some sort of filtering technique becomes obvious after examining the instantaneous vector fields.

Four spatial decomposition methods were used as tools for visualizing coherent structures, resulting in the filtered vector field plots shown in Figure 44 through Figure 50: (1) Galilean transformation, (2) Reynolds decomposition, (3) homogeneous large-eddy simulation decomposition, and (4) inhomogeneous large-eddy simulation decomposition known as proper orthogonal decomposition. Adrian et al. (2000) summarizes the use of these methods for previous studies of turbulent boundary layers. Each method provides useful information about the variations in the velocity field. Next is a description of how each of these filtering techniques was used in this application.

4.4.1. Galilean Transformation

Galilean transformation is simplest decomposition method and expresses the idea that an invariant property of the flow, such as vorticity, does not depend on the velocity of the observer. Therefore if a vortex core exists somewhere in the field of view, the removal of a fixed convection velocity from the instantaneous vector field will reveal its core, resulting in nearly elliptical or spiral patterns in the filtered velocity vector field. The Galilean transformation is mathematically represented by the decomposition of the unfiltered velocity field into the two components:

$$\mathbf{u} = \mathbf{U}_c + \mathbf{u}_c \tag{7}$$

where $\mathbf{u}$ is the instantaneous total velocity (u_1, u_2), $\mathbf{U}_c$ is the fixed convection velocity (U_{c1}, U_{c2}) and $\mathbf{u}_c$ is the vortex convection velocity ($\mathbf{u}$ - $\mathbf{U}_c$). For each experiment, $\mathbf{U}_c$ was scaled by the ensemble-averaged, maximum free-stream velocity $\mathbf{U}_\infty$ such that

$$\mathbf{U}_c = \theta \mathbf{U}_\infty, \ \theta \in [0, 2] \tag{8}$$

The Galilean transformation method has been used in previous flow visualization studies of turbulent coherent structures and it is known to be well suited for visualization of local velocity patterns induced by eddies; however, a range of θ values must be used to visualize all of the different eddy structures moving at different convection velocities (Natrajan and Christensen 2006). Setting $\theta = 0$ returns the unfiltered instantaneous velocity field. Fields produced by iterated values of θ shown in (8) were tried and values in the range 0.7 to 0.8 were best for visualizing vortex cores. In Figure 45, $\theta = 0.7$, the region of high velocity near the surface (right, top) is moving upward with inclination angle approximately 30° relative to the bed and marks the downstream boundary of a thick region of knotted, thin-cored vortex tubes. Here the term "knot" is used as a general descriptive term and provide

a more rigorous discussion of knots in terms topology and the mathematics of knot and braid theory later in this thesis.

The benefit of the Galilean transformation filter technique is that it can be used to identify coherent vortex structures for these experiments. The problem is that it requires a wide range of convection velocities to find these structures in a given velocity field, thus it is not possibly to clearly identify how these structures are connected. It is evident from the results of this technique that the velocity gradients are very high near the bed and near the free-surface. A single convection velocity is not adequate to filter the entire flow depth in order to see some very slender vortex structure that may have different topology than a spiral or ellipse, i.e. the vectors stretch and overlap in regions near the free-surface and at the wall, making it difficult to clearly identify coherent structures in these regions and other regions simultaneously and how they are connected.

4.4.2. Reynolds Decomposition

Decomposition of the instantaneous velocity into the mean and fluctuations about the mean is the standard method for analyzing turbulent velocity fields (Adrian et al. 2000). The Reynolds decomposition of PIV data

$$\mathbf{u} = \mathbf{U} + \tilde{\mathbf{u}} \tag{9}$$

separates the total instantaneous velocity $\mathbf{u}$ into an expected value $\mathbf{U}$ and the fluctuations relative to the expected value representing turbulence $\tilde{\mathbf{u}}$. The time average was used for $\mathbf{U}$ and has infinite scales in the averaging directions. The fluctuations have finite spatial and temporal fluctuation scales in x_1 and x_2 (Adrian et al. 2000). The data are assumed to be homogeneous in the streamwise direction but not in the vertical; therefore $\mathbf{U}$ was defined as the ensemble mean vertical velocity profile calculated by averaging the rows of the velocity tensor for each experiment. Vortex cores were subsequently visualized and eddies educed in vector field plots of $\tilde{\mathbf{u}}$ (see Figure 46). According to Adrian et al. (2000), one of the strengths of this decomposition method is that it does a fair job of revealing small scale vortices; however, a weakness is that it removes large-scale features "intimately associated with the mean flow".

The Reynolds decomposition results, e.g. Figure 46, reveal coherent structures similar to the Galilean transformation shown in the previous figure in the region of high velocity (top, right), and also identifies a thick turbulent region with finer texture filled with vortex cores moving nearly at the mean velocity distribution.

4.4.3. Homogeneous Large-eddy Simulation Decomposition

Large-eddy simulation (LES) decomposition is a spatial filtering method that separates the total velocity into the sum of the large-scale and small-scale fluctuations in space and time. This method differs from the Reynolds decomposition because not only infinite spatial and or temporal scales are isolated from the total instantaneous fields and it is a more general approach because it separates the field into separate groups that represent different spatial scales. The LES decomposition is useful because it removes the translation due to the larger-scale eddies (Adrian et al. 2000). The LES decomposition separates the total instantaneous velocity field into two components:

$$\mathbf{u} = \mathbf{u}_{<} + \mathbf{u}_{>} \tag{10}$$

where $\mathbf{u}_<$ is the large-scale field and $\mathbf{u}_>$ is the remaining small-scale field. The large-scale field is based on a spatial averaging technique:

$$\mathbf{u}_<(\mathbf{x},t) \equiv \frac{1}{V_\Omega}\int_\Omega u(\xi,t)g(x|\xi)d\xi \tag{11}$$

where V_Ω is the area of the flow domain and g is a spatial-averaging filter kernel. A homogeneous Gaussian filtering kernel was used to compute the large-scale field in this LES decomposition, defined by

$$G(\xi) = \frac{1}{\sigma\sqrt{2\pi}} e^{-\frac{\xi^2}{2\sigma^2}}, \tag{12}$$

where σ is the standard deviation. The effect of a Gaussian filter kernel is to smooth the data by removing the influence of the small-scale vortices, which is equivalent to finding the value of σ that allows visualization of the small scale eddies using the definition of a vortex core. Several values of σ were evaluated. The large-scale filtered field, plotted in Figure 47, was subtracted from the total instantaneous velocity field to visualize the small scale vortices, plotted in Figure 48. The result of the LES decomposition is to provide a large-scale filter similar in characteristics to the instantaneous vector field, e.g. the high-speed region, although with subtler texture. The small-scale filtered field (Figure 48) is rich with turbulent motions that could be due to vortices, including the region of high-velocity, though relatively few eddies in this region have nearly circular cores. Instead, the small-scale field appears to be better described as a knotted or linked grouping of long, thin-cored, meandering vortex tubes. It is easy to identify hairpin-type vortex elements using this method. These hairpin-type elements generally have "legs" inclined ~45-degrees relative to the wall and "heads" which form an arc, bridging the legs from above.

4.4.4. Inhomogeneous LES – Proper Orthogonal Decomposition

Since vortices may change size and shape as they move away from the bed, an improvement of the LES decomposition may be to replace the kernel G in equation (12) with an inhomogeneous filtering kernel, providing an improved visualization of the vortices away from the bed. The proper orthogonal decomposition (POD) was used to compute an inhomogeneous filtering kernel. This is also scale decomposition and is very similar to LES. POD is known in other fields of research by various names including the single value decomposition, the principal components analysis and the Karhunen-Loéve decomposition (Chatterjee 2000). POD is a mathematical decomposition applicable in the field of turbulence research (Lumley 1985; Liu *et al.* 1994; Adrian, Christensen *et al.* 2000; Liu *et al.* 2001).

In the POD filtering method, the large-scale field is based on spatial averaging as:

$$\mathbf{u}_<(\mathbf{x},t) = \int_M u(\mathbf{x}',t)h(\mathbf{x},\mathbf{x}')d\mathbf{x}' \tag{13}$$

where M is the flow domain and *h* is the correlation, or filter kernel. The POD procedure finds the most correlated features of the flow dynamics and has the benefit of being unbiased with respect to the input of the experimentalist (Chatterjee 2000). These highly correlated features are the eigenvalues (POD modes) of the integral equation (Holmes *et al.* 1998)

$$\int R(x_1, x_1', x_2, x_2')\phi(x_1', x_2')dx_1'dx_2' = \lambda\phi(x_1, x_2)\,, \tag{14}$$

involving the average two-point correlation tensor:

$$R(x_1, x_1', x_2, x_2') = \left\langle \mathbf{u}(x_1, x_2)\mathbf{u}(x_1', x_2')^* \right\rangle. \tag{15}$$

In (15), $\langle\ \rangle$ represents spatial averaging and * represents complex conjugate. Almost every member of the ensemble can be reconstructed using the entire set of POD modes by the following equation:

$$u^k(x_1, x_2) = \sum_{n=1}^{N} a_n^k \phi^n(x_1, x_2)\,, \tag{16}$$

where the uncorrelated POD coefficients (*a*'s) are the square roots of the eigenvalues (λ's). Eigenvalues are arranged in descending order, then a low rank approximation of (16) can be found by summing not over the entire *N* eigenvalues, but from n=1 to n=*K*, where *K* represents a cutoff number (Liberzon *et al.* 2006).

The method of snapshots (Sirovich 1987) was used to approximate the covariance matrix for each ensemble. Each (k^{th}) snapshot was written as a vector as:

$$u^k = \begin{bmatrix} u_1 \\ \vdots \\ u_m \end{bmatrix}, \tag{17}$$

where $u_m = [u_m, v_m]^T$ and the superscript represents transposition (Liberzon *et al.* 2006). The symmetric covariance matrix was constructed from the ensemble (*k*=1,...,*N*) as:

$$C = \left\langle \mathbf{u} - \langle \mathbf{u} \rangle^{T} \quad \mathbf{u} - \langle \mathbf{u} \rangle \right\rangle \tag{18}$$

The eigenvalues (λ) and eigenfunctions (φ) satisfy

$$C\varphi = \lambda\varphi\,, \tag{19}$$

and the POD modes were found by projection on the original velocity fields as

$$\phi^{(n)} = \sum_{j=1}^{N} \varphi_j^{(n)} \mathbf{u}^j\,. \tag{20}$$

The large scale filtered fields were then computed by

$$\mathbf{u}_{<}(x_1, x_2) = \sum_{n=1}^{K} \lambda^{(n)} \phi^{(n)}(x_1, x_2)\,, \tag{21}$$

and the remaining small-scale field was obtained using the LES decomposition shown in equation (10). Vectorial decomposition methods were implemented with MATLAB on a desktop PC with a 3 GHz Intel® Pentium® 4 CPU and 1 GB RAM.

The selection of the cutoff number *K* has been discussed by others (Adrian, Christensen *et al.* 2000; Liu *et al.* 2001; Liberzon *et al.* 2006) Selection of the appropriate *K*

was used following the number of modes that best allows visualization of the eddies, which is the same as finding a value that delimits the "characteristic eddies" in the flow field while maintaining a reasonable small truncation error for recovering the total kinetic energy of the actual turbulence intensities. 50% of turbulent kinetic energy was used as a threshold for filtering the "large" and "small" scale fields arbitrarily after assessing other thresholds and found that the large-scale structures were identified using this value in all test cases, as was the case in Liu *et al.* (2001). The distribution of the total turbulence kinetic energy recovered is plotted as a function of the POD modes $n \in [1...61]$ in Figure 43.

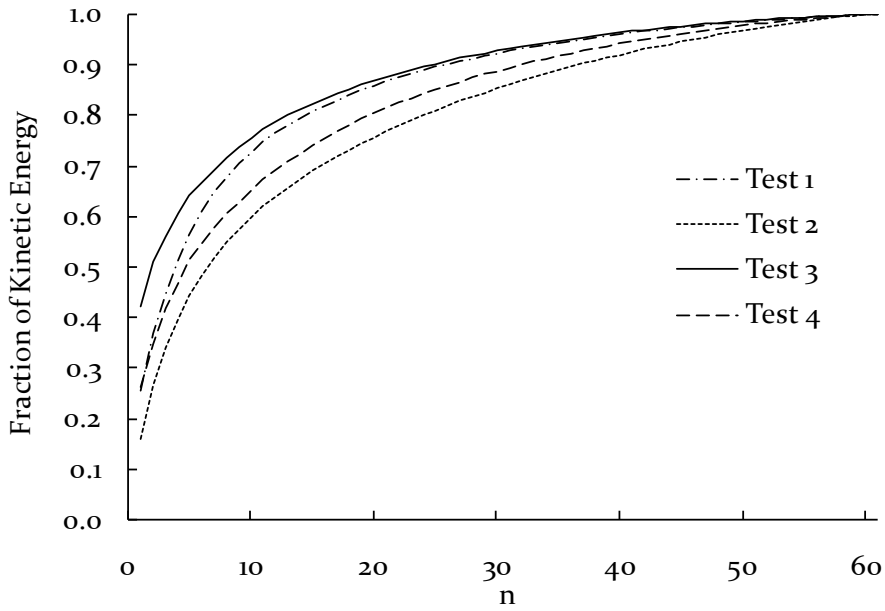

Figure 43. Turbulent kinetic energy vs. POD mode number

Figure 43 indicates that as the depth increases in the flume a higher number of POD modes are required to recover a given energy level. This indicates that the turbulence phenomena are more complex for higher flow depths. For these experiments the first ten POD modes capture at least 50% of the total turbulent kinetic energy of the ensembles. Each possible value of the cutoff number in the range $K \in [1...10]$ were tried and it was found that $K=[3...5]$ was sufficient to visualize the characteristic small- and large-scale coherent motions for this setup (CE FLUME). The use of higher K values tends to blur the large-scale phenomena by incorporating more of the faster moving fluctuations from smaller-scales, thus making it more difficult to identify coherent structures in the vector field or streamlines.

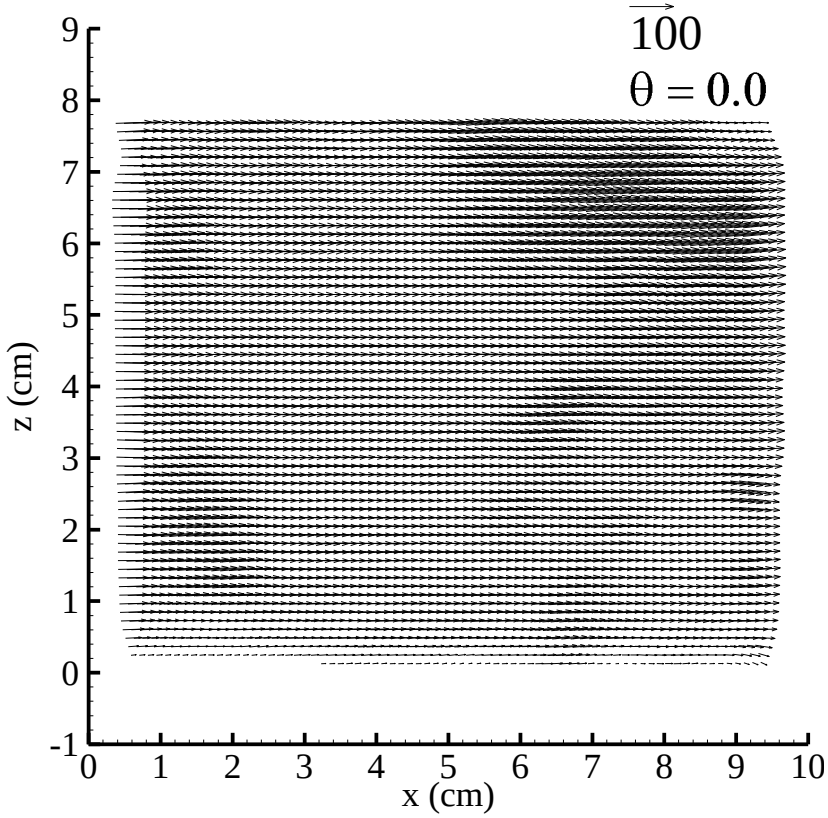

Figure 44. Instantaneous 2-D velocity vector field

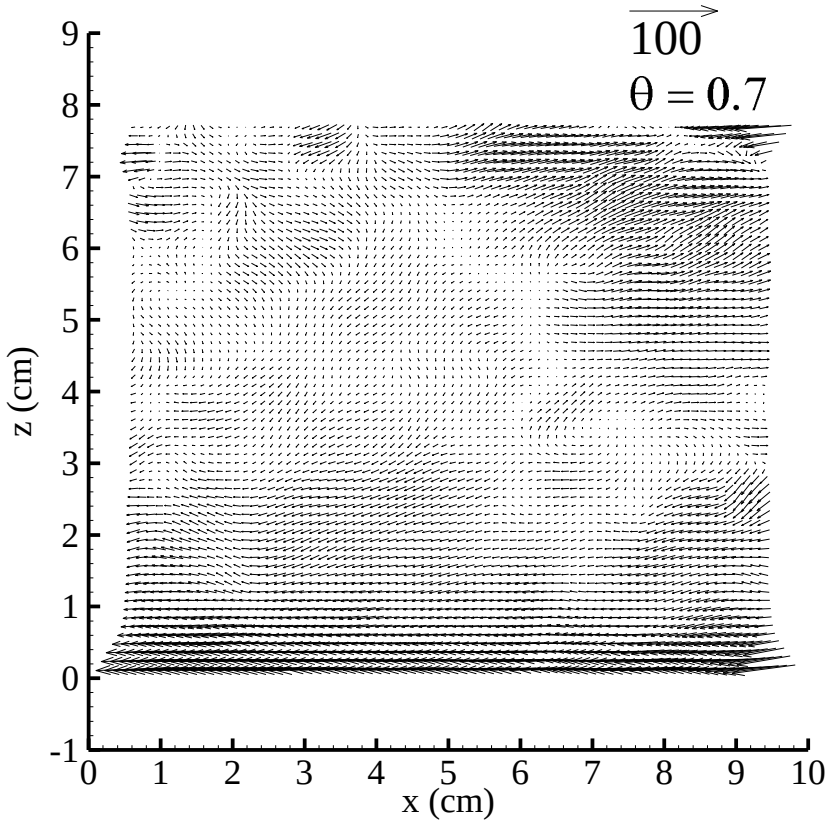

Figure 45. Galilean Transformation

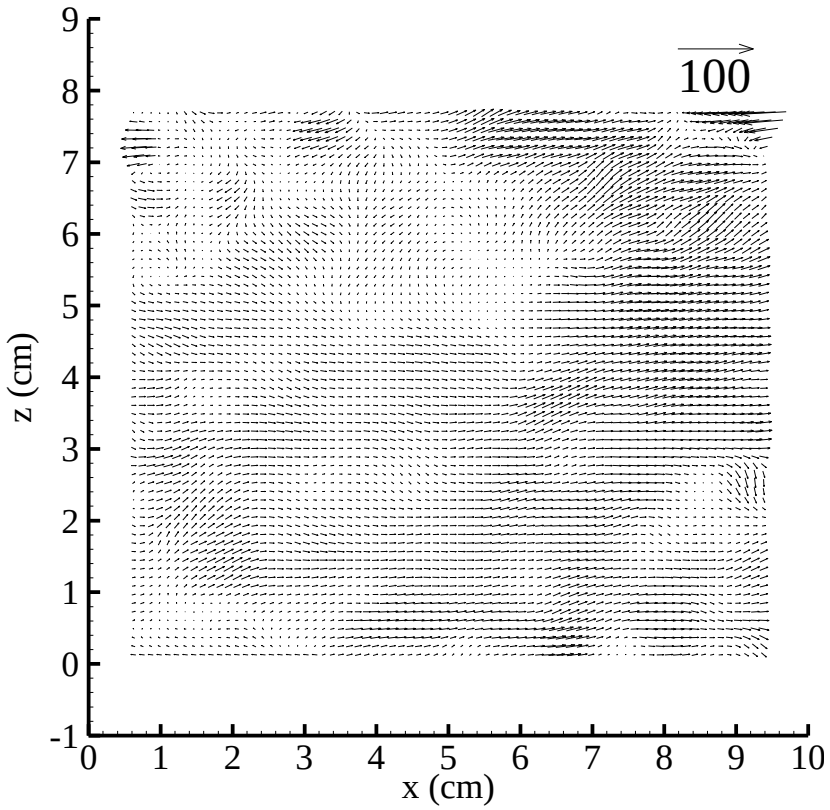

Figure 46. Reynolds Decomposition

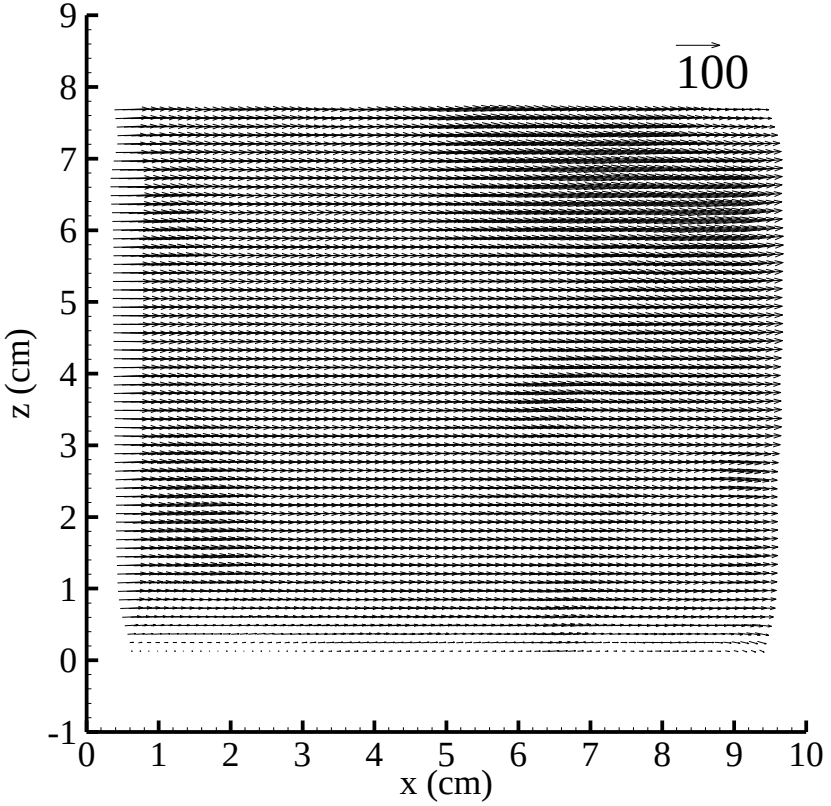

Figure 47. LES Large-Scale Filtered Field

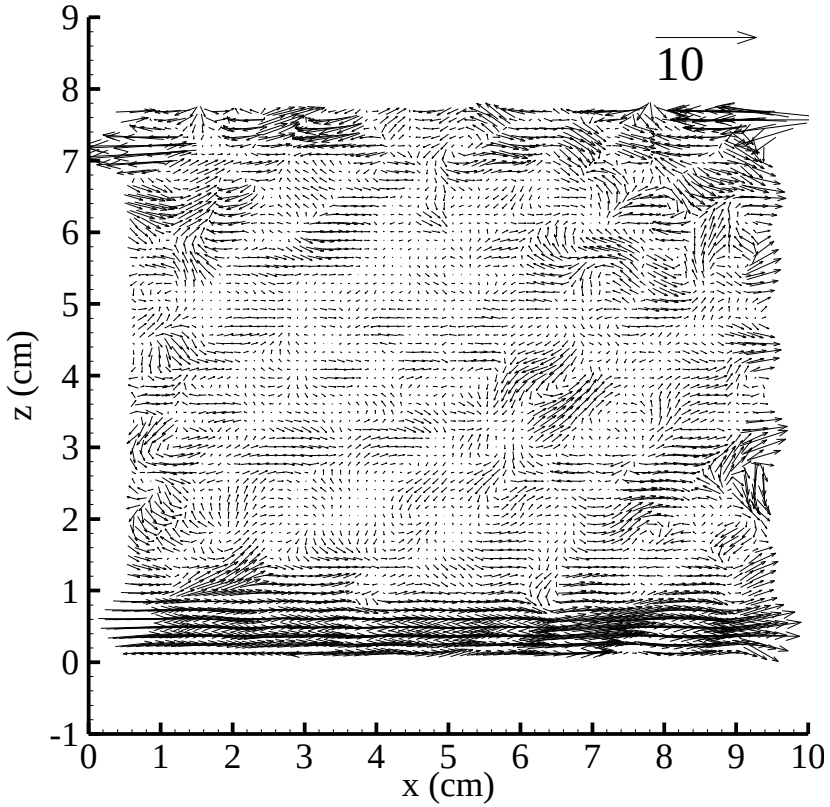

Figure 48. LES Small-Scale Filtered Field

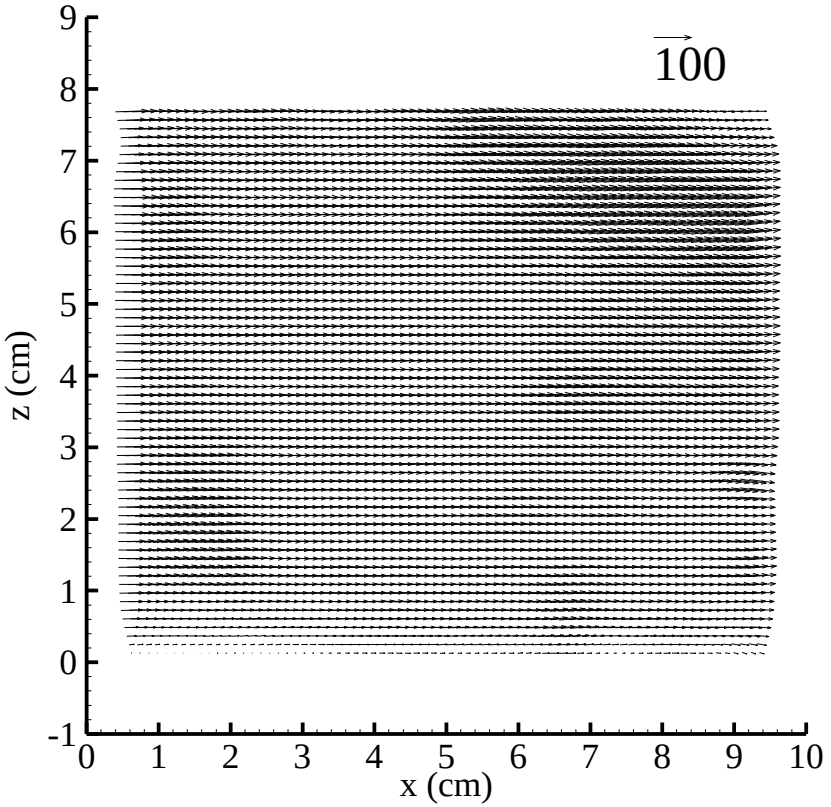

Figure 49. POD Large-Scale Filtered Field

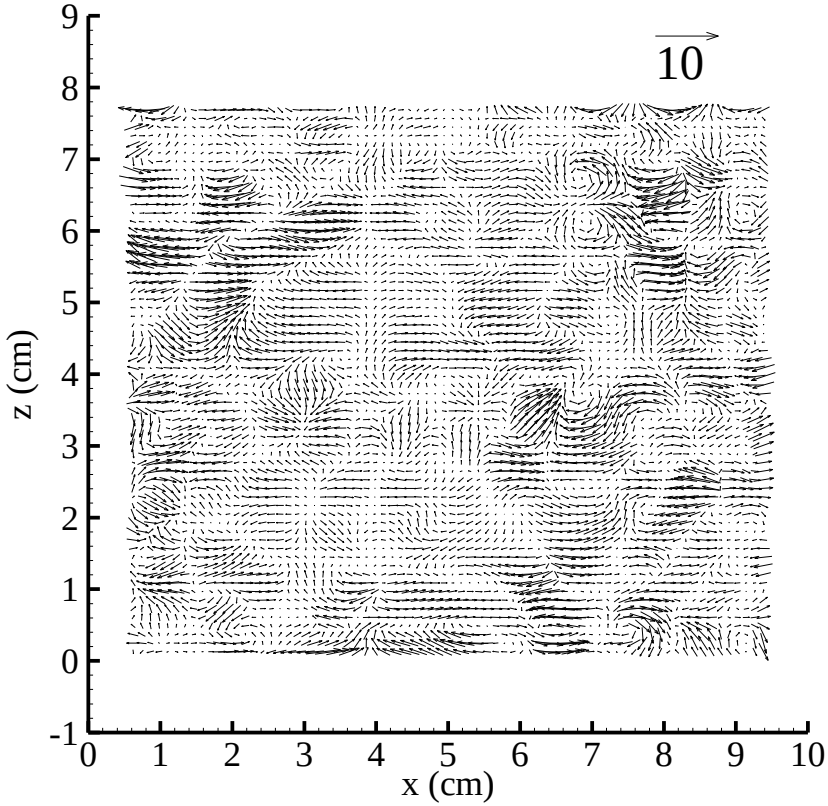

Figure 50. POD Small-Scale Filtered Field

In Figure 44 through Figure 50 the four spatial decomposition methods are compared by filtering the same random sample, Test 3 image-pair 15, to demonstrate the different types of visualization results. The POD appears to be the best method of the four presented above for visualizing both the large-scale and small-scale turbulent dynamics and coherent structures for these test conditions (CE FLUME). The POD method produced velocity fields in which small-scale eddies could be determined and measured in the majority of the field of view; whereas, the other methods were distorted near the boundaries or required multiple convection velocities. The large-scale POD filtered field shown in Figure 49 and is very similar to the LES large-scale filtered field shown in Figure 47. Both filtering techniques adequately recover the flow dynamics intimately related to the mean flow. The small-scale filtered fields are also similar; the small-scale POD filtered field shown in Figure 50 can be used to identify the same types of eddies as in the LES (Gaussian filter kernel) small-scale filtered field shown in Figure 48. The similarity is the preponderance of thin vortex tubes often having structural organization resembling knot patterns. The difference is that the observed small-scale field shows knot patterns which are continuous, i.e. less sheared, at the boundaries in the POD method and more blurred or sheared in the LES-Gaussian method. Any small-scale structure, say on the order of 1 to 2 cm in circular diameter, observed in these POD small-scale fields can also be educed by iterating through the convection velocity values in the Galilean transformation method and thus is equivalent in terms of usefulness for identifying vortex cores and other eddies.

4.5 Characterization of the Turbulent Flow Fields with Flow Visualization

The dominant forms of spatial structures observed in the decomposed velocity fields for these gravel-bed flow conditions are identified in this section. Example images of the characteristic structures including both the smaller scale turbulence and the larger-scale turbulence events that are common to all tests are provided in the following figures.

4.5.1. Thin-Cored Vortex Tubes

The most prominent feature of all the tests is the preponderance of thin vortex tubes near the bed which may be considered hairpin and other u-loop type vortices similar to those sketched in Figure 8 after the vortex packet model of Adrian, Meinhart et al. (2000); however, in our tests the alignment of the heads of these tubes appears oriented with the streamwise and spanwise directions instead of aligned into packets along the streamwise direction as shown in the vortex packet model. In these experiments the thin-cored vortex tubes tend to become arranged into patterns that resemble long, streamwise braids which sometimes have spatial structures resembling knots. These vortex tubes were generally accompanied by low-speed fluid regions that connect over much longer spatial distances than a single hairpin vortex structure. These arrangements of the vortex tubes are often accompanied by large, pulsating turbulent velocities into the region near the surface at the small-scales and also in the outer layer at the larger-scales.

Examples of similar arrangements of vortex tubes and Reynolds stress events, i.e. sweeps, are shown below in instantaneous spatial decompositions where the smaller-scale eddies are shown in the field to the left and the simultaneous larger-scale eddies are shown to the right in Figure 51.

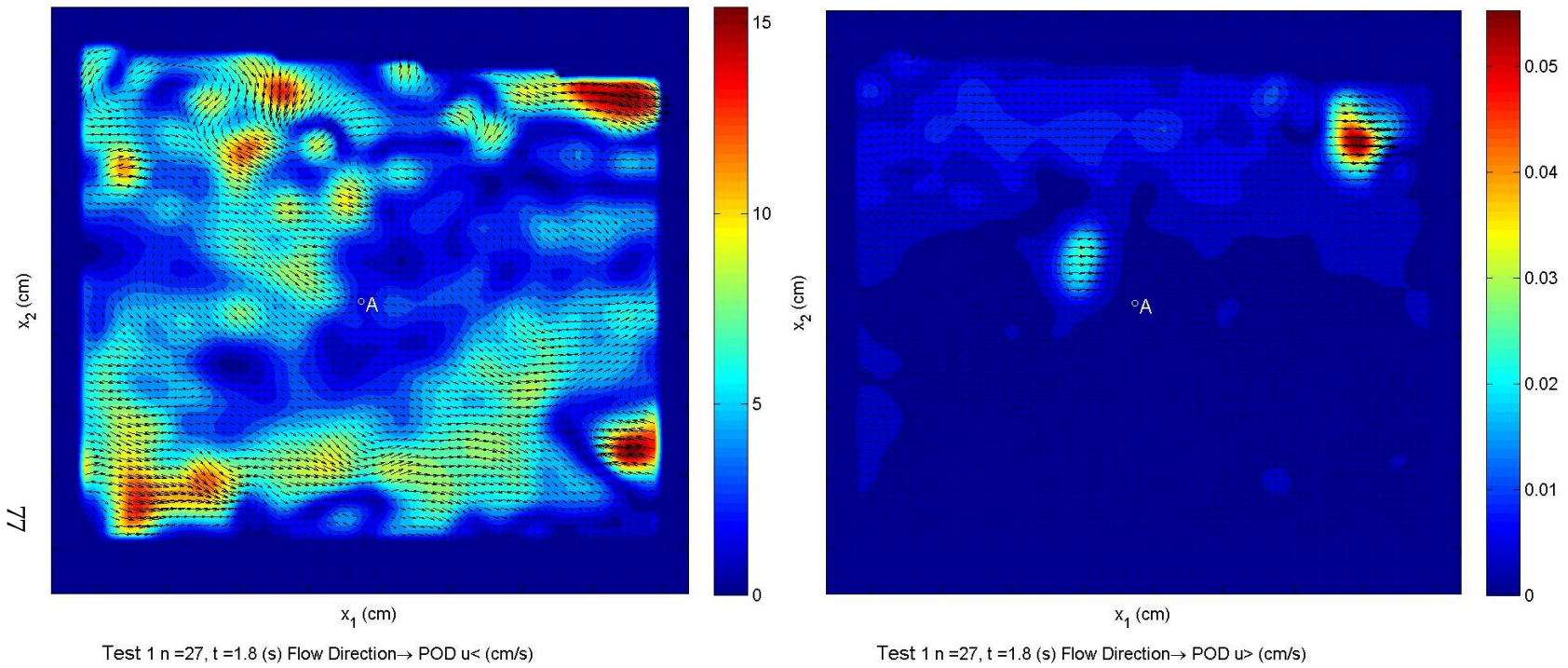

Figure 51. Characteristic sweeping motions accompanied by thin vortex tubes in the wall region

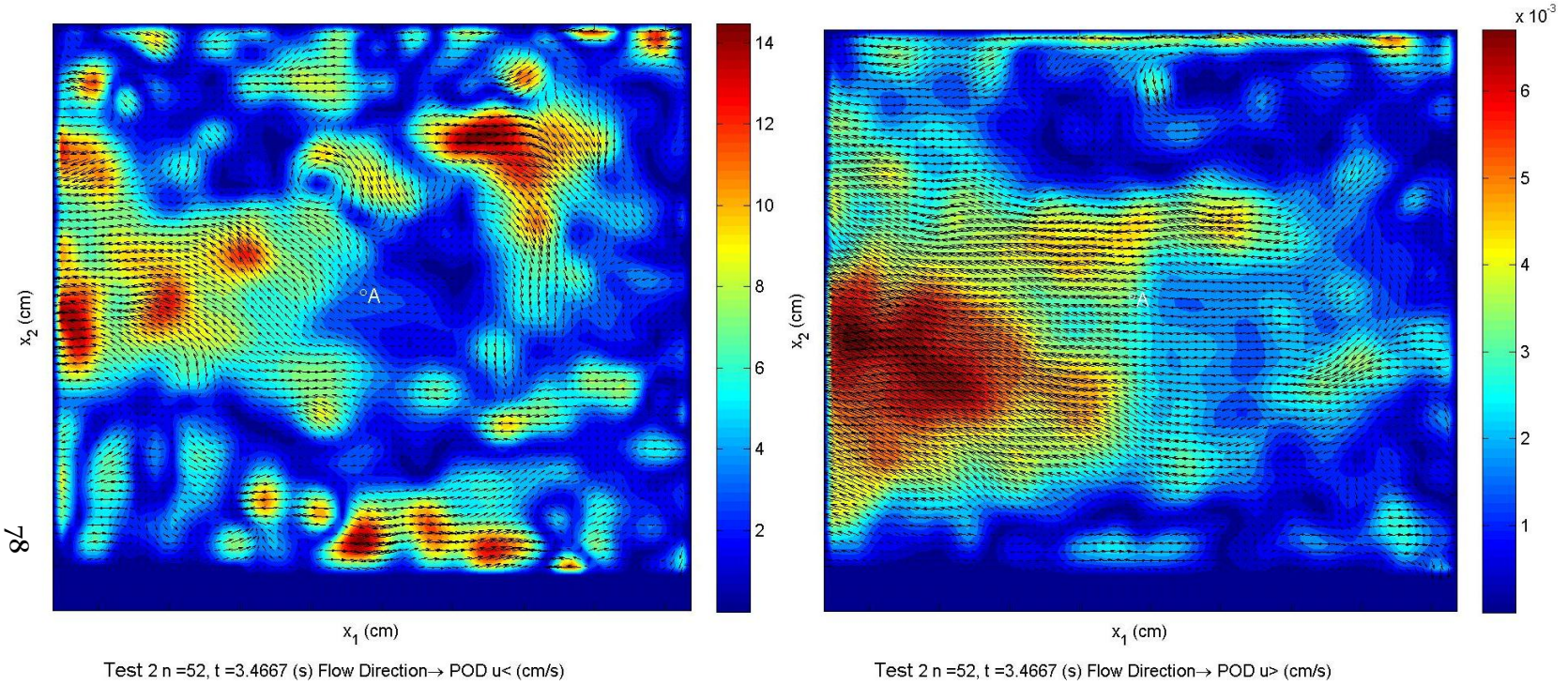

Figure 51. continued

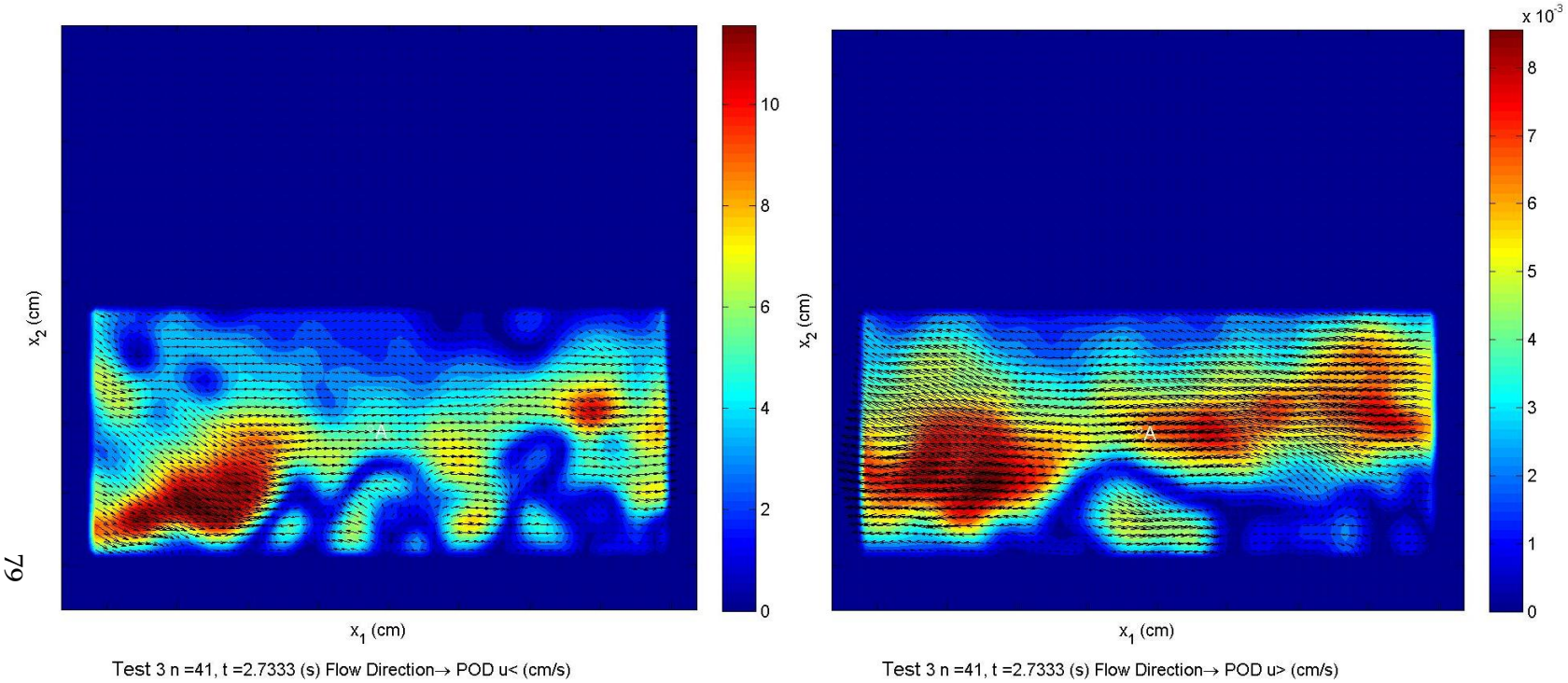

Figure 51. continued

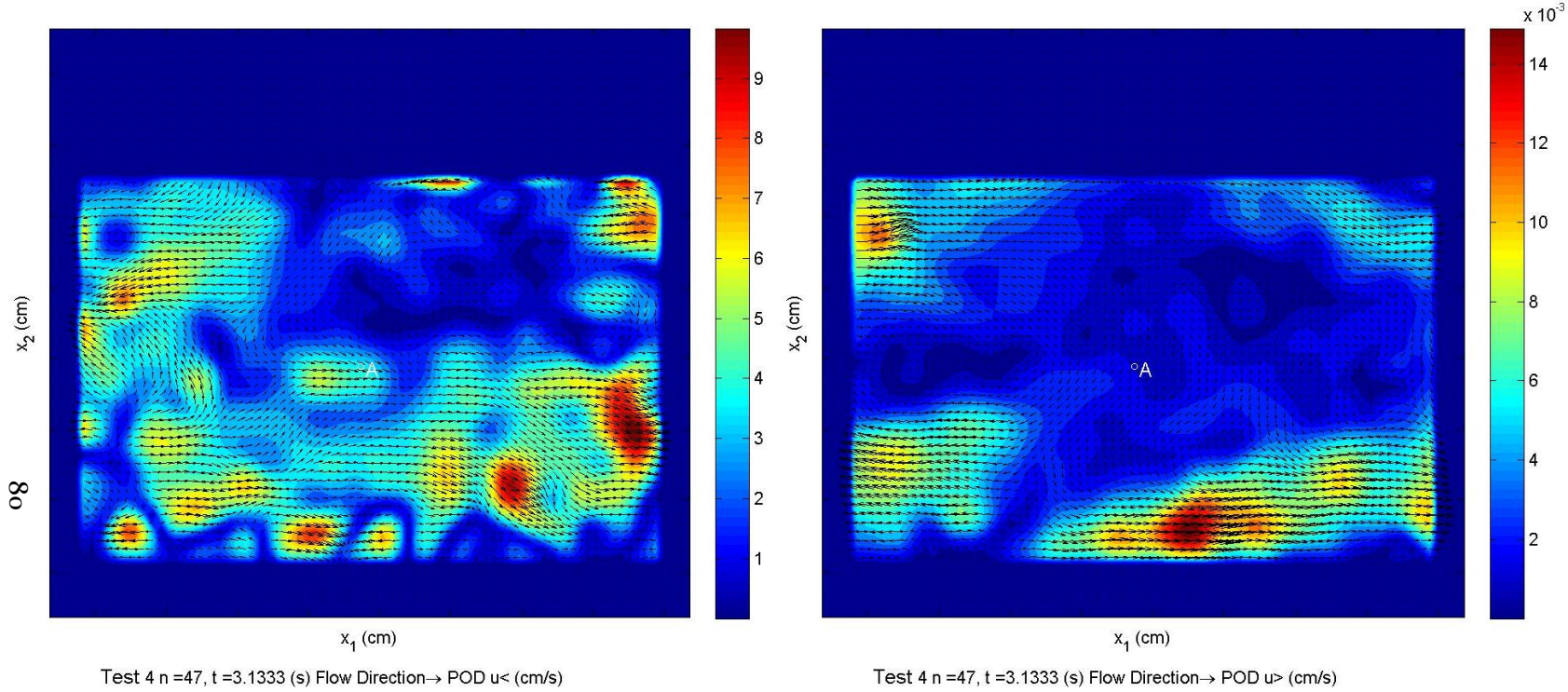

Figure 51. continued

In Figure 51 a color contour mapping of the turbulent velocity magnitude is based on colors typically used in fluid studies and available in MATLAB as the colormap labeled "jet". Here the dark blue color represents regions that are moving at nearly the mean velocity and the bright red color are turbulent fluctuations which are either fast or slow depending on the direction of the velocity vectors indicated by the black arrows. The vectors indicate that the dark blue regions contain vorticity and thin shear layers with topology consistent with previously observed vortex interaction processes in boundary layers.

4.5.2. Vortex Rings

Some smaller observations of coherent structures are shown below in enlarged views of instantaneous turbulent events captured in the POD filtered fields. In the enlarged views the location A is included, the channel half-height, and either the wall or the free-surface for a scale reference.

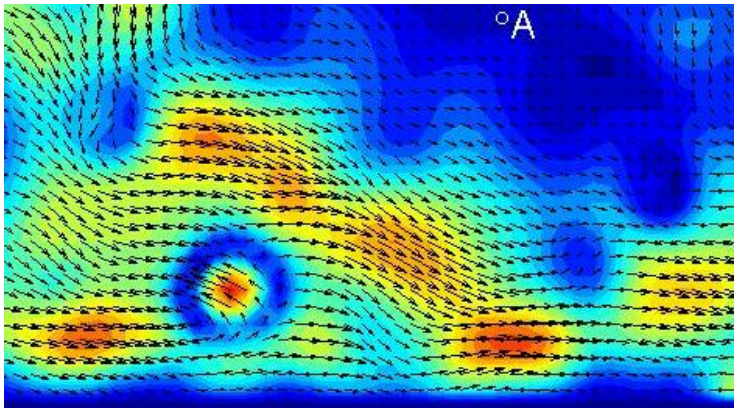

Figure 52. Vortex ring near the gravel bed below the channel half-depth which is denoted by the circle labeled A in Test 4, small-scale filtered field, at time t = 3.7 s

The vortex ring is the approx. 1-cm diameter toroidal-shaped dark region connected to an overlying sweeping motion which measures approx. 4-cm in the streamwise (to the right) direction. The sweeping motion lies between two cyan colored rings which stretch out to form shear layers that separate the sweeping motion from the outer layer and the wall region. The cyan rings have opposite sense of two-dimensional motion in the core region compared to the dark blue ring. The descending sweeping fluid has four centers of high velocity magnitude between these two cyan rings; the resulting vortex system has topology similar to that of a series of joined, or linked, rings spanning the region between the "north" pole of the blue ring and the "south" pole of the cyan ring.

4.5.3. Spanwise Vortex Cores in the Outer Layer

The region further from the wall often contained strong spanwise vorticity focused into a thin section of a long vortex tubes which appear to be connected to other knotted or linked vortex tubes near the free-surface region.

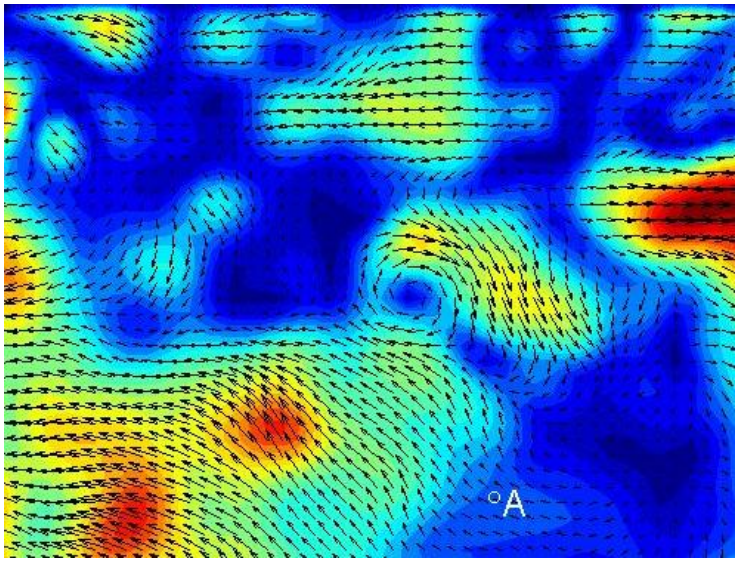

Figure 53. Spanwise vortex core and attached vortex loops (Test 2, u>, t=3.5 s)

Figure 53 shows another coherent structure with a predominately spanwise vortex core that has similar streamwise dimensions as the ring vortices but more commonly occurs in the outer layer under deeper flow conditions. This eddy is more two-dimensional with respect to the field of view and occurs primarily at higher elevations than A. As shown in the figure it is connected to a sweeping motion in the outer layer on its downstream side and a large ejection motion emerging from the inner layer on its upstream side. This vortex core is also connected to multiple centers of high velocity magnitude that appear as connected rings. In this field the "centers" of the high shear stress rings, have direction vectors which slowly rotate clockwise in the same direction as the vortex core in the outer layer.

4.5.4. Vortex Knot Patterns

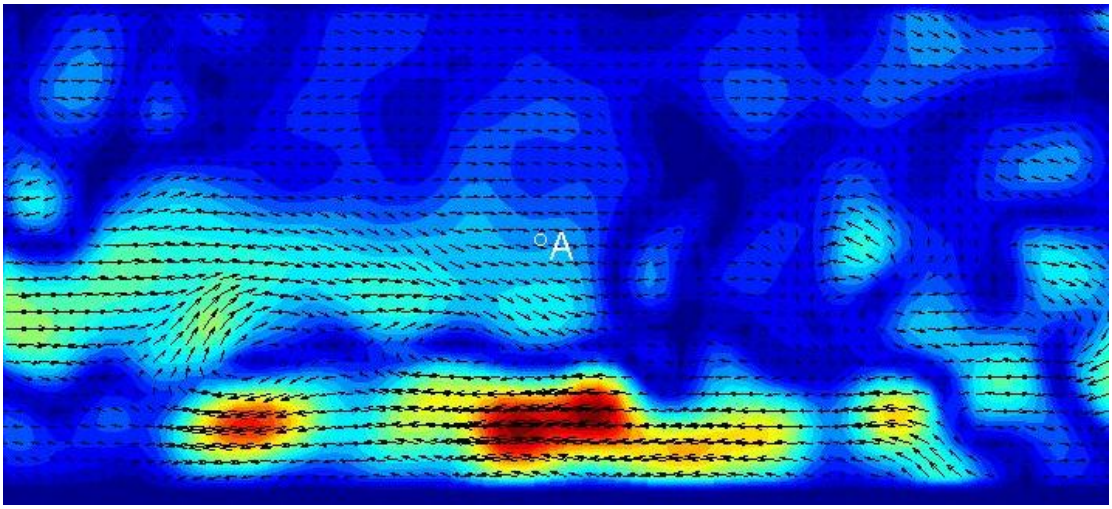

Figure 54. Vortex knot pattern in the outer layer (Test 3, u<, t=0.1 s)

A knot pattern in the long streamwise vortex tubes was evident in all test conditions, perhaps most evident in the large-scale field shown in Figure 54, which shows the entire flow depth. Here the streamwise vortex tubes appear to pass through a larger, presumably

older, ring vortex which has passed into the outer layer and appears more distorted, just to the right of point A in Figure 54. This link overlays a very intense turbulent burst of a long low-speed fluid region at the bed. The linked or knotted vortex tube has similar x1 length but double the x2 length compared to the smaller heads of the vortex tubes observed closer to the wall, e.g. Figure 52. The highest magnitude turbulent fluctuations in the field of view are focused at the bed just upstream of the link which occurs between the long streamwise vortex tube and the twisted vortex ring. The length of the low-speed region near the bed is about 6 cm. The vortex surface separates the low-speed region near the bed and a high-speed region of similar spatial extents and organization. The total streamwise length of this vortex interaction exceeds the field of view, >10 cm. Again the high velocity turbulent fluctuations appear to be grouped into multiple pairings similar to the other observed structures; however, this time they are aligned in the upstream direction. This structure occurs near the beginning of a large downward trend in the time-series of the u-component of Test 3 (see Figure 41) and that the pattern shown below in Figure 55 (small-scale) and Figure 56 (large-scale) occur at the minimum value in the time-series which occurs about half a second later than the link pattern shown in Figure 54.

4.5.5. Linked Turbulent Events, i.e. Ejections and Sweeps

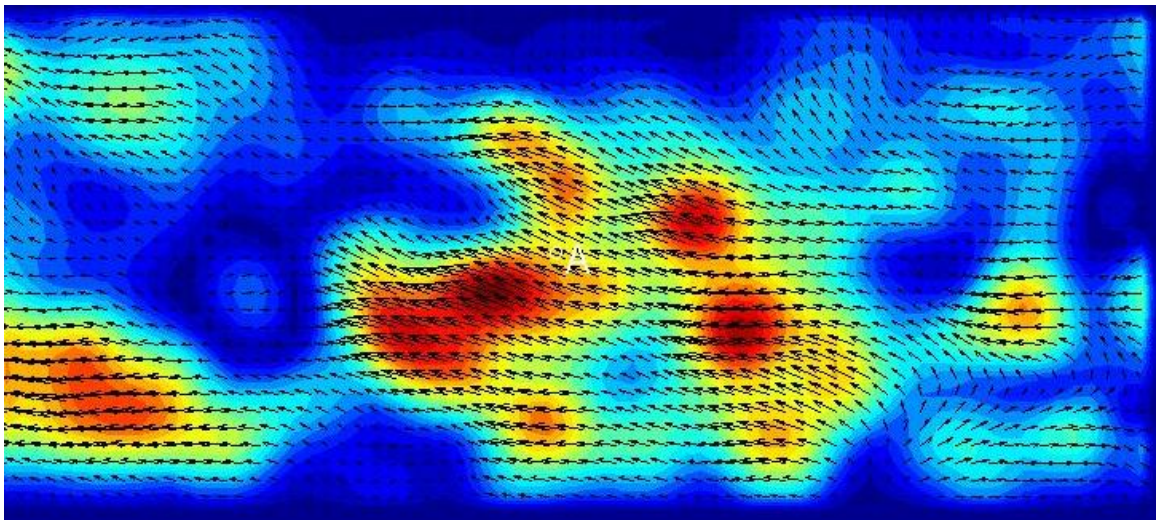

Figure 55. Strongest ejection in Test 3 time-series at Point A, u<, t=0.53s

The strongest ejection of turbulent fluid into the outer layer corresponds to the largest dip in the time-series of point A in Test 3. Figure 55 shows that the characteristic linked vortices are more vertically aligned in this instant and the strongest fluctuations are located at point A. The origin of the ejecting fluid is from a flow separation or discontinuity at the wall on the downstream side of point A which appears as a sharp bend in the normally meandering vortex tubes occurring in a braided structure which is aligned in the streamwise direction. Here the eddy sizes are also ~1 cm dia and vortex rings are evident on either side of A in a pattern similar to the smaller scale version shown in Figure 52. This stronger ejection appears to be connected to a twist or kink in the streamwise vortex tube at the wall. The region near A contains eddies aligned nearly perpendicular to the x1-axis.

4.5.6. *Largest Scale Eddies*

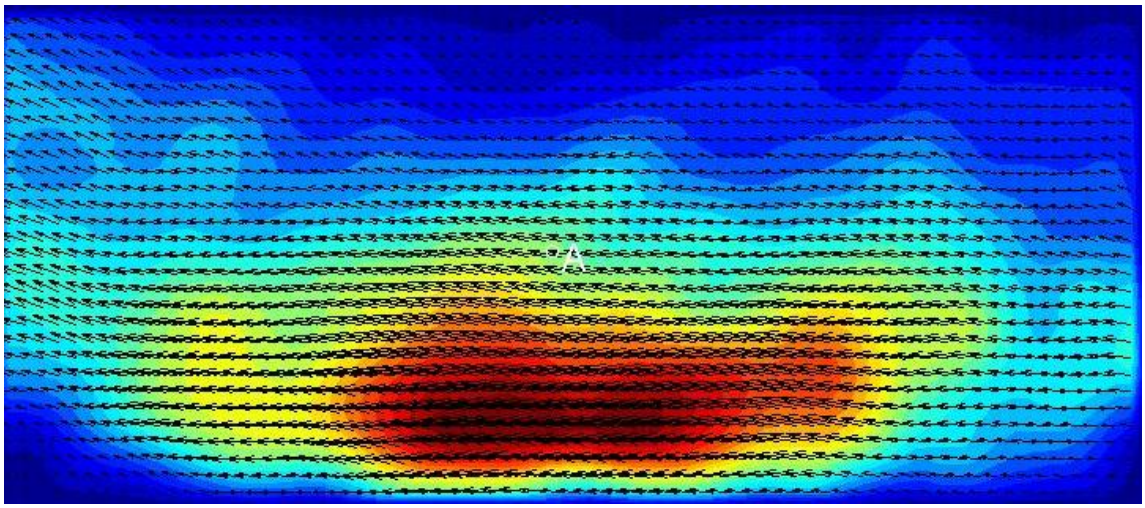

Figure 56. Strongest Ejection in Test 3 Time-Series at Point A, u>, t=0.53s

In Figure 56 the large-scale structure appears as a very large low-speed region which is slowly lifting and spiraling into the upstream direction. The structure resembles a very large version of a packet of vortices as described by (Adrian, Meinhart *et al.* 2000) overlying a low-speed fluid region at the bed. This large-scale motion ejects fluid into the free-surface region to the left side of the figure.

4.5.7. *Separation and Attachment Locations at the Gravel Surface*

The presence of a single, vertically aligned vortex tube is evident in the center of the low-speed region directly beneath A in Figure 56 and think that this tube is the same vertically aligned tube shown in slightly different perspective about one second later, having moved very slowly in the upstream direction along the wall a distance equivalent to the extents of a typical ring vortex tube. The structure now appears to originate at the wall just upstream of A and dissipate into the flow along a sloping shear line that extends in the direction of the flow and lifts slowly from the wall.

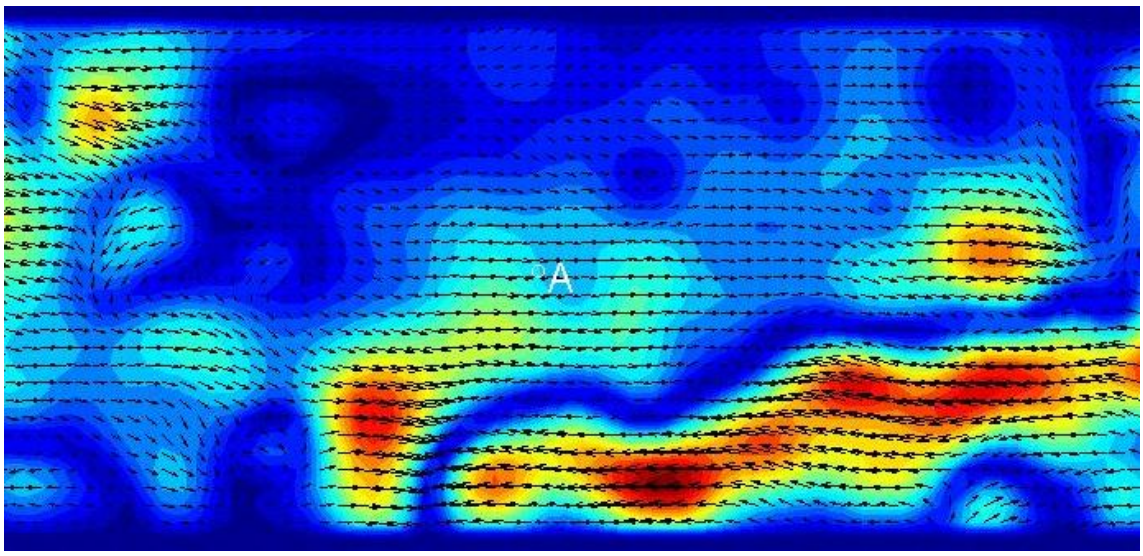

Figure 57. Separation and Reattachment at the Wall (Test 3, u<, t=1.5s)

This structure (Figure 57) could explain the origin of the long vortex tube connected to the upstream end of the knot and the beginning of the low-speed streak at the wall. The highest magnitude turbulent fluctuations in the field of view are focused at the bed just downstream of the attachment point. The vortex surface separates the low-speed region near the bed and a high-speed region of similar spatial extents and organization. The total streamwise length of this vortex interaction exceeds the field of view, >10 cm. The origin of the high-speed fluid is the flow passing into the attachment point from a kink and wall separation point that is due to the presence of the vertically aligned, linked vortex rings (to the left of A). The shear stress at the wall goes to zero at the point of attachment beneath A and further downstream a vortex sheet exists and may create a hydrodynamic lift force in the outer layer. Presumably this lift force would cause the vortex sheet to move with a velocity relative to itself and become twisted, resulting in secondary circulations.

As mentioned above, the vortex knot appears at the beginning of a downward, large-scale dip of the velocity time-series relative to the mean flow and then the local peak (downward) variation occurs some time later. The time-series at later times is generally of lower-variance than prior to the knot and positive with respect to the mean. The gradual increase of the velocity data is approximately linear for a period of 1.5 s (relative to the mean) and this may be explained by the hydrodynamic lift force which is generated by the nearly linear vortex sheet. A large-scale dip in the time-series is evidently due to a vortex knot moving in opposition to the mean flow, followed by a large-scale reattachment of vorticity flux at the wall. The knot is associated with a flow separation point moving along the wall due to a kink-instability of long, meandering streamwise vortex tubes that passes through a region where toroidal vortex shedding from the wall is the important physical process. Each time the separation and reattachment events occur the boundary layer is "reset" and begins "growing" along thin sheets formed by the sloping shear layers. Whereas vortex knotting and flow attachment is the process on the downward limb of the large-scale fluctuations, vortex stretching and amalgamation is the important process on the upwards limb. The later processes do not depend on viscosity; however, the vortex merging processes and kink-instabilities do require the mechanism of viscosity. These processes appear to balance to form the mean flow.

5. TOPOLOGY AND GEOMETRY OF THE VORTEX SURFACE

Our next goal is to formulate a model which has the same topology as these observed vortex interactions and to then use invariant properties related only to the topology of the derived model for describing other physical events observed in rivers. Fluid topology includes the relationship between large and small scale turbulent processes, the turbulent bursting phenomena and other observed fluid motions in rivers and laboratory experiments. A model based on topology is advantageous because it is based on the connectivity, including linking of vortex tubes and connectivity to the bed, of vortices with each other and the surroundings. A topological fluid mechanics model is based on the fundamental conservation laws controlling vortex interactions and thus it is based on physical laws. Also, a topological model enables a four dimensional view (three space and one time dimension) which is the reality for real-time turbulent flows. At the same time, topology is more general and hence can be more abstract as compared to geometry and thus there can be difficulty in the interpretation of the results of a topological model in a conceptual sense. For this reason, immersion, which is similar to a projection for example from four dimensions to three dimensions, of the topological model is used to show the geometry of a resultant vortex surface within the flow. The purpose of the model is to develop a mental picture or backdrop for coherent structures that will help us to test the hypothesis that turbulence structure in gravel beds is organized and thereafter it is hopeful that the vortex model will help us understand and predict the fluid forces that cause portions of the river boundary to move and result in sediment transport phenomena and larger scale cyclic phenomena such as secondary currents and river meanders. Ultimately this model is intended to be used as a tool for understanding and predicting the distribution of velocity and Reynolds stresses for describing the fluid dynamical forces involved in future particle transport studies.

5.1. Building the Smooth Surfaces (Manifolds) Used in the Present Vortex Model

First, consideration is given to the topology of the shapes of the characteristic vortex structures observed in these experiments, including hairpins, rings, long streamwise tubes, braids, knots, groupings of four, twists and larger-scale Reynolds stresses associated with turbulent bursts and secondary currents. It can be observed that all of these phenomena have origin at the wall for the experimental conditions; however, the different phenomena appear to become overlapped at certain times that coincided with lines connecting similar events, i.e. they may have different origins in space and time but overlap in a thin vertical section along the flow region. One possible explanation for these coinciding events is developed below in terms of a bound vortex model.

It is known that the flow contains vorticity and therefore it is possible to divide the vorticity into a bound part which exists inside the wall and a free part which exists outside the wall. This notion is similar to the classical method of images used to describe vortex motions in an ideal fluid except here only viscous fluids and granular walls are considered.

Four generic topological properties, i.e. the most generic properties of the vortex surfaces observed herein, are used to derive the model: (1) small-scale looped or knotted vortex tubes, (2) thin shear layers attached to the heads of the looped vortex tubes, (3) large-scale spiral or circular eddies, and (4) flow separation and attachment of long streamwise vortex tubes at the wall, often accompanied by large scale Reynolds stresses attributed to bursting and large-scale eddies. By a process of deduction and a healthy bit

of trial and error, a form of a vortex surface has been found that recovers most of the observed spatial variations described in the experiments and it will be shown that the purely topological properties of the surface can be used to gain much insight into the large-scale flow dynamics in open-channels through interactions with the water's free-surface region and that further geometrical properties can be easily adapted to a given set of gravel-bed conditions for laboratory flows.

The specific form of the vortex surface is known in mathematics as a Klein bottle and is named for the German mathematician who discovered its form in 1882. It will be shown that the Klein bottle is a manifold that can be used as the vortex model of the structural turbulent organization in gravel bed rivers. The Klein bottle is denoted K^2 and is a smooth space, or manifold, formally constructed via the standard mathematical and topological methods used in fluid mechanics (Moffatt 1969). The basic topological tools used to build the Klein bottle and the other surfaces that will be important in this dissertation. The Klein bottle can be constructed by identification, written symbolically in the squared unit interval $I^2 = I \times I$: identify "/" $0, y \leftrightarrow (1, y)$ and $x, 0 \leftrightarrow (-x, 1)$, or $I^2 / \leftrightarrow \cong K^2$. For reference, a similar, non-orientable two-dimensional manifold, the Möbius strip, is constructed with the same technique. In I^2 identify $0, y \leftrightarrow (1, 1-y) \cong M$ and this method can be used to construct such a one-sided surface out of a strip of paper using tape to identify the edges represented by the intervals in the parenthesis. The type of orientable, two-sided surface that can be created by identification in I^2, $0, y \leftrightarrow (1, y)$ and $x, 0 \leftrightarrow (x, 1)$, or $I^2 / \leftrightarrow \cong T^2$ the 2-torus. In the above notation the symbol '$\cong$' means homeomorphic, i.e. topologically the same. $I^2 \cong D^2$ means that the squared unit interval is homeomorphic, i.e. can be converted via a continuous one-to-one and onto mapping, to the unit 2-ball $D^2 = \{x_1, x_2 \in \mathbb{R} \mid \sum x_k^2 \leq 1\}$. Homeomorphism is weaker and more primitive than deformability (Tokieda 2001). It is customary in mathematical dialect to distinguish between balls, which are solid, and spheres, which are shells only, and to reference the boundary of the solid ball as the 1-sphere $S^1 = \{x_1, x_2 \in \mathbb{R} \mid \sum x_k^2 = 1\}$ which is what in geometry is typically called "circle". In topologic notation the symbol ∂ stands for boundary, i.e. $S^1 = \partial D^2$. These basic building blocks can be used to generate the complicated spaces involved in the study of fluid domains in the present model and this notation is adopted for the derivation that follows. Two basic methods are used in this thesis to construct building blocks of complex fluid surfaces such as the three-dimensional channel domain and three-dimensional vortices shed from the bed; namely, the methods of product and identification. Identification has been described above and the product has been mentioned at the beginning by defining a space made by product of the unit interval $I = [0,1]$ with itself as $I^2 = I \times I$. A three-dimensional fluid domain such as a laboratory flume can be created by producing the 3-cube $I^3 = I \times I \times I$. The method of product can also be used to construct the torus as $T^2 = S^1 \times S^1 \cong$ knotted tube. The exponents here can be easily generalized to n-dimensions, i.e. the n-ball, (n-1)-sphere, n-cube, n-torus.

The Klein bottle is a topological space that is a two-dimensional manifold that can only be created in four-dimensions where it forms a surface which bounds no volume and

passes through itself without any holes, i.e. it has no inside or outside. One can imagine zooming in close enough to such a surface such that a small patch will look like a normal Euclidean 2-dimensional surface. This surface is defined herein as a vortex sheet made of infinitesimal vortex lines infinitely long and arranged next to each other such that they have the same sense of rotation and circulation (Kundu and Cohen 2004). The Klein bottle space is closed and non-orientable; which means that a small symbol can be slid around the surface and returned backwards at the same coordinates in a later time. A symbol slid around a n-sphere or n-torus does not behave this way and always returns the same way it started. A tiny patch of fluid marked with ink must make two revolutions about the large geodesic in K^2 in order to look the same to an observer outside K^2. This is similar to the property known as spin that elementary particles such as gravitons are thought to possess and suggests a possible mechanism for interactions between the vortex surface and the pressure gradient setup by gravity.

5.2. Standard Immersion

First, two different immersions of the Klein bottle are described in this chapter so the characteristics of the Klein bottle topology and geometry can be realized. An immersion is similar to a projection. The photograph of the trout shown in Figure 2 is a two-dimensional immersion of a three-dimensional fish. The graphic models presented below are to be thought of as three-dimensional pictures of the Klein bottle and other topological surfaces as immersed into a subdomain of three-dimensional, real space denoted $\mathbb{R}^3$ and displayed on a two-dimensional subset of real space denoted $\mathbb{R}^2$ coinciding with the two-dimensional surface of the paper, denoted D.

Next the properties of geometry are discussed related to immersions of the Klein bottle. Immersions may have self intersections; however, locally the surface is a normal two-dimensional surface with outside the same as the inside. Immersions are different than embeddings, which do not have self intersections. An embedding is a way to show a topological surface in three-dimensional space such that its connectivity and algebraic properties are preserved. Embeddings of the Klein bottle will be further discussed in the next chapter. The important physical properties that relate the immersion process to fluid problems is that the mathematical version of a flow is a type of map or collections of maps that send fluid particles from one point in time and space to another point in time and space while preserving the volume of the fluid domain, i.e. the fluid domain D induces flow by volume-preserving maps of the interior points of D to other interior points of D (Ricca 2001). For now these flow maps are assumed related to the topology of the Klein bottle and use immersions to demonstrate this conceptual model. Immersion is a special type of map, or flow, which takes input from the surface of the Klein bottle and outputs a point in three-dimensional space, summarized by Eric Wolfram as "[a] special nonsingular map from one manifold to another such that at every point in the domain of the map, the derivative is an injective linear map. This is equivalent to saying that every point in the domain has a neighborhood such that, up to diffeomorphisms of the tangent space, the map looks like the inclusion map from a lower-dimensional Euclidean space to a higher-dimensional Euclidean space" (Wolfram Research 2008). Thereafter, it will be shown using the immersions of the Klein bottle that the topological surface has properties consistent with

- vortices shed for example from the riverbed;

- has characteristics which are reflective of a the large-scale spatial organization of the turbulence;
- has a temporally derived pattern also similar to large-scale fluctuations associated with 'large-scale eddies' observed in velocity time-series data over the gravel beds in section 4 of this thesis; and
- has other geometric characteristics that are consistent with the observed geometry of the mean flow in the fluid domain over a gravel bed.

Because the Klein bottle can capture the characteristics of the organized turbulent structure at different scales in gravel-bed rivers, it will be argued that the topological surface provides a backdrop and set of constraints from which solutions of the governing equations can be described. This argument is further supported due to the invariant properties of thin vortex tubes overlying the surface of the Klein bottle and its adherence to the conservation laws governing vortex motions.

Figure 58 is a graphic of the Klein bottle and is available online (Cambridge 2004) and shows the four fundamental Euclidean building blocks used to create the standard immersion of the Klein bottle, three of which are surfaces of rotation (red, yellow and green) and the fourth is a sheared surface of rotation (slightly deformed vertical blue tube). Using the standard Klein bottle as a conceptual model, the four observed vortex events are labeled using colors instead of numbers as (1) red, (2) blue, (3) green, and (4) yellow as will be further described in the next subsection.

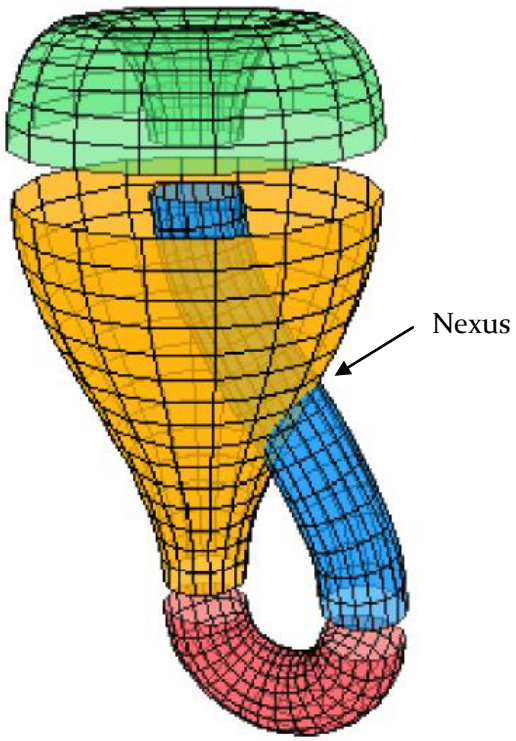

Figure 58. Building blocks of the standard Klein Bottle

In the immersion shown in Figure 58 there appears a self intersection labeled "Nexus". The nexus is a result of the specific type of immersion and may appear much differently or

not at all depending on the immersion selected. This surface is adopted as a conceptual model of the different vortex events observed in the experiments because it captures the connectivity of events, i.e. the topology, and the geometry, i.e. the physical scales of observed vortex patterns, upon rotations and reflections inside the fluid domain. The Klein bottle represents a non-revisiting path in periodic flow of vorticity from the wall to the outer fluid region. The topology is generic and does not depend on the way the Klein bottle is viewed; however, the geometry must be prescribed by stretching and bending the surface as if it were made of rubber and then projecting it into a three-dimensional space via the technique of immersion. How the topology of the Klein bottle describes the sequence of observed vortex events in the experiments is provided next, and then geometry is discussed in a separate subsection. From here on a turbulent burst is defined as a group of events which coincide with a two-dimensional observation plane D which is the two-sided (thus orientable), fluid manifold which has been cut into exactly two parts u> and u< and involves the formation of coherent structures in these vector fields.

5.3. Relationship of the Topology of the Klein Bottle to Observed Turbulent Bursting Events

A typical observed burst was described earlier and indicated by a large-scale dip in the time-series due to a vortex knot moving in opposition to the mean flow, followed by a large-scale reattachment of vorticity flux at the wall. The knot is associated with a flow separation point moving along the wall through a region where toroidal vortex shedding from the wall is the important physical process for generating vorticity that diffuses into the flow. The bursting included a preponderance of (1) thin-cored vortex loops, (2) long, slender, sloping shear layers connected to the vortex loops, (3) large spiraling foci and nearly elliptical vortex patterns, and (4) large scale (u<) vortex reconnections at the wall occurring downstream during strong Reynolds stress events and overlapping at other times with the smaller-scale (u>) vortex patterns. The four observed vortex events are labeled using colors on the Klein bottle instead of numbers as (1) red, (2) blue, (3) green, and (4) yellow and therefore the topology of the Klein bottle can be used to model the connectivity of these events which have been defined above as turbulent bursting. Here it is easiest to rotate the standard immersion clockwise and orient it with the wall as sketched in Figure 59 and so that one may later use a standard boundary layer coordinate system such as shown in Figure 4.

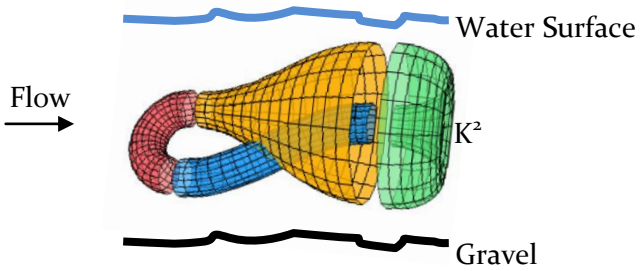

Figure 59. Connectivity of coherent structures in turbulent bursting

The standard immersion of the Klein bottle shows that a burst involves two regions close to the channel boundary, or wall, that are related to the blue building block, which is the sheared surface of rotation resulting from vorticity flux away from the wall in non-linear

patterns during bursting as shown in Figure 57. On the blue part of the Klein bottle one can imagine placing a fluid marker which is a coherent vortex pattern that was frequently observed having origin near the wall and is shown in by tracing the shape of limit cycle lines, which are streamlines drawn by connecting the directions of the instantaneous velocity vector field. This method was useful for estimating the spatial extent of observed coherent structures. In Figure 60 a POD decomposed vector field is plotted which has been color contoured based on the streamwise velocity magnitude to show regions which have fast moving turbulent fluid (red) and slow moving fluid (blue). The limit cycle lines have arrows which indicate the direction of the turbulent motions and the mean flow is from left to right (the vectors have been omitted to avoid clutter). These coherent structures were most easily observed in Test 3 which had the lowest depth of the PIV tests but were present in all tests.

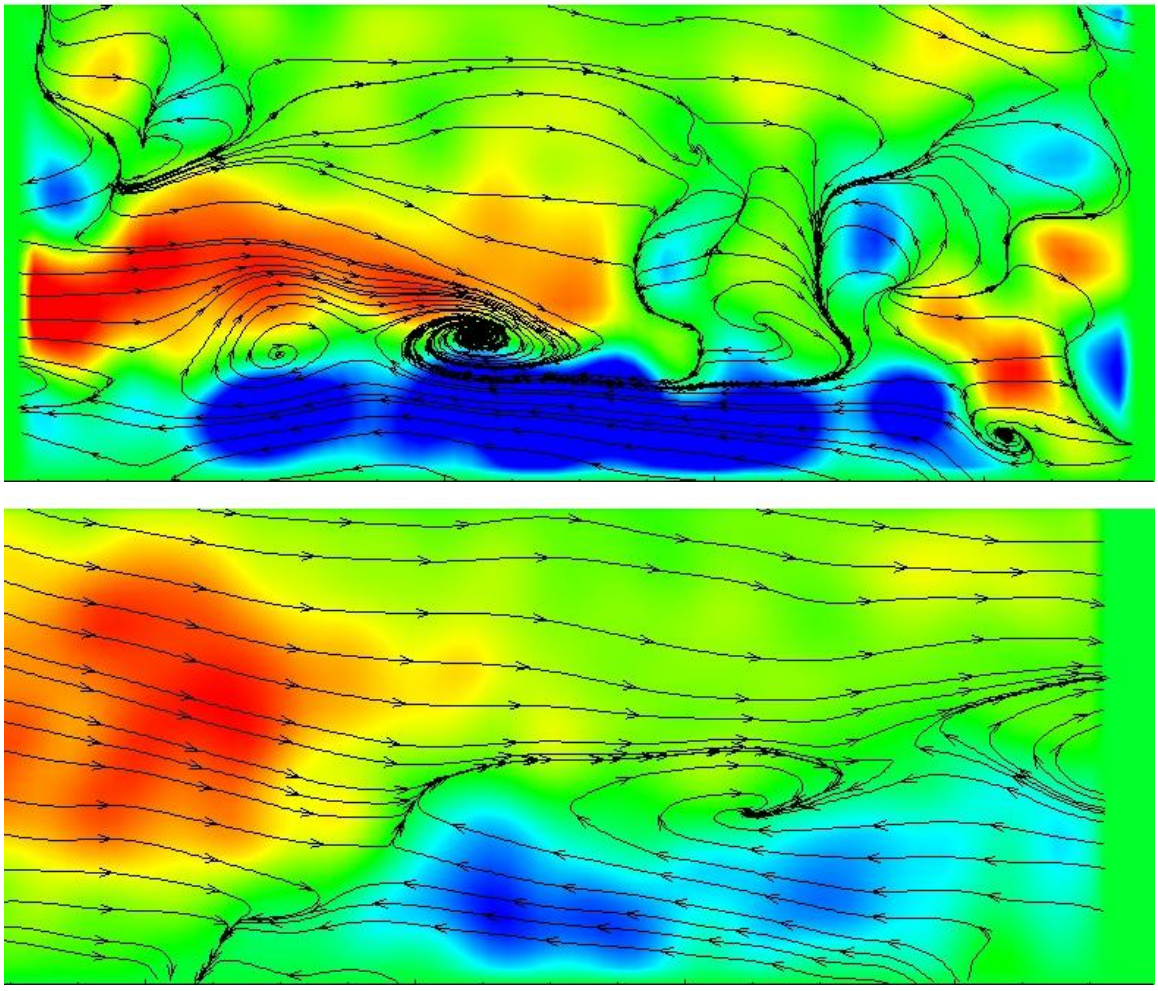

Figure 60. Fluid trajectories in B: small-scale filtered field (top) and large-scale filtered field (bottom)

Using the Klein bottle model shown in Figure 59, it is possible to describe the fluid trajectories of the small-scale coherent structure as knotted vortex tubes, aligned with axes pointing in the spanwise direction, traveling in the streamwise direction along the blue building block or shearing layer. The small scale structure resembles a mushroom cap and is better described by a figure-8 knot pattern than a torus knot pattern. If the

Klein bottle is marked with a non-dissipative fluid marker in a symbol that is the figure-8, the symbol may be moved around the Klein bottle such that it will return at a later time in the same space, but be backwards due to the non-orientability feature of the surface. This is what is shown in the large scale coherent structure at the same time (Figure 6o, u<) and therefore the two are related by the Klein bottle model. Imagine placing a stamp (coherent structure) at the left edge of the blue building block of the Klein bottle which looks like the figure-8 knot shown in (Figure 6o, u>). The structure's history pathlines are found by looking downstream (to the right) through the nexus of the Klein bottle, where a similar structure appears larger and inside out. If time is imagined oriented with the downstream direction then the small eddy coherent structure shown in (Figure 6o, u>) is near the end of time and is connected via the trajectories of neighboring points to a self-similar copy that has passed through the nexus and become rotated and twisted by the bulging portion of the Klein bottle at the right end of the blue building block which turns inside out and becomes the green building block, a pure surface of rotation which describes the large secondary currents known as Prandtl's second kind.

Time constraints of a dissertation limit the ability to show all of the instantaneous snapshots from all the tests; however, here it is concluded by looking at all of the decompositions (snapshots) that in each test case the connectivity between the large eddies and the small eddies can be adequately described by the topology of thin-cored vortex knots embedded on the Klein bottle. During turbulent bursting the fluid trajectories appear to be hyperbolic knots with local stagnation points that follow trajectories along the surface of the immersion of the Klein bottle. The other two building blocks can be viewed as half a torus (red) initially formed and attached to a large particle on the bed, and a surface representing expansion/contraction (yellow) that connects the large-scale eddies to the same surface particle on the bed. The yellow surface represents the space-time manifold of kinetic energy shed from one ring-shaped vortex to the next as described by Nitsche (2001). The Klein bottle includes processes related to viscosity and gradients near the wall (blue building block) and thus has the right topology to describe a steady-state flow of kinetic energy involving vorticity shedding from one ring-shaped vortex to the next in an environment which is representative of the gravel-bed river.

5.4. Relationship of the Geometry of the Immersed Klein Bottle to Spatial and Temporal Scales of Observed Turbulent Bursting Events

Another immersion of the Klein bottle that is conducive to the understanding of turbulence structure as a set of knotted vortex tubes is called the figure-eight immersion. The figure-8 knot is defined herein as a system of linked or knotted vortex tubes overlying the mathematical surface defined by the figure-8 immersion and has spatial structures topologically equivalent to the vortex patterns identified in Figure 6o. The figure-8 immersion of the Klein bottle is useful because it can be used to illustrate vortex interactions observed in the fluid experiments and has the benefit that it allows direct comparison to previous studies of vortex motions involving linked vortex tubes and knotted vortex tubes that travel together in space. In the following, background is presented regarding vortex links or knots, which are topologically equivalent, and then the figure-eight immersion is presented and used to describe the physical scales (spatial and temporal) of observed coherent structures in these experiments and related to the measured particle sizes on the bed.

The simplest case of vortex links or knots were discovered through a thought experiment by J.J. Thomson in 1883, as cited in Ricca et al. (1999). Considering a particularly symmetric system of linked vortex tubes that travel in rigid motions in the fluid, Thomson imagined embedding n = 2 vortex rings equally spaced on the surface of a mathematical torus of radius R and small diameter d. The link system, "can be realized by the following 'thought construction': choose a meridian plane of the torus and place two point vortices (representing the cross-sections of the vortex filaments) on the circumference in diametrically opposite position. Consider now the simultaneous uniform rotation of the two point vortices around the common center of mass (i.e. the center of the meridional circumference) *and* around the principal axis of the torus, along the great circle of diameter R, in the longitudinal direction (see Figure 61). The vortex link system results from the collection of the two point vortex positions occupied after their full (double) revolution" (Ricca *et al.* 1999).

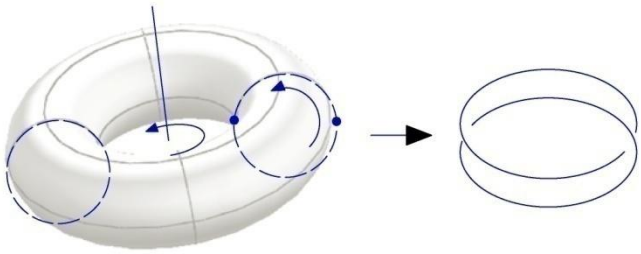

Figure 61. Vortex link system with n = 2 and Lk = 1 after Ricca et al. (1999)

The thought experiment lead to the following theorem: consider a link given by two vortex rings of equal circulation and relative linking number embedded and equally spaced on a torus in a fluid domain. The vortex link system is steady and stable if and only if (Ricca *et al.* 1999)

$$\frac{M(2\pi\rho\Gamma)^{1/2}}{LkP^{3/2}} < 1 \tag{22}$$

where ρ is the fluid density, assumed constant, and $M = |\mathbf{M}|$ and $P = |\mathbf{P}|$ are the intensities of the angular momentum and linear momentum, respectively, of the fluid system. The simplest link system with linking number Lk = 1 rotates and translates with angular velocity Ω and translational velocity V given by

$$\begin{aligned} \Omega &= \frac{\Gamma}{\pi d^2}, \\ V &= \frac{\Gamma}{4\pi R}\log\frac{64R^2}{a^2}. \end{aligned} \tag{23}$$

Higher-order link systems are obtained by increasing the number of full revolutions of the point vortex system in Figure 61. The system can be expanded further by imagining n vortex rings linked together as generated by full revolutions of n point vortices equally spaced on the small circumference around the two principal axes of the torus (in the longitudinal and meridian direction) to generate n-vortex components linked in space. The latter system is steady and stable if and only if n≤6.

Some types of simple vortex link systems were studied via numerical modeling by Ricca et al. (1999), who assumed inviscid (ideal) fluid conditions and discovered that some vortex tubes can be wrapped around a mathematical torus in such a way that they translate and rotate together, forming a stable link or knot pattern (see Figure 62). Other patterns of vortex tubes tended to unfold immediately (see Figure 63).

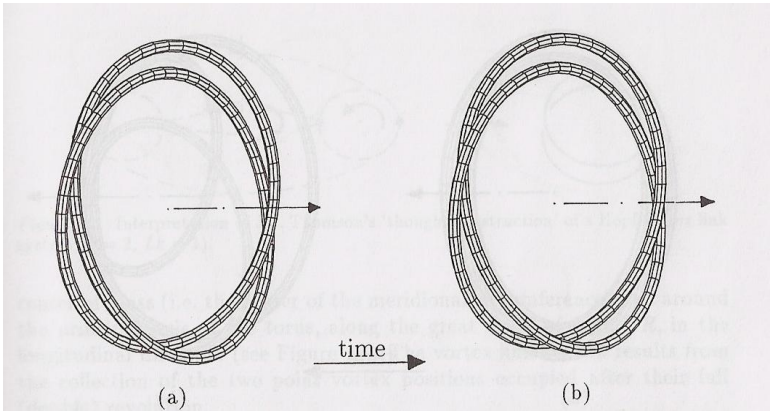

Figure 62. Evolution of T2,3 Vortex Knots after Ricca et al. 1999

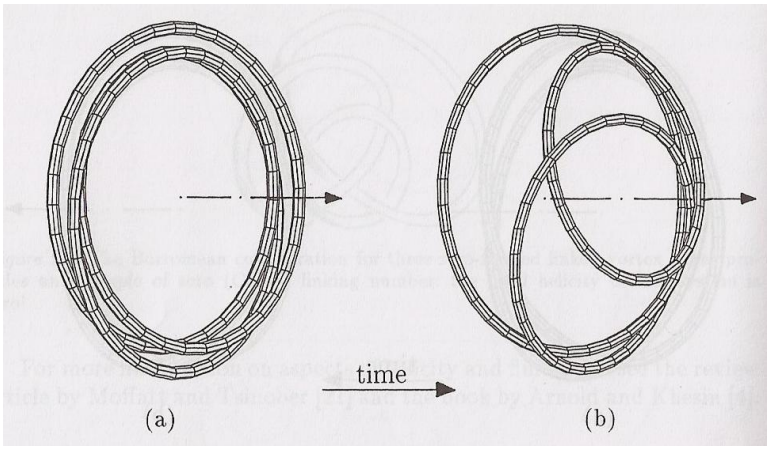

Figure 63. Evolution of T3,2 Vortex Knots after Ricca et al. 1999

The two isotopes of a given torus knot are denoted Tp,q and Tq,p for given p,q co-prime integers. A thin vortex tube embedded on the surface wraps the mathematical torus p>1 times in the longitudinal direction and q>1 times in the meridian direction. The ratio q/p is termed the winding number, W, and the product pq is the linking number, Lk. The winding number and linking number are two topological invariants of the knot type, which means that they do not change under deformation of the knot system. For small amplitude vortex tubes Ricca et al. (1999) finds that Tp,q is steady and stable under linear perturbations only if q>p (W>1).

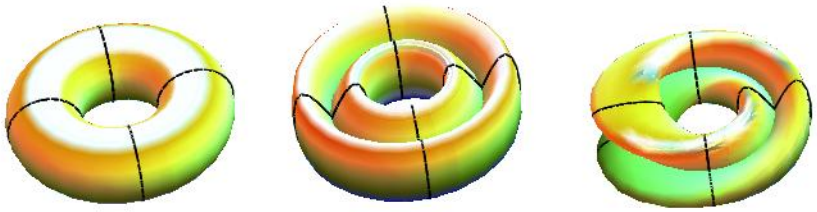

Figure 64. The Torus Knot (A), Figure-8 Knot (B) and Figure-8 Immersion of Klein Bottle (C)

The observed forms of the vortex structures in the present experiments are well described by the presence of thin-cored vortex tubes embedded in the mathematical surfaces shown in Figure 64, similar to the way the vortex tubes are embedded in a torus in Figure 62 and Figure 63, although the thin vortex tubes are omitted to show only the underlying mathematical spaces. Figure 64(A) is geometrically defined by the equations relating the outer diameter R to the inner diameter r of the torus by sine and cosine functions:

$$\begin{aligned} x(u,v) &= (R + r\cos(v))\cos(u) \\ y(u,v) &= (R + r\cos(v))\sin(u) \\ z(u,v) &= r\sin(v) \end{aligned} \tag{24}$$

Here r = 1 and R = 2 have been used because this is known to be approximately the size of toroidal vortices initially shed from individual large grains on the bed of a river where r is a local Euclidean metric such as a statistical particle diameter. This ratio is a good measure for the streamwise length of knotted vortex tubes and vortex loops near the wall.

A simple representation of a figure-8 knot is the space that contains all points such that

$$\begin{aligned} x(t) &= (2 + \cos(2t))\cos(3t) \\ y(t) &= (2 + \cos(2t))\sin(3t) \\ z(t) &= \sin(4t) \end{aligned} \tag{25}$$

for real values of the parameter t. The simplest linked system of hyperbolic knots, as opposed to torus knots described by Ricca et al. (1999), are those which occur on the figure-8 pattern as shown in Figure 64 (B) which is the space made by substituting u = 3t and v = 2t into equation (25), representing the linking of vortex tubes on the surface of the torus which has been deformed into a figure-8 knot via the following immersion equations

$$\begin{aligned} x(u,v) &= (R + r\cos(v))\cos(u) \\ y(u,v) &= (R + r\cos(v))\sin(u) \\ z(u,v) &= r\sin(2v) \end{aligned} \tag{26}$$

which show that the space in Figure 64 (B) is due to a frequency doubling of the sine function argument in the z-component equation for Figure 64 (A) and is just a torus twisted into a figure-8. The resulting space is a manifold for embedding thin-cored vortex tubes arranged in figure-8 knots, or hypersurfaces in $\mathbb{R}^3$. The figure-8 knot is a special prime knot in that it is the knot having the minimal invariant property called volume of knot complement. A prime knot is a knot which has the fewest number of crossings

possible in terms of the linking number in a knot diagram (see Figure 65). The substitution q = u/t and p = v/t was made to compare fluid systems composed of stable linear perturbations of torus knots Tp,q to types of knots which can be described by hyperbolic knots which started out as stable torus knots and then became deformed due to the presence of vortex reconnection events at the wall, i.e. in the presence of a turbulent burst which causes flow to separate from the wall, as shown, for example, in Figure 57. It is known that flow separation from the wall involves hyperbolic geometry of fluid motions (Hornig 2001) which cannot be described by fluid motions induced by stable vortices initially wrapped about a mathematical torus; however, the geometry of these observed bursting events is well captured by imagining stable vortices wrapped about the figure-8 immersion of the Klein bottle shown in Figure 64 (C), visualized by rotating and twisting the figure-8 knot as expressed in:

$$\begin{aligned} x(u,v) &= (R + r\cos(u/2)\sin(v) - r\sin(u/2)\sin(2v))\cos(u) \\ y(u,v) &= (R + r\cos(u/2)\sin(v) - \sin(u/2)\sin(2v))\sin(u) \\ z(u,v) &= r\sin(u/2)\sin(v) + r\cos(u/2)\sin(2v). \end{aligned} \tag{27}$$

The above equations show that the figure-8 immersion of the Klein bottle is obtained by adding a 180-degree Möbius strip to a figure-8 torus. Thin vortex tubes arranged on the surface of the figure-8 would possibly be stable and travel together in groups that have three possible configurations shown in Figure 65, knot group 16. The knot diagrams shown in Figure 65 are reprinted from Tait's original diagrams of prime knots, which are the classes of known knots representing the minimum number of crossings. These large knots, large in terms of linking number, would explain the phenomena of "football-shaped" eddies and secondary circulation cells. The cardinal knot diagrams represent the different views of the same prime knot structure, for example the form on the left looks much like the view looking down into the river with flow going upwards, the view in the middle looks like multiple linked secondary currents in cross-section view (rotated 90-degrees in the plane of the page) and the third view resembles the "inside" view obtained by stripping away 50% of the energy and looking along the channel thalweg as in the experiments.

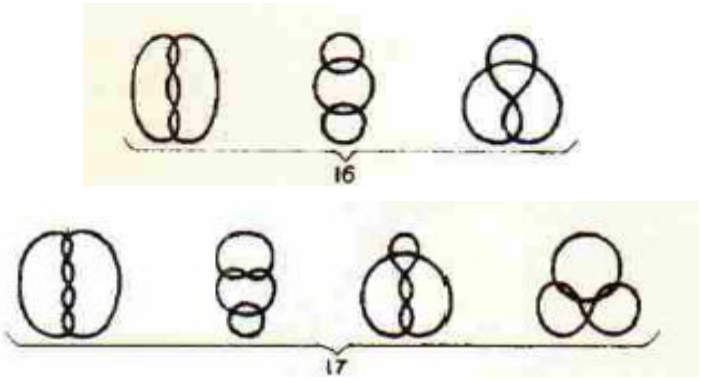

Figure 65. Tait's Prime Knots 16 and 17 Reprinted from (Ricca and Berger 1996)

Any three-dimensional Euclidean space cannot be filled everywhere by invariant tori. Assume the wall region in flow is filling with ring-shaped vortices being shed from individual grains. Then some thin vortex tubes which have formed due to viscous forces on the surfaces of these tori will become linked and translate steadily in the boundary

near the wall and others will open up into the outer layer and become nearly parallel or tangent to the mean flow. A simple model of the large-scale fluctuations in a stable flow would be to consider it as a system of thin vortex tubes arranged in knots which are stable with respect to linear perturbations the same way that some torus knots are stable. This is easy to do in the figure-8 immersion by substituting $v = 2t, u = 3t$ into the equations (27) to derive a parametric form of a vortex knot system that can be embedded onto the hyperbolic surface of the Klein bottle:

$$\begin{aligned} x(t) &= [a + \cos(3t/2)\sin(2t) - \sin(3t/2)\sin(4t)]\cos(3t) \\ y(t) &= [a + \cos(3t/2)\sin(2t) - \sin(3t/2)\sin(4t)]\sin(3t) \\ z(t) &= \sin(3t/2)\sin(2t) + \cos(3t/2)\sin(4t). \end{aligned} \tag{28}$$

Let t represent a dimensionless time scale which is a multiple of the winding number. On the Klein bottle one full cycle is equal to t = 4π, resulting in a temporal structure of fluctuations as plotted in Figure 66 where the y-axis represents the total variance and is interpreted as large-scale eddies. The temporal large-scale structure appears as a packet of vortices, as is evident by the structure of (28) shown in Figure 66, which lasts on the order of ten to fifteen dimensionless time units. In comparison with the previous time-series plots presented in this thesis, it may be concluded that (28) adequately recovers the temporal organization of the large scale turbulent fluctuations as well as cyclic time-trends in the change of larger scale variance.

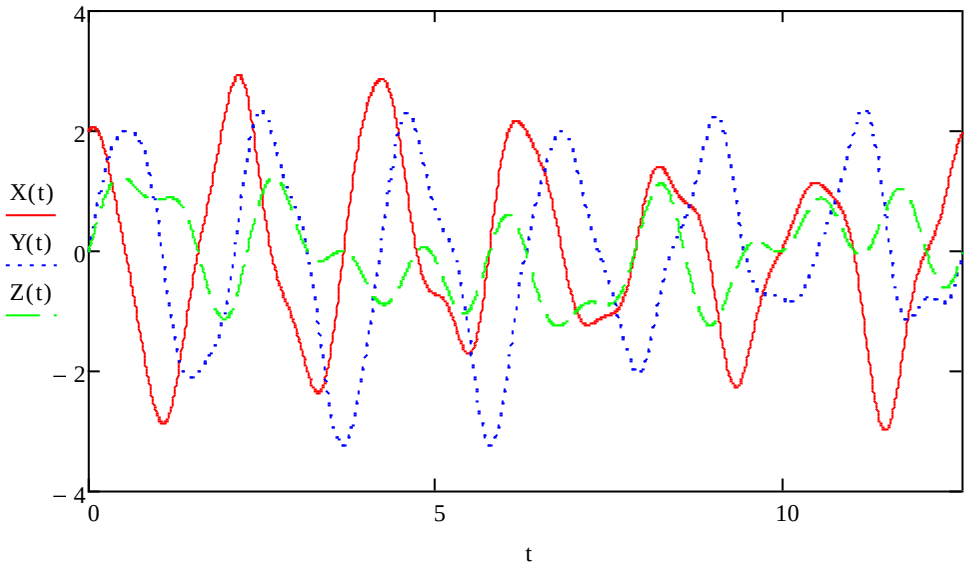

Figure 66. One space-time cycle of a linked vortex system on the Klein Bottle

5.5. Vortex Geometry of the Fluid Domain in a Gravel Bed River

The streamwise fluid domain in Figure 67 is constructed by examining the scale of smaller-scale turbulent fluid motions observable in a POD filtered field as a coherent structural arrangement of vortex motions characteristic of the experimental conditions and responsible for most of the intense Reynolds stresses at the wall.

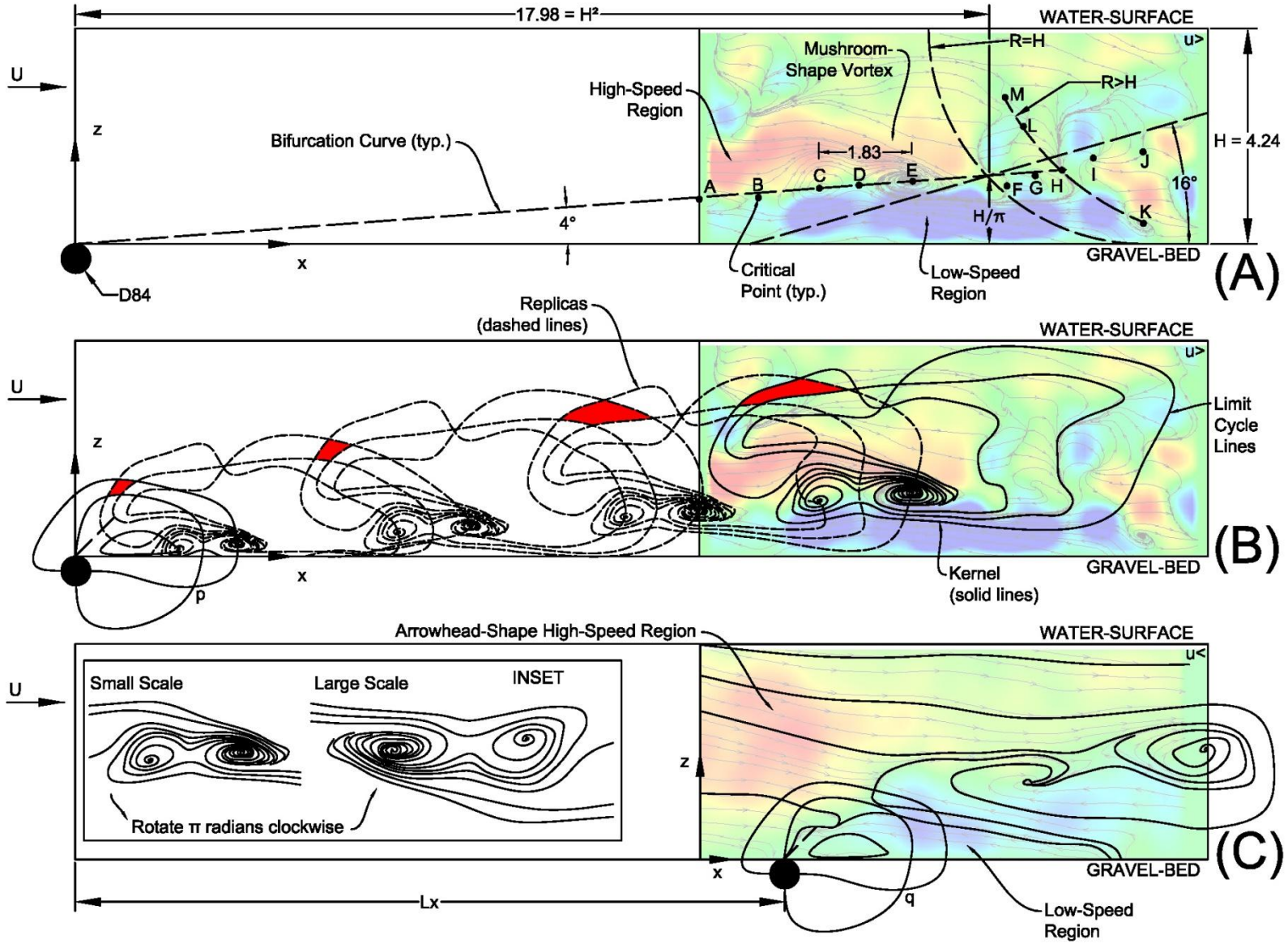

Figure 67. Vortex Knots on the Figure-8 Immersion of the Surface of a Klein Bottle

First the POD filtered field has been placed in a rectangular fluid domain of unknown streamwise length and spanwise width and then determine these dimensions by considering the geometry of the observed features of the vortex surface shown in Figure 60. The geometry of measured flow patterns and the geometric interpretation of the Klein bottle immersion oriented with the flow domain (see Figure 59) have been sketched in Figure 67. Figure 67 (A) shows the geometry of the observed limit-cycle lines in the decomposed vector fields induced by the vortex surface intersecting a wall-normal plane aligned along the flow axis and a POD small-scale filtered velocity field (colored image) is projected into the fluid domain on the right side of the boundary. A line has been extended to the wall in the upstream direction to define the upstream boundary limits. Figure 67 (B) shows the topology of the vortex surface model based on consideration of the limit cycle lines traced from the image and copied and projected along the extended bifurcation line to the origin. Figure 67 (C) shows the simultaneous large-scale event and the relationship between the observed smaller-scale characteristic vortex structure and the observed characteristic larger vortex structures.

In Figure 67-A thirteen of the observed stagnation points have been identified and labeled A-M. In this particular snapshot these points were very nearly aligned in the streamwise-wall-normal plane. The points can be arranged into three groups connected by smooth curves in the two-dimensional fluid domain, shown by dashed lines named bifurcation curves. Two of these groups are arranged along linear bifurcation curves and the other is nearly circular. Points A through H are shown to be nearly linearly connected along an inclination angle $\propto_1 = 4°$ until reaching a certain distance from the wall, shown here as being equal to H/π, where H is the flow depth. Points F through J are shown to be nearly linearly connected along a bifurcation line at angle $\propto_2 = 16° = \propto_1^2$. At point H the $\propto_1$ bifurcation line intersects the group of critical points K-H-L-M aligned along a circular radius shown here as R>H. The circle with radius R=H has been fitted to the point where the linear bifurcation curves intersect. From this intersection the $\propto_1$ bifurcation line has been extended in the upstream direction until it intersects with the wall, where a solid ball has been placed, representing a three-dimensional particle. Consider the bound vortex is a 2-sphere with geometry determined from a statistical measure of particle diameters on the bed, i.e. the D84. A 2-sphere is the surface of the three-dimensional solid ball at the origin of the $\propto_1$ bifurcation curve and consider this to be the origin of the turbulent structure on the wall, similar to the idea of a wing-tip vortex in the lifting-line theory. Here the value D84 is used to represent a typical large particle at the origin. The $\propto_1$ bifurcation curve is the portion of the vortex surface that lifts from the wall at a low inclination angle and is composed of stagnation points uniformly distributed and composed of alternating eddies with spiraling or nearly elliptical foci, i.e. points A, C and E, and saddle nodes, i.e. B and D. The alternating pattern of foci and saddle points C, D, E is found by tracing the lines to which all other streamlines asymptotically approach. These asymptotes have been termed limit cycle lines, bifurcation lines and other names (Panton 1996). If these asymptotes lie on the wall then they are usually called separation or attachment lines. The presence of these bifurcation lines and separation regions means a fully three-dimensional velocity field. The characteristic small-scale structure observed in these experiments is the pattern of limit cycle lines that wrap around three adjacent stagnation points, such as C-D-E, forming a mushroom shape with clockwise sense of rotation on the outside of the cap. The inside of the cap has the same sense of rotation but is divided unequally in two spirals (see inset Figure 67-C).

In Figure 64-B the topology of the organized turbulence structure is constructed using a kernel for the vortex pattern shown in the flow patterns of Figure 64-A. The kernel for the vortex pattern is developed first by constructing a three-string braid of limit cycle lines that matches closely the observed topology of the structure C-D-E and then filling a larger fluid region with self-replicas. The vortex surface is constructed based on the idea that the characteristic mushroom shapes in the smaller-scale turbulent field represent an attracting region in the solution space of a dynamical system, which is the same concept as a coherent structure in turbulent velocity fields (Lumley 1985). To develop the model, the vortex kernel is distributed on the real line based on topological considerations Holmes et al. (1998). The upstream limits of the fluid domain extends of the fluid domain were determined based on the geometry shown in Figure 67-A. Further, a fluid domain was chosen that is larger than typical observed mushroom-shaped structures in the smaller-scale fields but as described in Holmes et al. (1998) not be too large, in which case too many of the typical coherent structures would inhabit the physical space for a simple model to apply. For now a spanwise width of the fluid domain is on the order of the flow depth, H. Next copy, translate and scale the kernel pattern uniformly along the $\propto_1$ bifurcation curve until it ends at the origin, as shown in Figure 67-B. This construction method preserves the geometry of the observed stagnation points only each copy is connected to the one on the downstream end through the stagnation points on the bifurcation curve, thus preserving the topology of a closed vortex surface. The curves stretch slightly outside of the mushroom caps so that the strings pass through the stagnation points of the adjacent downstream copy.

In Figure 64-B, a total of four of these kernel structures fit along the $\propto_1$ bifurcation curve, leaving a gap between the origin and the first eddy approximately equal to the streamwise width of the mushroom cap C-D-E. Here it is important to note that the uniform spacing of the stagnation points is preserved, i.e. eddies that are nearly two-dimensional in this view appear to be growing from the origin and expanding at a uniform rate. The portions of the bifurcation lines sketched in Figure 67-B outside the mushroom caps are intended to show the topological nature of the vortex surface and not the specific geometry of streamlines, i.e. they are intended only to show how the structures are connected outside the two-dimensional view of the mushroom caps. Regardless, the three-strings outside the C-D-E mushroom cap describe the real fluid streamline motions closely. The sketch suggests that the surface is twisted such that the three strings cross in the outer layer once for each loop around the outside of the mushroom cap. The process of translation created additional crossings in the outer layer such that the strings in each kernel cross the strings of the adjacent downstream kernel in a similar pattern, forming a net above the mushroom caps of curvilinear rectangles, that appear to distort in a uniform manner and rotate clockwise in the flow until reaching the most downstream, original kernel. One curvilinear rectangle has been shaded red at each crossing in Figure 64-B. At the most downstream such crossing in the outer layer the curvilinear grid passes into the self-crossing of the original kernel structure, just above the most downstream eddy. The linked strings in the outer layer will be discussed further below in terms of the larger-scale structure of the vortex model.

The vortex surface which composes the space-time manifold, i.e. the Klein bottle denoted K^2, is composed of threads which are vortex lines intertwined with streamlines such that when viewed "close enough" the surface looks like a Lamb surface, which is an orthogonal net providing coordinates of equilibrium solutions to Euler's flow equations;

however, when viewed at larger scales the surface is closed and more abstract. At the large scales the vortex tubes which are the threads of this surface visualize as hairpin vortices which form in regions of high amount of local curvature on K^2 and travel to regions of nearly constant curvature. Regions of constant curvature are the Euclidean building blocks formed by surfaces of rotation, i.e. lines of constant circulation, which trace out portions of K^2 as hairpin or "horseshoe" vortices move by self-induction from regions of high curvature gradient to regions of more constant curvature gradient. The geometrical alignment of a streamwise axis in the wall using a boundary layer coordinate system (see Figure 4) immediately recovers the sheared surface of rotation, the remaining building block needed to connect the pieces of K^2 in the fluid domain. A sheared surface of rotation implies high velocity gradients, as would be expected to occur near the wall in a laminar shear flow. This gave us the idea to select a specific immersion of K^2 to describe the geometry of the spatially coherent structures as shown above in Figure 67.

Detailed streamline geometry (in black) of the kernel pattern are shown as horizontal and vertical measurements (in red, respectively) in Figure 68 where flow is from left to right and the vortex is shown connected to the bed and extending vertically to the free-surface region. The rectangular boxes in Figure 68 are drawn for reference and do not indicate fluid streamlines.

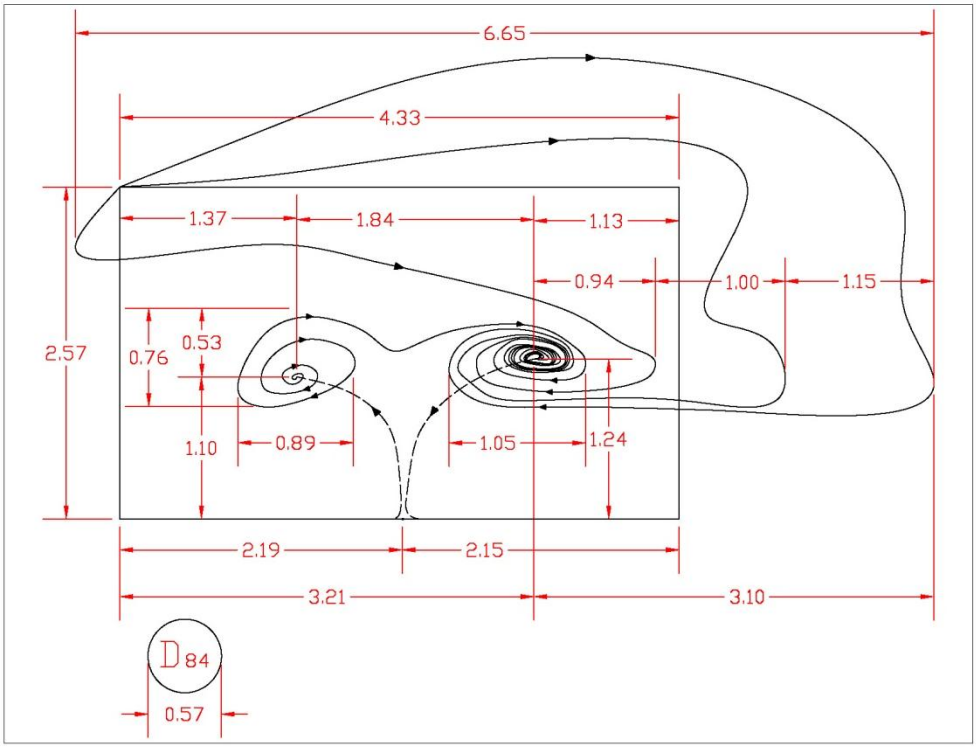

Figure 68. Fluid geometry and measurements in cm of a small-scale eddy and vortex knot pattern observed during a turbulent burst in the CE flume with particle size distribution of bed material represented by the equivalent circle diameter D84 shown for scale comparison

Figure 68 shows that the small-scale eddies associated with a particularly violent turbulent burst scale with the D84 particle size, i.e. the vortex contains foci spaced about 2 such diameters apart and the eddies visualize as vortex cores with sizes approximately 2

diameters. The vertical scale (2.57 cm) indicates that the small-scale eddy size scales with the flow depth in the wall-normal direction for this test.

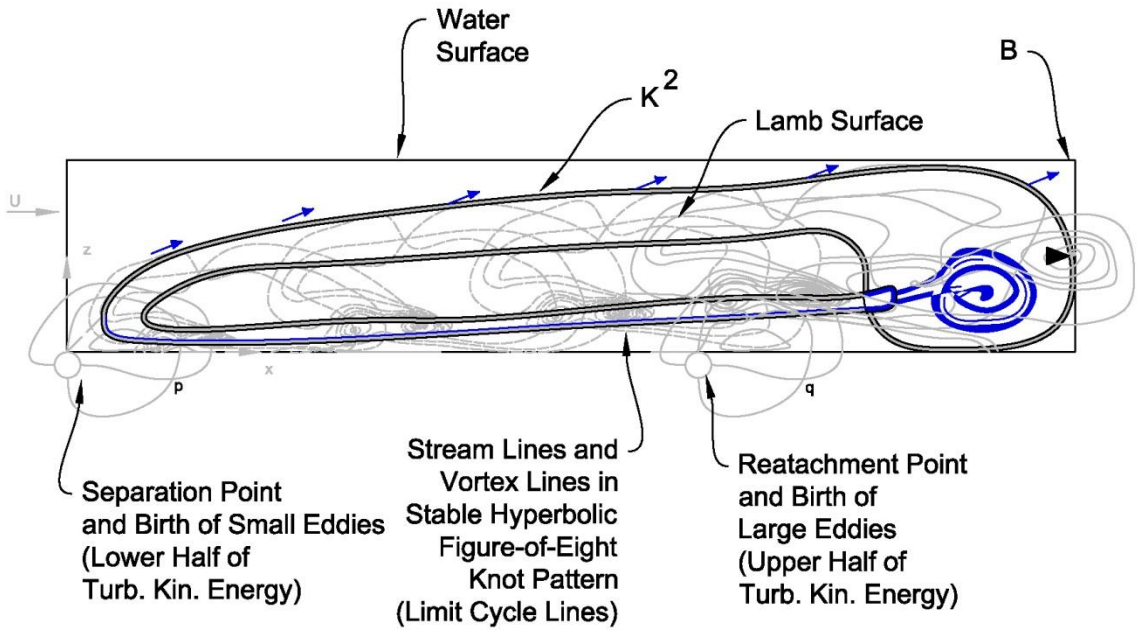

Figure 69. Organizing turbulent fluctuations in a gravel-bed fluid domain

Figure 69 implies that regions of B which contain the standard projection of K^2 contain limit cycle lines arranged as a figure-of-eight knot pattern in the sheared region of circulation near the wall and imply that the fluid motions outside the projection in B are self-similar but larger copies of the knot patterns that form in the sheared region. This particular diagram represents a time of maximum production of shear at the wall associated with turbulent bursting and streamwise low-speed streaks. At this instant the flow across the downstream boundary of B is dominated by the flow over a vortex sheet and not the viscous fluid properties which are important near the wall and less important in the outer region. The circulations in the sheared region have a consistent sense of orientation, i.e. they all rotate clockwise. Since they pass through the apparent self-intersection of K^2 they become inside out and appear larger on the downstream boundary; however, the topological property known as the knot invariant remains the same on the boundary. This allows us to attach a downstream boundary condition which is based purely on the topology of the fluid paths induced by $K^2 \times B$. The boundary condition is the knot invariant called hyperbolic volume of knot compliment, which is simply the volume in B which is not inside the figure-of-eight knot. The upstream boundary is located at a flow discontinuity at the wall where the local wall shear stress obtains zero magnitude. This fluid domain B is well described as the solution to an Euler flow having slip conditions at the wall in which the energy dissipation is being maximized.

5.6. Summary of the Vortex Model

The focus of this chapter has been to derive a model with topology and geometry similar to observed fluid motions in a turbulent open channel flow. Flow visualization results which separated the total instantaneous velocity field into large-scale eddies, u<, and small-scale eddies, u>, were used to educe coherent structures. The Klein bottle has been shown to provide the mathematical space in which stable vortex knot patterns exist

in the fluid domain. Another interesting topological feature of the Klein bottle further allows a model of the connectivity between the large scales to the small scales by cutting the fluid domain into two parts which both contain half of the total turbulent kinetic energy, i.e. half of the variance. A Klein bottle only appears to have self-intersections in B; however, the surface really does not intersect itself and thus can be cut into two Möbius strips as shown below in Figure 70, representing the two faces of a thin vertical sheet oriented along the two-dimensional boundary layer coordinate system in B. This topological feature shows the connection of the POD filtered fields and how they appear to coexist in the same fluid space B and both may have vortex tubes embedded and attached to the wall in the same region. The remarkable property of the Klein bottle is that it can also be cut into a single Möbius strip (not shown) by cutting the figure-8 immersion instead of the standard immersion. This shows that the same topology can be used to describe layering effects described by previous research on the structure of turbulence in open channels, e.g. Nezu and Nakagawa (1993).

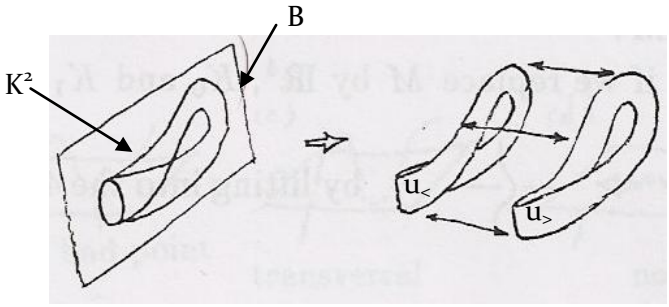

Figure 70. Slicing a Klein Bottle after Tokieda (2001)

To summarize this chapter, it has been shown that a vortex surface having the topology of a Klein bottle can be used to develop a model of vortex interactions in a gravel-bed river environment, thus supporting the main hypothesis, which is that a structural organization of turbulence exists in gravel-bed rivers. A specific model has been presented to demonstrate the usefulness of researching this hypothesis and have shown that much is learned in the process of developing such a model. In the next chapter an extension of the model is used to describe additional structure in the time-average wall-normal velocity distribution, commonly called velocity profiles, which further supports the main hypothesis and suggests avenues for future research involving this vortex model and gravel-bed rivers.

6. IMPLICATIONS FOR THE WALL-NORMAL VELOCITY DISTRIBUTION IN RIVERS

So far it has been demonstrated that the current results support the hypothesis that a structural model of turbulence organizes turbulent fluctuations in rough, steady-open-channel flows, which are close relatives of other turbulent boundary layer flows. A specific model of this structure which is a vortex surface having topology of a Klein bottle was developed in the previous section and it was shown that the generating parts can be used to describe the individual components of the small-scale velocity fluctuations and that its connectivity provides a way to conceptualize how these different types of fluid motions are related. Next, some predictions regarding the global fluid geometry are made, i.e. how the average velocity varies relative to distance from the average gravel-bed surface in a river. Geometry, being less generic than topologic concepts such as "homeomorphic", depends on the extrinsic concepts such as width, depth and particle sizes which can only be determined using some sort of statistical averaging procedure.

An additional structure has been observed in these experimental flows which appears to be related to the topology of the figure-8 knots described in the previous chapter. An extension of the model is to develop a useful method to collapse measured velocity profiles in rivers which all have the same amount of turbulence structure, i.e. vortex motions governed by immersions of Klein bottles. A steady-state mean flow in gravel-bed rivers does allow a similarity solution approach for these experiments, an approach which includes a pressure gradient parameter that may be related to knot invariants of hyperbolic knots, specifically the figure-of-eight knot, as a fundamental shape parameter. While this needs further research and data collected in gravel-bed rivers, the following discussion is provided to suggest that there is good reason to continue to adopt a coherent structure approach in the study of other aspects of gravel-bed rivers.

It can be seen in Figure 69 that all of the streamwise flow comes from the knot compliment in B and thus must be related to the volume of the knot compliment, which is a hyperbolic volume and knot invariant that only depends on the topology of the knot diagram on K^2 x B. This knot invariant, the volume of the knot compliment, is only known for the figure-of-eight knot. On the downstream boundary the point of maximum velocity is located above the arrow pointing to the center of the large eddy in B. This velocity, denoted now U_∞, only depends on the distance from the wall and the volume of the knot compliment and occurs at a point δ in analogy with boundary layer theory. If the Klein vortex surface is always present; however, perhaps not visible due to the specific form of the immersion, then δ will always depend on the same hyperbolic volume as it is a flow invariant that is unchanged by the external conditions. The hyperbolic volume (knot invariant) of the figure-of-eight is known exactly (2.0298832...). The time-average filament of maximum velocity in a river is expected to vary as a function of distance from the wall while obeying some sort of similarity collapse which uses this number. The simplest relationship being a power function of the form $\delta \sim U_\infty^n$ where n is a simple function of the knot invariant.

It is possible to derive a theoretical velocity profile for these conditions by adopting a similarity analysis approach previously used for boundary layer flows having positive pressure gradients, which is consistent with the present experiments. Next it is shown that a similarity collapse exists for these and other boundary layer flows and that the non-linearity parameter may be related to the hyperbolic volume of the figure-of-eight knot.

The notation of past research applied to smooth boundary layers is adopted to show that this flow property (non-linearity parameter) does not depend on geometrical considerations such as roughness size but rather to "momentum deficit thickness" (Castillo and George 2001) which is closely related. Finally, the model is adapted to specific roughness geometry by incorporating the effects of generating vortices with spacing determined by the statistical measures of the roughness sizes and find that the velocity data from different experiments can all be collapsed onto (nearly) a single curve in the boundary layer.

The typical derivations of flow velocity laws in rough channels have been modifications of the boundary layer equations that account for roughness at the wall, which result in some sort of modified log-law which requires curve-fitting to measured data in order to compute shape parameters related to the shear stress at the wall and roughness elements. Recent attempts, e.g. (Termini and Greco 2006), have also included modifications to explain observed vertical profiles in rough channels that have curvature such as 's-shapes' and 'dips' that otherwise are not explained by the derivations of the log-law which only allows for increasing functions. The shape of the vertical profile and the dependence on hydraulic conditions remains an important research topic. New similarity collapses of the boundary layer equations have been used to collapse velocity vertical profiles for hydrodynamically smooth conditions, e.g. Castillo and George (2001); revealing a universal similarity solution; however, this type of scaling does not appear to be used in typical applications in rough channels.

Boundary layer equations were fitted to these experimental data and it was found that although empirically fit log-law equations may be adjusted to fit in the core regions of these data, and thereafter a piecewise-smooth curve derived to fit each section of the data, there is not an explanation for the variability in the curve-fitting parameters, for example a wake parameter, to describe physical processes involved in the curvature near the free surface. The log-law does an adequate job for curve-fitting in the narrow region just above the buffer layer at the beginning of the outer layer; however, the thickness of the buffer layer is an experimentally determined parameter in this case and may not be known *a priori*.

Next an apparent trend in these data was found upon plotting the base-10 logarithm of U_{max} plotted versus the base-10 logarithm of δ, as shown in Figure 71.

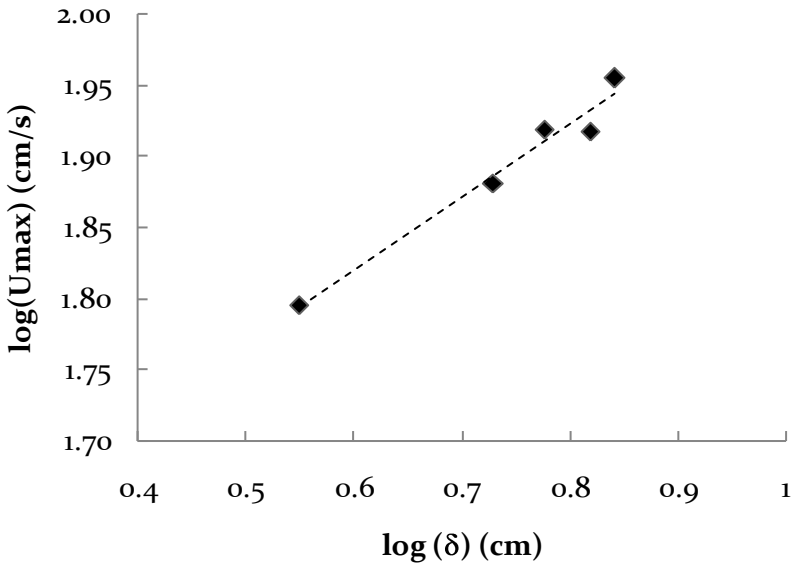

Figure 71. Log-log plot of U_{max} vs. δ (Λ=-1.95)

Figure 71 indicates that these flows do satisfy an equilibrium solution approach for predicting the velocity distribution from the wall to the top of the boundary layer (Castillo and George 2001). Equilibrium solutions have been suggested therein that fit a straight line when plotted as logarithms in consistent units, as in Figure 71 where the equilibrium parameter value n = 0.5128 is the slope of the best fit (dashed) line and the Castillo and George pressure gradient parameter is defined by -1/n = Λ = -1.95. Surprisingly, these values agree well with apparently all measurements of velocity distributions made in smooth boundary layers with favorable pressure gradients. According to Castillo and George (2001) there are apparently only three values for Λ, 0.22, 0 and -1.92, that collapse all smooth-bed turbulent boundary layers for adverse, zero and favorable pressure gradients, respectively. The present test data are within experimental error of the value given in Castillo and George (2001) for favorable pressure gradients, indicating an important validation and extension of this type of velocity-deficit similarity collapse to open channel flows with rough beds. Our hypothesis is justified by noting that Λ=-HV where HV is a hyperbolic knot invariant of the figure-8 knot patterns observed in the spatial velocity fields organized by the K^2 immersion during turbulent bursting. This obviously needs further research and justification. The similarity analysis is further described below and it is shown that velocity profiles for these tests may be collapsed into a single structure.

Based on the equilibrium approach of Castillo and George (2001) a similarity solution approach is extended to gravel-bed rivers in the following paragraphs.

The Navier-Stokes equations written in Einstein notation for an incompressible fluid are

$$\frac{\partial u_i}{\partial t} + u_j \frac{\partial u_i}{\partial x_j} = -\frac{1}{\rho}\frac{\partial p}{\partial x_i} + \nu \frac{\partial^2 u_i}{\partial x_j \partial x_j} + g_i \qquad (29)$$

where u_i is the instantaneous velocity vector field, p is the instantaneous pressure, t is the time dimension, x_i is the spatial vector, ρ is the water density, ν is the kinematic fluid viscosity and g_i is the vector of gravitational acceleration given by:

$$g_i = -gn_{vi} \tag{30}$$

where g is the magnitude of the gravitational acceleration and n_{vi} is the unit upward normal vector. The above equations define the relationship for momentum and the relationship for continuity is

$$\frac{\partial u_i}{\partial x_i} = 0. \tag{31}$$

Examination of the variations in velocity distributions is also examination of the dynamics of these governing equations. In typical engineering applications in river mechanics, the equations are simplified and appropriate boundary conditions are specified to produce a representative model of the flow. Consider a fully developed flow in a bounded domain with notation as described in Figure 4. For the governing equations to be applied to rivers it is typical to adopt a slender flow approximation, similar to boundary layer and other turbulent flows, in which the changes in streamwise length scales of the boundary and of turbulence are assumed to be much more gradual than the changes in the wall-normal direction. The flow typically changes much more slowly in the streamwise direction than other directions in river applications. This is the key assumption in boundary-layer type flows. To perform the slender flow approximation, a Reynolds decomposition of the velocity and pressure fields is performed to average over the effects of turbulence: $u_i = \overline{u}_i + u_i'$, $p = \overline{p} + p'$, with the overbar representing the expected values of velocity and pressure using an averaging procedure and the primes denote the fluctuating part of the velocity and pressure fields that contain both the coherent structures and the incoherent or less coherent turbulence. The averaging procedure results in the Reynolds equations for momentum and continuity:

$$\frac{\partial \overline{u}_i}{\partial t} + \overline{u}_j \frac{\partial \overline{u}_i}{\partial x_j} = -\frac{1}{\rho}\frac{\partial \overline{p}}{\partial x_i} + \frac{1}{\rho}\frac{\partial \overline{\tau}_{vij}}{\partial x_j} + \frac{1}{\rho}\frac{\partial \tau_{Rij}}{\partial x_j} + g_i \tag{32}$$

$$\frac{\partial \overline{u}_i}{\partial x_i} = 0 \tag{33}$$

where

$$\overline{\tau}_{vij} = \rho\nu\left(\frac{\partial \overline{u}_i}{\partial x_j} + \frac{\partial \overline{u}_j}{\partial x_i}\right) \tag{34}$$

$$\tau_{Rij} = -\rho\overline{u_i' u_j'} \tag{35}$$

are the average viscous stress tensor and the Reynolds stress tensor that is due to the coherent and incoherent fluid motions.

The Reynolds equations are often further simplified to model free-surface flow in rivers by considering a two-dimensional mean velocity field attached to a solid boundary, meaning that there is no flow in the wall-normal or spanwise directions at the scale of the river. In addition, the river bottom is typically assumed to be averaged over small-scale roughness elements such as individual particles, ripples or dunes. The flow depth is measured normal to the average bed with the slope given by

$$S = -\frac{\partial \eta}{\partial x} \tag{36}$$

For the range of experiments considered in this dissertation and for most rivers, $S < 0.04$, so the small angle approximation is used to simplify the vector representation of the gravitational acceleration:

$$g_{i=1,3} = \begin{bmatrix} gs & -1 \end{bmatrix}. \tag{37}$$

In two-dimensions the average velocity vector is $\bar{u}_{i=1,3} = \begin{bmatrix} \bar{u} & \bar{w} \end{bmatrix}$ and the Reynolds equations under the slender flow approximation reduce to continuity, streamwise momentum and wall-normal momentum as:

$$\frac{\partial \bar{u}}{\partial x} + \frac{\partial \bar{w}}{\partial x} = 0 \tag{38}$$

$$\frac{\partial \bar{u}}{\partial t} + \bar{u}\frac{\partial \bar{u}}{\partial x} + \bar{w}\frac{\partial \bar{u}}{\partial z} = -g\frac{\partial H}{\partial x} + \frac{1}{\rho}\frac{\partial \tau}{\partial z} + gS \tag{39}$$

$$\bar{p}_h = \rho g(H - z) \tag{40}$$

where $\bar{p}_h$ is the deviation from local atmospheric pressure at the water surface, corresponding to the hydrostatic component of the average flow pressure. The only component of the original nine terms of the Reynolds stress tensor retained after the slender flow approximation is $\tau = \tau_{Rij} = \tau_{R13}$. The average pressure can be decomposed into hydrostatic and dynamic components

$$\bar{p} = \bar{p}_h + \bar{p}_d. \tag{41}$$

The depth averaged streamwise velocity denoted by $U(x,t)$ is defined as

$$UH = \int_0^H \bar{u} dz. \tag{42}$$

For the two-dimensional Reynolds equations the general structure of the streamwise flow velocity can be represented as a dimensionless structure function, f, where

$$\frac{\bar{u}}{U} = f(\varsigma, x)$$
$$\varsigma = z / H \tag{43}$$

If the dependence on x is ignored, the above equation reduces to a similarity solution. For slowly varying flows satisfying the slender flow approximation this is often the case.

From here the mathematical approach follows closely that of Castillo and George (2001) who sought similarity solutions for the mean velocity and the fluid stresses of the form

$$U - U_\infty = U_{SO}(x)\, f(\eta, \delta^+, \Lambda, \Theta) \tag{44}$$

and

$$u_1 u_3 = R_{SO}(x) r(\eta, \delta^+, \Lambda, \Theta) \tag{45}$$

where U_{SO} is the velocity scale of the outer layer, R_{SO} is the fluid stress scale of the outer layer, $\eta = \frac{y}{\delta}$ is the similarity variable and is a dimensionless depth, $\delta^+ = \delta u_* / \nu$ represents the local Reynolds number dependence based on the shear velocity defined by $u_* = \sqrt{\tau_w / \rho}$ in terms of the wall shear stress, Λ is a parameter that accounts for the local pressure gradient and Θ is a parameter representing a dependence on unknown conditions, for example the upstream controls.

The important results of Castillo and George (2001) show that a similarity solution of the form (44) and (45) is only possible if $U_{SO} \sim U_\infty$ and $R_{SO} \sim {U_{SO}}^2 \frac{\partial \delta}{\partial x} \sim {U_\infty}^2 \frac{\partial \delta}{\partial x}$ and $\frac{\partial \delta}{\partial x} \sim \frac{\delta}{U_\infty}\frac{\partial U_\infty}{\partial x} \sim \frac{1}{\rho}\frac{\delta}{U^2_\infty}\left[\frac{\partial P_\infty}{\partial x}\right]$ with the "surprising consequence" that $\delta \sim U_\infty^n$ where n is some non-zero constant. The pressure gradient parameter can then be defined as

$$\Lambda = \frac{\delta}{U_\infty \partial\delta/\partial x}\frac{\partial U_\infty}{\partial x} = \frac{\delta}{\rho U_\infty^2 \partial\delta/\partial x}\frac{\partial P_\infty}{\partial x} = \text{constant} \tag{46}$$

For nonzero values of the pressure gradient parameter (46) can be integrated to obtain

$$\delta \sim U_\infty^{-1/\Lambda}. \tag{47}$$

The exponent in the power law relation between the thickness and the external velocity is determined uniquely by

$$n = -1/\Lambda. \tag{48}$$

Figure 71 is experimental validation of (47) for rough beds if the "outer" velocity is replaced by the maximum velocity. The velocity deficit form of the CE Flume tests are plotted in Figure 72, where $\eta = y/\delta$ is the similarity variable. The velocity profiles are guaranteed to collapse at the top of the boundary layer and at the wall.

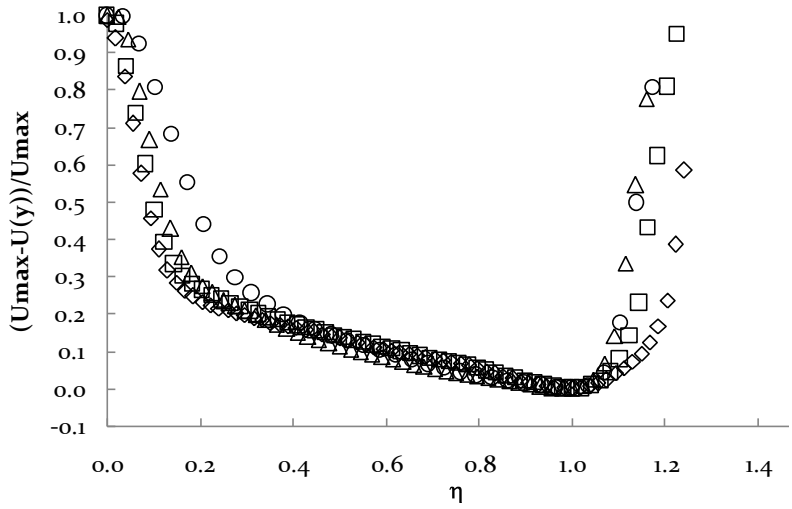

Figure 72. Mean velocity profiles

The extent of the near-wall region is shown to decrease in terms of the similarity variable with increasing flow strength, indicating that the effect of decreasing relative smoothness is to compress the dimensionless thickness of the turbulent core region. This effect is further illustrated in Figure 73, where these data are further collapsed near the wall by a renormalization using the relative smoothness parameter.

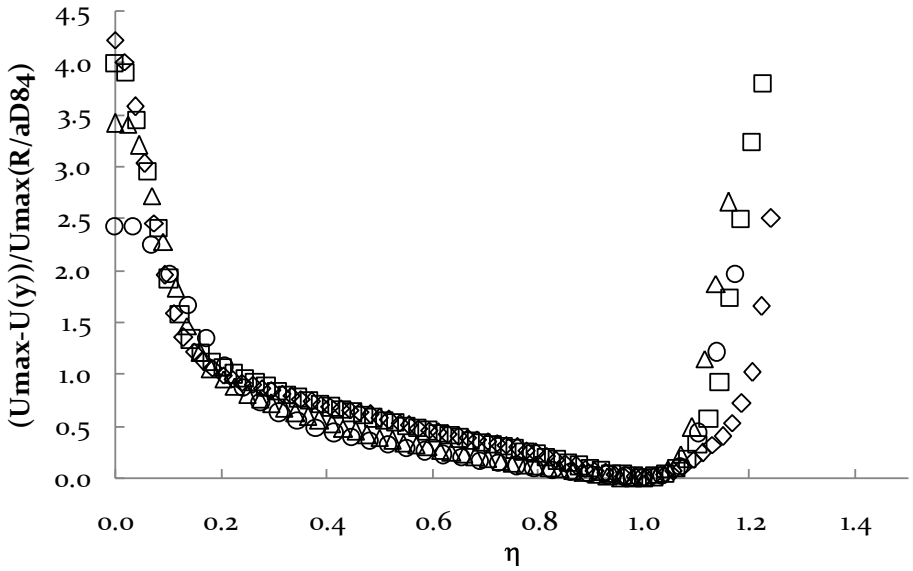

Figure 73. Velocity deficit normalized with R/aD84 using a = 2.5

Here the majority of the data collapse in the range $0.1 < \eta < 1.0$. The theory does not guarantee that all the tests will collapse onto a single curve. In comparison to Castillo and George (2001), the relative smoothness parameter has the same effect in these experiments as the dimensionless boundary layer momentum thickness parameter has near the wall in smooth-bed turbulent boundary layers with pressure gradients. A key difference between the similarity plots shown above and the analysis for smooth boundary layers by Castillo and George (2001) is the curvature of the velocity profiles near the free surface, which is absent in smooth 2-dimensional boundary layers. The free-surface

region $\eta>1$ still admits an additional velocity deficit in Figure 73 that is not fully explained by the similarity solution approach; however, in this case the "dip" region can be seen to be monotonically increasing functions of the similarity parameter in the free-surface region. In these experiments and presumably in larger rivers this region may be influenced by fluid motions in the top 1-cm or so near the free-surface where surface tension effects are important at the air-water interface. In these experiments this region is large compared to the flow depth and occupies the upper 20% of the flow.

The main point of this discussion about the structure of the mean flow is that the data show that these flows are by the Castillo and George (2001) definition equilibrium flows. This is consistent with the model of a vortex surface which contains knotted vortex tubes traveling as stable knot patterns in an equilibrium setup by the balance of vorticity flux and shearing stresses near the wall. Moreover, the simplest knots that fit our model are hyperbolic knots which have linking number $Lk = 4$. The prime knot that has four crossings is the figure-8 knot and the equilibrium solution shown above depends only on a pure number which happens to be very closely approximated by (minus) the knot invariant which is the volume of the knot complement. Castillo and George (2001) found this similarity parameter allowed for the collapse of nearly all positive pressure gradient boundary layer velocity profiles. This leads us to conclude the need for further research and additional data collection in rivers that may have local regions of zero or adverse pressure gradients in which the pressure gradient parameter is zero or 0.22, respectively. A hypothesis is that these are also knot invariants of prime knots, for example the knot shown at the bottom of Figure 65, which are created by repeated doubling of the sinusoidal argument in the z-component of the figure-8, representing an additional form of stable knots on the Klein bottle. Unfortunately at this time the hyperbolic volume of the knot compliment is only known for the figure-8 knot and more research is needed in this mathematical area as well.

7. SUMMARY AND CONCLUSIONS

The hypothesis is that a coherent structure organizes velocity fluctuations in rough, turbulent boundary layers. To examine this hypothesis experimental data of velocity measurements in gravel-bed flow conditions were collected in the laboratory. Because these flow data had a very high amount of turbulence intensity, sophisticated turbulence decomposition, or filtering, techniques were needed to produce snapshots, or pictures, for flow visualization to reveal coherent structures. It is possible to identify coherent vortex structures in the experimental data similar to previously observed structures in boundary layers, thus supporting the hypothesis. Next was derived a specific vortex model, alias Klein bottle, to describe the connectivity of observed vortex events during a turbulent burst and also the temporal and spatial patterns due to this organization of thin-cored vortex tubes which produces the same amount of spatial and temporal fluctuations observed in the data. The model further allowed a backdrop for the process by which the large eddies are connected to the small eddies and how both have origin at the bed or walls. The abstract fluid manifold traced out by the vortex motions was suggested to be in the form of a Klein bottle and thereafter the motions of the vortex filaments could be modeled as being induced by a given immersion of the Klein bottle into the fluid region and then orienting with the streamwise direction and the wall-normal direction. Eddies in time-series and spatial series of velocity data can be described by this structural model and that perhaps this is the physical reason why a velocity model could be found which is based on a similarity solution analysis.

Future research needs to examine further how the topology of knots relates to the distribution of mean velocity in gravel-bed rivers. Findings presented in this thesis suggest that the similarity approach better captures the topology of the natural fluid motions than a log-law which is traditionally used in boundary layer models.

Ultimately, the intent is to extend the vortex model to understand and describe flow conditions conducive to stable boundary conditions for gravel-bed rivers, i.e. to help us find stable river patterns and bed structures which promote healthy aquatic biology while at the same time minimizing sediment transport of particles existing on the boundary. The structural organization of the turbulent interactions is an important part of this future research. An important future step is to develop mathematical modeling of vortex surfaces under Euler flows to investigate the stability of figure-8 knots and other hypersurfaces which can be embedded on the Klein bottle, which is a continuation of the work of previous researches (Kida 1981; Ricca *et al.* 1999). It is also important to further investigate via numerical modeling the effects of vortex reconnection events under the full Navier-Stokes equations because the latter represents a transfer of turbulent kinetic energy which is an additional mechanism for energy transfer to the bed flow resistance. Thereafter, it is hopeful that a vortex model of structural organization can be used to understand and predict the fluid forces that cause portions of the river boundary to move and result in sediment transport phenomena and larger scale cyclic phenomena such as secondary currents and river meanders. Ultimately this model is intended to be used as a tool for understanding and predicting the distribution of velocity and turbulent fluid stresses for describing the fluid dynamical forces involved in future particle transport studies. Further, a model of the structure of turbulence presents a map for the turbulent vortices in the flow containing fixed points and closed curves and thus is a model of an attracting region and can be used in future turbulence modeling methods that focus on

the dynamical system context (e.g., Holmes et al. 1998). In the future, work will be towards the use of this vortex model for specific applications in restoration design of gravel-bed rivers.

REFERENCES

Adrian, R. J., Christensen, K. T., and Liu, Z. (2000). "Analysis and interpretation of instantaneous turbulent velocity fields." *Experiments in Fluids*, 29, 275-290.

Adrian, R. J., Meinhart, C. D., and Tomkins, C. D. (2000). "Vortex organization in the outer region of the turbulent boundary layer." *Journal of Fluid Mechanics*, 422, 1-54.

Allen, J. R. L. (1984). "Parallel lamination developed from upper-stage plane beds: a model based on the larger coherent structures of the turbulent boundary layer." *Sedimentary Geology*, 39, 227-242.

Balachandar, R., and Bhuiyan, F. (2007). "Higher-Order Moments of Velocity Fluctuations in an Open-Channel Flow with Large Bottom Roughness." *Journal of Hydraulic Engineering*, 133.

Boyland, P., Stremler, M., and Aref, H. (2003). "Topological fluid mechanics of point vortex motions." *Physica D: Nonlinear Phenomena*.

Cambridge. (2004). "Imaging math - Inside the Klein bottle." <http://plus.maths.org/issue26/features/mathart/applets/appletKleinParts.html>.

Castillo, and George. (2001). "Similarity Analysis for Turbulent Boundary Layer with Pressure Gradient: Outer Flow." *AIAA*, 39.

Chatterjee, A. (2000). "An introduction to the proper orthogonal decomposition." *Current Science*, 78(7), 808-817.

Clifford, N. J. (1993). "The analysis of turbulence time-series: statistical and correlation approaches using the Minitab package."" *Earth Surface Processes and Landforms*, 18, 845-854.

Dargahi, B. D. (1997). "Generation of coherent structures in turbulent boundary layers." *Journal of Engineering Mechanics*, 123(7), 686-695.

Defina, A. (1996). *Transverse Spacing of Low-speed Streaks in a Channel Flow over a Rough Bed.*, John Wiley & Sons Ltd, England.

Detert, M., Weitbrecht, V., and Jirka, G. (2007). "Simultaneous Velocity and Pressure Measurements using PIV and Multi Layer Pressure Sensor Arrays in Gravel Bed Flows." *HMEM, Lake Placid*.

Falco, R. E. (1977). "Coherent motions in the outer region of turbulent boundary layers." *Physics of Fluids*, 20(10), 5124-5132.

Fox, J. F., Papanicolaou, A. N., and Kjos, L. (2005). "Eddy taxonomy methodology around a submerged barb obstacle within a fixed rough bed." *Journal of Engineering Mechanics*, 131(10), 1082-1100.

Grass, A. J., Stuart, R. J., and Mansour-Tehrani, M. (1991). "Vortical structure and coherent motion in turbulent flow over smooth and rough boundaries." *Phil. Trans. R. Soc.*

Henderson, F. M. (1966). *Open Channel Flow*, Prentice-Hall, Inc., Englewood Cliffs, New Jersey.

Hicks, D. M., and Mason, P. D. (1998). *Roughness Characteristics of New Zealand Rivers*, Water Resources Publications, LLC.

Holmes, P., Lumley, J., and Berkooz, G. (1998). *Turbulence, Coherent Structures, Dynamical Systems and Symmetry*, Cambridge University Press.

Hommema, S. E., and Adrian, R. J. (2002). "Similarity of apparently random structures in the outer region of wall turbulence." *Experiments in Fluids*, 33, 5-12.

Hondzo, M. (1998). "Dissolved oxygen transfer at the sediment-water interface in a turbulent flow." *Water Resources Research*, 34(12), 3525-3533.

Hornig, G. (2001). "The geometry of reconnection." In: *An Introduction to the Geometry and Topology of Fluid Flows*, R. L. Ricca, ed., Kluwer Academic Publishers, Cambridge, UK, 239-252.

Hoyt, J. W., and Sellin, R. H. J. (2001). "Three-dimensional visualization of large structures in the turbulent boundary layer." *Experiments in Fluids*, 30(3), 295-301.

Imamoto, H., and Ishigaki, T. (1985). "Velocity vector measurements by laser doppler velocimeter in an open-channel flow." *Bulletin Disaster Prevention Research Institute*, 28, 471-486.

Kaftori, D., Hetsroni, G., and Banerjee, S. (1994). "Funnel-shaped vortical structure in wall turbulence." *Physics of Fluids*, 6(9), 3035-3050.

Khan, M. J., and Ahmed, A. (2005). "Topological model of flow regimes in the plane of symmetry of a surface-mounted obstacle." *Physics of Fluids*, 17.

Kida, S. (1981). "A vortex filament moving without change of form." *Journal of Fluid Mechanics*, 112, 397-409.

Kline, S. J., Reynolds, W. C., Schraub, F. A., and Runstadler, P. W. (1967). "The structure of turbulent boundary layers." *Journal of Fluid Mechanics*, 30(4), 741-773.

Klingeman, P. (Year). "Preface." *Gravel-Bed Rivers in the Environment*, Water Resources Publications, LLC., Gold Bar, Washington.

Kundu, P. K., and Cohen, I. M. (2004). *Fluid Mechanics*, 3 Ed., Elsevier, San Diego, CA.

Leopold, L. B., Wolman, M. G., and Miller, J. P. (1964). *Fluvial Processes in Geomorphology*, Dover Publications, Inc, New York.

Liberzon, A., Gurka, R., and Hetsroni, G. (2006). "POD of vorticity fields: A method for spatial characterization of coherent structures." *International Journal of Heat and Fluid Flow*, 27(3), 416-423.

Liu, Z. C., Adrian, R. J., and Hanratty, T. J. (1994). "Reynolds number similarity of orthogonal decomposition of the outer layer of turbulent wall flow." *Physics of Fluids*, 6(8), 2815.

Liu, Z. C., Adrian, R. J., and Hanratty, T. J. (2001). "Large-scale modes of turbulent channel flow: transport and structure." *Journal of Fluid Mechanics*, 448, 53-80.

Lumley, J. (1985). "Strange attractors, coherent structures and statistical approaches." In: *Theoretical Approaches to Turbulence*, D. L. Dwoyer, M. Y. Hussaini, and R. G. Voigt, eds., Springer-Verlag, New York.

Makita, H., and Sassa, K. (1993). "Three-dimensional vortical structure of a large-scale coherent vortex in a turbulent boundary layer." Springer-Verlag New York, Secaucus, NJ, USA, Munich, Ger, 23.

Manhart, M. (1998). "Energy Transfer Between Coherent Structures in the Wake of a Hemisphere."

Moffatt, H. K. (1969). "The degree of knottedness of tangled vortex lines." *Journal of Fluid Mechanics*, 35, 117-129.

Muller, A. (1982). "Secondary flow vortices: a structure in turbulent open channel flow." *Structure of Turbulence in Heat and Mass Transfer*.

Natrajan, V. K., and Christensen, K. T. (2006). "The role of coherent structures in subgrid-scale energy transfer within the log layer of wall turbulence." *Physics of Fluids*, 18(6), 065104.

Nezu, I. (2005). "Open-channel flow turbulence and its research prospect in the 21st century." *Journal of Hydraulic Engineering*, 229-246.

Nielsen, D. R., and Wendroth, O. (2003). *Spatial and Temporal Statistics*, Catena Verlag, Reiskirchen.

Nitsche, M. (2001). "Self-similar shedding of vortex rings." *Journal of Fluid Mechanics*, 435, 397-407.

Panton, R. L. (1996). *Incompressible Flow*, Second Ed., John Wiley & Sons, Inc., New York.

Poncet, P., Hildebrand, R., Cottet, G.-H., and Koumoutsakos, P. (2006). "Spatially distributed control for optimal drag reduction of the flow past a circular cylinder."

Porporato, A., and Ridolfi, L. (2002). "Some dynamical properties of a differential model for the bursting cycle in the near-wall turbulence." *Physics of Fluids*, 14(12), 4278-4283.

Rhodes, M. (1998). *Introduction to Particle Technology*, John Wiley & Sons, Ltd., West Sussex, England.

Ricca, R. L. (2001). "Geometric and topological aspects of vortex motion." In: *An Introduction to the Geometry and Topology of Fluid Flows*, R. L. Ricca, ed., Kluwer Academic Publishers, Cambridge, UK, 203-228.

Ricca, R. L., and Berger, M. A. (1996). "Topological ideas and fluid mechanics." *Physics Today*, 49(12), 28.

Ricca, R. L., Samuels, D. C., and Barenghi, C. F. (1999). "Evolution of vortex knots." *Journal of Fluid Mechanics*, 391, 29-44.

Robinson, S. K. (1991). "Coherent motions in the turbulent boundary layer." *Annual Review of Fluid Mechanics*, 23, 601-639.

Rodriguez, J. F., and Garcia, M. H. (2008). "Laboratory measurements of 3-D flow patterns and turbulence in straight open channel with rough bed." *Journal of Hydraulic Research*, 46(4), 454-465.

Rosgen, D. L. (1994). "A classification of natural rivers." *Catena*, 22, 169-199.

Roy, A. G., Buffin-Belanger, T., Lamarre, H., and Kirkbride, A. D. (2004). "Size, shape and dynamics of large-scale turbulent flow structures in a gravel-bed river." *Journal of Fluid Mechanics*, 500, 1-27.

Santhanakrishnan, A., and Jacob, J. D. (2007). "Flow control with plasma synthetic jet actuators." *Journal of Physics D: Applied Physics*, 40, 637-651.

Schlichting, H., and Gersten, K. (2000). *Boundary Layer Theory*, 8th Ed., Springer, Berlin.

Schwartz, J. S., and Herricks, E. E. (2008). "Fish use of ecohydraulic-based mesohabitat units in a low-gradient Illinois stream: implications for stream restoration." *Aquatic Conservation: Marine and Freshwater Ecosystems*.

Shnirelman, A. (2001). "Diffeomorphisms, Braids and Flows." In: *An Introduction to the Geometry and Topology of Fluid Flows*, R. L. Ricca, ed., Kluwer Academic Publishers.

Sholl, M., and Savas, O. (1997). "A fast lagrangian PIV method for study of general high-gradient flows." In: *35th Aerospace Sciences Meeting and Exhibit*, American Institute of Aeronautics and Astronautics, Reno, NV.

Shvidchenko, A. B., and Pender, G. (2001). "Macroturbulent structure of open-channel flow over gravel beds." *Water Resources Research*, 37(3), 709-719.

Sirovich, L. (1987). "Turbulence and the dynamics of coherent structures. I. Coherent structures." *Quarterly of Applied Mathematics*, 45(3), 561-570.

Smith, C. R. (1996). "Coherent flow structures in smooth-wall turbulent boundary layers: facts, mechanisms and speculation." In: *Coherent Flow Structures in Open Channels*, John Wiley & Sons, Ltd.

Stoesser, T., Rodi, W., and Froehlich, J. (2005). "LES of Open-Channel Flow over a Layer of Spheres." *Proceedings of 31th IAHR Congress, Seoul*.

Tamburrino, A., and Gulliver, J. S. (1999). "Large flow structures in a turbulent open channel flow." *Journal of Hydraulic Research/De Recherches Hydrauliques*, 37(3), 363-380.

Termini, D., and Greco, M. (2006). "Computation of flow velocity in rough channels." *Journal of Hydraulic Research*, 44(6), 777-784.

Thomas, A. S. W., and Bull, M. K. (1983). "On the role of wall-pressure fluctuations in deterministic motions in the turbulent boundary layer." *Journal of Fluid Mechanics*, 128, 283-322.

Tokaty, G. A. (1971). *A History and Philosophy of Fluid Mechanics*, Dover.

Tokieda, T. (2001). "Topology in Four Days." In: *An Introduction to the Geometry and Topology of Fluid Flows*, R. L. Ricca, ed., Kluwer Academic Publishers.

Wang, Z., and Larsen, P. (1994). "Turbulent structure of water and clay suspensions with bed load." *Journal of Hydraulic Engineering*, 1250(5), 557-600.

Wolfram Research, I. (2008). "Wolfram Mathworld." Mathworld.

Yalin, M. S. (1977). *Mechanics of Sediment Transport*, 2 Ed., Peragamon Press, Ontario.

Yalin, M. S. (1992). *River Mechanics*, Pergamon Press.

VITA

1. Born: January 24, 1972, in Glasgow, Kentucky.
2. Attended University of Kentucky and University of Louisville
   2.1. Awarded BSCE, University of Kentucky, 1994
   2.2. Awarded MSCE, University of Kentucky, 1997
3. Registered Professional Engineer
   3.1. Kentucky PE Number 21501
   3.2. Ohio PE Number 70545
4. Scholastic and Professional Honors
   4.1. Recipient of KY-TN Water Pollution Control Scholarship
   4.2. University Scholar
   4.3. BSCE Cum Laude
   4.4. Raymond Fellowship
5. Professional publications prior to Dissertation:

Fox, J. F., Patrick, A. and Belcher, B. "Large-scale eddies measured with large scale particle image velocimetry", *Flow Measurement and Instrumentation*. In Review.

Belcher, B. "Buffalo Run in the Cedar Grove Business Park, A Natural Channel Design Approach to Stormwater Management", *Land and Water Magazine*, April 2002. (this is a non-refereed journal)

Belcher, B. "Design-Build Natural Channel Diversions at Cedar Grove", River Management Society, Winter 2001/2002. (this is a non-refereed journal)

Belcher, B. and Fox, J. F. Poster: "Coherent Structures in Rough Open Channel Flows", AGU 2007, American Geophysical Union, San Francisco, California, Dec. 2007.

Fox, J. F., Belcher, B. and Patrick A. "Measurement of large-scale eddies using LSPIV, PIV, and ADV in a rough bed flume", FLUCOME 2007, ninth international symposium on fluid control, measurement and visualization, Tallahassee, Florida, Sept. 2007.

Belcher, B. and Fox, J. F. "Visualization of Turbulent Coherent Structures with PIV and ADV in Open Channel Flows over a Gravel Bed", HMEM 2007, Third Hydraulic Measurements and Experimental Methods Conference, Lake Placid, New York, Sept. 2007.

Mayhew, B., Fox, J. F., Belcher, B. Study of Soil Erosion Models at the Watershed Scale and Database Development, Kentucky Water Resources Research Institute Annual Symposium, Lexington, KY, March 2007.

Fox, J. F. and Belcher, B. Experimental study of the impact of upland sediment supply upon cohesive streambank erosion – Part 2: Fluid Turbulence. Kentucky Water Resources Research Institute Annual Symposium, Lexington, KY, March 2007.

Fox, J. F. and Belcher, B. Experimental study of the impact of upland sediment supply upon cohesive streambank erosion – Part 1 - Laboratory Design. Kentucky Water Resources Research Institute Annual Symposium, Lexington, KY, March 2006.

Fox, J. F., A.N. Papanicolaou, B. Belcher, N. Thompson, C. Davis, Land-Use Fingerprinting Techniques to Measure the Source of Fine Sediments in Central Kentucky, Kentucky Water Resources Research Institute Annual Symposium, Lexington, KY, March 2006.

Belcher, B. “Englewood Low-Head Dam Removal”, Watershed Management Association of Ohio Annual Conference, November 2005.

Belcher, B. “Runoff Curve Numbers”, County Engineers Association of Ohio Annual Conference, October 2005.

Belcher, B. “Beyond Riprap – a natural approach to stream restoration”, Effective Erosion Prevention in Construction in Ohio, Lorman Educational Services Seminar, March 2005.

Belcher, B. “Dimensionless Ratios and Natural Channel Design”, Federal Highway Administration Hydraulic Engineering Conference, Louisville, Kentucky, September 2002.

Belcher, B. “Natural Channel Design, Construction and Monitoring”, Water Environment Federation, Ft. Lauderdale Florida, February 2002.

Belcher, B. Stream Restoration Design Techniques, NAAMLP National Conference, Athens, Ohio, 2001.

Belcher, B. “Vane Structures Used in Natural Channel Design”, First Annual Ohio Natural Channel Design Conference, October 2001.

Belcher, B. Stream Restoration Design Techniques, TN Water Resources Annual Symposium, Nashville, Tennessee, April 2001.

Belcher, B. Stream Restoration Design Techniques Ohio Department of Natural Resources Stream Restoration Design Symposium, Salt Fork Resort, Ohio, October 2000.

Belcher, B. and Rush, R. Modeling Hydrological Response to Stage III NEXRAD Data in the Pond Creek Watershed Using HEC-HMS, KWRRI Kentucky Water Resources Research Institute Annual Symposium, Lexington, KY, 1999.

6. Printed Name: Brian J. Belcher